AUTOIGNITION MEASUREMENTS AND MODELING IN A RAPID COMPRESSION MACHINE

by

Daeyup Lee

B.S., Seoul National University (1986)
M.S., Korea Advanced Institute of Science and Technology (1988)
M.S., Massachusetts Institute of Technology (1993)

SUBMITTED TO THE DEPARTMENT OF
MECHANICAL ENGINEERING IN PARTIAL
FULFILLMENT OF THE REQUIREMENTS
FOR THE DEGREE OF

DOCTOR OF PHILOSOPHY
IN MECHANICAL ENGINEERING

at the

MASSACHUSETTS INSTITUTE OF TECHNOLOGY

February 1997

Signature of Author 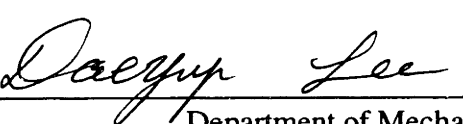
Department of Mechanical Engineering
January 22, 1997

Certified by 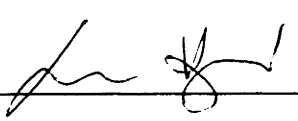
Simone Hochgreb
Associate Professor, Department of Mechanical Engineering
Thesis Supervisor

Accepted by 
Ain A. Sonin
Chairman, Departmental Graduate Committee

(This page has been intentionally left blank.)

Autoignition Measurements and Modeling in a Rapid Compression Machine

by Daeyup Lee

Submitted to the Department of Mechanical Engineering on January 22, 1997
in partial fulfillment of the requirements for the Degree of
Doctor of Philosophy in Mechanical Engineering

Abstract

The investigation of *high pressure autoignition* of combustible mixtures is important in providing both practical information for the design of combustion systems and fundamental measurements to verify and develop chemical kinetic models.

The main objective of this study was to develop a tool to study high pressure autoignition of reacting mixtures, using measurements of pressure records as a function of time and *autoignition* modeling in a *rapid compression machine* (RCM). Moreover, a simplified method for modeling the state of the reacting mixtures were sought. The work done in this study was: (a) Modification of the RCM piston head to suppress the *piston corner vortex*, (b) Understanding and modeling heat transfer from the gases and the effects of piston crevice, (c) Development of a model to reproduce measured pressure-time history incorporating heat loss and autoignition behavior, and (d) Verification of the model through autoignition measurements for hydrogen and oxygen mixtures. The measurements were made at p=0.6-4 MPa and T=950-1050 K, which are above the second explosion limit, and in a region previously unexplored. The results can be extended to study autoignition characteristics of fuel-oxidizer mixtures in the rapid compression machine for further studies.

The new design of the piston crevice in the present study has been shown to minimize disturbances to the reacting zone, allowing more accurate predictions of the reacting temperatures to be made from the measured pressure-time records. Using the initial conditions and gas molecular transport properties, a thermodynamic model combining chemical kinetic modeling, the behavior of core gas, and its heat transfer characteristics during the induction period was developed to reproduce the observed pressure history.

Hydrogen oxidation analysis showed that, at high pressures, reactions that are *chain-branching* ($H_2O_2+H=HO_2+H_2$) and very *exothermic* ($HO_2+HO_2=H_2O_2+O_2$) can play an important role in determining the induction time. The rate constant for $H_2O_2+H=HO_2+H_2$ was identified as one of the most important reactions for hydrogen oxidation at pressures above the second explosion limit; however, there has been no accurate evaluation of this reaction rate constants at high temperatures. A modification to this reaction rate $H_2O_2+H=HO_2+H_2$ ($k_{17}=2.3\times10^{13}$ exp(-7950/RT)) is suggested and validated using measured pressure profiles. The model with the modified reaction rate agrees very well with the measured pressure profile in terms of induction time and pressure rise due to energy release over the range tested in this study.

Thesis Supervisor : Simone Hochgreb
Title : Associate Professor of Mechanical Engineering

(This page has been intentionally left blank.)

ACKNOWLEDGMENTS

I would not have been able to complete this work without guidance, support and patience from Professor Simone Hochgreb. I also would like to thank Professor James C. Keck for direction and support when they were needed. Special thanks go to my thesis committee: Professor Wai K. Cheng and Professor Jack B. Howard. My thanks go to students and all staffs at the Sloan Automotive Laboratory.

This work has been supported by the Department of Energy/Office of Transportation Technology, through contract number DE-FG04-87AL44875, and a generous grant from Ford Motor Company. My gratitude for financial support goes to Professor Simone Hochgreb.

I have been fortunate enough to have the opportunities to work at the Sloan Automotive Laboratory, Massachusetts Institute of Technology for last five years. Those moments that gave me frustrations as well as achievements will nourish my life.

Finally, my deepest affection goes to my family, Hyunsun and Giwon, parents and parents-in-law for support and encouragement.

Daeyup Lee
January 1997

(This page has been intentionally left blank.)

TABLE OF CONTENTS

LIST OF FIGURES

LIST OF TABLES

NOMENCLATURE

a	speed of sound	m/sec
c_p	constant-pressure specific heat	J/mole
E_a	activation energy	kcal/mole
h	specific enthalpy	J/mole K
h_f^o	specific heat of formation at 298.15 K	J/mole K, kcal/mole K
h_x	heat transfer coefficient	W/m² °C
H	clearance height	cm
k	thermal conductivity	W/m °C
K_c	equilibrium constant based on concentration	
k_b	backward rate constant	cm³/mol/sec
k_f	forward rate constant	cm³/mol/sec
L	stroke	cm
m	mass	kg
M	molar mass	kg/mole
M_a	Mach number	
Nu_x	Nusselt number	
p	pressure	MPa
q	heat transfer rate	W
R^o	universal gas constant	8.3143 J/mole K
R	gas constant of the substance	J/mole K
Re_x	Reynolds number	
Q	heat	J
t	time	sec or ms
t_{cmp}	compression time	ms
T	temperature	K
T_f	film temperature, $=(T_\infty+T_i)/2$	K
U_p	piston speed	m/sec
V	volume	cm³
W	work	J

y	coordinate to describe boundary layer	
Y	mass fraction	
α	thermal diffusivity	m^2/sec
γ	specific heat ratio	
δ_t	thickness of thermal boundary layer	cm
δ_d	thickness of thermal displacement layer	cm
ρ	density	kg/m^3
τ_{ch}	characteristic heating time	ms
τ_s	characteristic time for sound speed	ms
τ_d	induction time	ms
τ_k	kinetic induction time	ms
$\dot{w}$	molar rate of production	mole/sec

Subscript

ad	adiabatic
bl	boundary later
cr	piston head crevice
i	initial state
iso	isothermal
K	number of species
peak	peak point when compression process completes
∞	core gas
w	condition at the cylinder wall

GLOSSARY

autoignition (self-ignition, spontaneous ignition) : rapid increase of the temperature of the mixture (not initiated by any external ignition source) when the energy released by the reaction as heat is larger than the heat lost to the surroundings.

core (in a combustion chamber) : the region where temperature gradients are almost uniform, *i.e.*, what is not confined to the growing thermal boundary layer.

corner vortex (piston corner vortex, rolled-up boundary layer) : unusual flow pattern in the corner formed by the cylinder wall and the piston face. Because a boundary layer exists on the cylinder wall, a vortex flow is generated when the piston moves.

induction time (ignition delay time, ignition delays, autoignition time): the interval between the moment of the steepest slope during compression process to the moment of the maximum pressure gradient ($\geq 10^5$ MPa/s, that is, 10 MPa (maximum operating pressure) pressure rise during 0.1 ms) after the compression process.

peak pressure, peak temperature : pressure and temperature when the compression process is completed. Thereafter, the cylinder volume is kept constant.

piston crevice : total volume of piston head crevice and piston O-ring crevice.

piston head crevice : consisting of the volume between the piston and the cylinder wall, above the O-ring packs which seal the combustion chamber.

piston O-ring crevice : Unoccupied O-ring groove volume by O-ring and back-up rings at cylinder side.

thermal boundary layer : the region where temperature gradient (resulting from a heat exchange process between the gas and the wall) are present in a cylinder.

CHAPTER 1. INTRODUCTION

Chemical kinetic modeling has become an important tool in the analysis of combustion systems. Since large amounts of elementary kinetic data, accurately estimated specific reaction rates, and increased computation capability have become available, detailed kinetic modeling has become more useful to understand and improve not only conventional combustion systems such as internal combustion engines, but other combustion fields such as the safe storage and transportation of liquid and gaseous fuels.

The investigation of high pressure *autoignition*[*] of combustible mixtures is important in providing both practical information for the design of combustion systems and fundamental measurements to verify and develop chemical kinetic models. A great deal of progress has been made in recent years toward both understanding and predicting pressure dependent behavior of important combustion reactions. However, further improvements in dealing with pressure dependence for modeling purposes are still needed, since many unimolecular decomposition reactions and their associated recombination reactions exhibit significant pressure dependence in some experimental regimes.

The focus of this study was to develop a tool to study *high pressure* autoignition of reacting mixtures, using measurements of time-pressure records and modeling autoignition in a rapid compression machine (RCM). A RCM was implemented in order to create well characterized reacting conditions, and the model was developed to reproduce autoignition in the

---

[*] Rapid combustion reaction which is not initiated by any external ignition sources. Please refer also to glossary section for the definition of terminologies.

RCM within acceptable accuracy while maintaining simplicity. Model verification using the autoignition measurements is the main goal of this study.

1.1 Background

High temperature combustion studies are complicated by the fact that typical time scales are extremely short and reaction rates are very sensitive to temperature. Several *experimental methods* available to study chemical kinetics are summarized in Table 1.1.1. Among them, measurements in a RCM have *advantages* such as: well controlled conditions (in terms of peak pressure and temperature), direct measurement of induction time, no disturbance by residual gases, and high pressure measurement. *Disadvantages* are: no sampling (confined to the current study) and no direct temperature measurements for core gas as well.

Basic *operation principle* of a RCM is that it compresses the reacting mixtures, so they reach the required high pressure and temperature in a short time (in order to avoid significant heat loss during compression process). Thereafter, the *constant volume* autoignition of gaseous fuel-oxidizer mixtures occurs when the energy release by the chemical reaction as heat becomes larger than the heat loss through the cylinder wall. As a result, the temperature of the mixture

Table 1.1.1 Summary of experimental methods with typical parameter ranges.

	Pressure	Temperature	Advantages	Disadvantages
Motored/skip-fired engine	< ~ 5 MPa	< ~ 1200 K	realistic (P,T), sampling	residual gases, vigorous fluid motion
Flow reactor	~ 0.1 MPa	850-1300 K	speciated	no induction time, moderate pressures
Static reactor	~ 0.1 MPa	< ~ 800 K	speciated, simple	surface effects
Shock tube	< ~0.3 MPa	> ~1300 K	near adiabatic, speciated sampling	unclear induction time
Rapid compression machine	< ~ 6 MPa	700-1200 K	high pressures, induction time	no sampling (currently)

increases, thus rapidly accelerating rates of involved reactions and results in self-accelerating event in which pressure and temperature increase rapidly at constant volume. Therefore, with known pressure and temperature conditions, direct measurement of induction time (definition discussed in section 2.4) and autoignition behavior (associated with time-pressure profile) are available. Table 1.1.2 summarizes the specifications of RCMs used in previous chemical kinetic studies*.

For the investigation of autoignition and reaction characteristics of fuels at high pressures, the RCM is the most suitable device (compared with methods in Table 1.1.1) and can be extended to the highest pressures and concentrations than any other experimental methods. However, previous studies using RCMs were hampered by temperature non-uniformities and fluid motion in the chamber resulting from the scraping of the thermal boundary layer by the piston, in turn leading to difficulties in separating the chemical kinetics from the transport effects.

Table 1.1.2 Specifications of the rapid compression machines used in previous chemical kinetic studies.

Affiliation	Driving mechanism	Bore/stoke Clearance height Compression time	Remarks	References
University of Leeds, UK	compressed air at 820 kPa	46/233 mm 22.7 mm 22 ms	-	Schreiber *et al.* 1993.
Nagoya Inst. of Tech., Japan	-	65/140 mm - up to ~6.5 ms	O-ring sealing, variable CR	Furutani *et al.* 1993.
Massachusetts Inst. of Tech., USA	compressed air at 2 MPa	50.8/<~110 mm 6.2-15(?) mm 10-30 ms	O-ring sealing, variable CR, *piston head crevice*	Park 1990.
Universite des Sciences et Techniques de Lille, France	mechanical cam	50mm 20 mm -	two pistons, electrically heated chamber	Carlier *et al.* 1990

* Since 1990. As far as we are aware.

Reaction processes in RCMs have been usually assumed to be uniform - this simplifies the analysis, and was considered to be close to realistic until recently. However, visual observations have revealed that mixture condition is far from uniform (Furutani *et al.* 1993 & Tabaczynski *et al.* 1970). The reaction in conventional RCMs is highly non-uniform, leading to problems of poor repeatability and difficult characterization of mixture conditions.

Tabaczynski *et al.* (1970) observed a vortex motion at the piston face and cylinder wall interface as the cylinder wall moves towards the piston. Furutani *et al.* (1993) observed spatially non-uniform ignition behavior in a RCM: a sliced-pineapple like structure, composed of a center core and an outer ring in the vicinity of the cylinder wall. They observed a quite local onset in methane ignition as if it propagates into the combustible volume. They noted that very local onset with gradual luminosity and pressure rises as well as ignition with steep rises could be obtained even with the same mixtures prepared in a single lot. However, Elsworth *et al.* (1963) stated that the ignition becomes heterogeneous when particles larger than 10 nm in diameter exist in the mixture. If one interprets this conversely, they effectively asserted that the absence of particles would give completely homogeneous ignition. However, the quantitative implications for the assumption that particles are the main reason for non-homogeneous ignition have not been addressed yet.

Griffiths *et al.* (1986) positioned grids adjacent to the final resting position of the piston face at the end of its stoke, in order to achieve conditions of enhanced heat loss from the hot, compressed gas mixture in the combustion chamber. The result showed a marked enhancement in the initial cooling rate (in accordance with the change in average gas velocities) and the decay of mean gas-temperature (derived from pressure records) following compression of a non-reactive mixture under the effects of grids. Griffiths *et al.* (1993) also showed by numerical study that the predominant motion within the central core remains in the direction of the piston motion, with a 'rolled-up vortex' causing recirculation at the periphery of the cylinder.

When the reacting mixture is disturbed by piston vortex, the estimation of core gas* temperature and concentration (if the core exists yet) from measured pressure records becomes difficult. Most numerical studies of autoignition, either as comprehensive kinetic schemes encompassing hundreds of elementary reactions or as reduced models, have been based on the assumption of spatial uniformity within the combustion chamber, either with heat loss (Halstead 1977) or without (Carlier *et al.* 1990, Ohta *et al.* 1988). At another extreme, CFD models have been developed to predict the detailed behavior of the mixture in a combustion chamber (Griffith *et al.* 1993).

In autoignition modeling, a spatial uniformity of temperature and species concentration have been generally assumed to exist only when vigorous gas motion is induced (Griffiths *et al.* 1990) or when stirred flow reactors are used (Baulch *et al.* 1988, Westbrook *et al.* 1988). The assumed idealization (spatially uniform temperature and concentrations within the reacting core) was first realized by the RCM equipped with a specially designed piston head to suppress the generation of piston vortex (Park 1990, Park & Keck 1990). They developed a RCM to obtain uniform well-defined core gas, heat transfer reduction, and containment of the vortex formed from the side wall boundary layer. A crevice volume on the piston head was incorporated to achieve the side wall vortex containment. The result showed enhanced repeatability of both induction time measurements and qualitative estimation of core temperature from the pressure measurements.

Based on this approach, autoignition modeling became feasible, with assumptions that reacting core is well defined and conserved (not significantly disturbed by vigorous fluid motion).

---

* Portion, external to thermal boundary layer, assumed to have uniform temperature, thus negligible temperature gradient inside.

1.2 Objectives

If autoignition in a RCM is to be modeled successfully, one must first implement fluid dynamics in conjunction with chemical kinetics and heat loss models in sufficient detail to reproduce the measured pressure history of fuel oxygen mixtures at high pressure and temperature in the cylinder. It seems that little has been achieved to measure and model autoignition in circumstances, especially in a RCM, in which the autoignition develops from mainly chemical kinetic interactions while minimizing fluid motion interaction in order to make the model simpler but to benefit from the detailed chemical kinetic mechanisms available.

Therefore, the objectives of this study were:

(a) Modification of a piston head to suppress the piston corner vortex,

(b) Understanding of the heat transfer that characterizes the reacting core and the effects of piston crevice volume on heat loss,

(c) Development of a model to reproduce measured pressure-time history incorporating heat loss and autoignition behavior, and

(d) Verification of a model by measuring hydrogen autoignition.

The results can be extended to study autoignition characteristics of fuel-oxidizer mixtures in the rapid compression machine for further studies.

1.3 Thesis organization

This thesis will detail the development of a model to study autoignition in a rapid compression machine and its validation through well characterized and implemented measurements, which provide time-pressure records. Chapter 1 gives an introduction and brief background of

autoignition measurements and chemical kinetic studies in RCMs. Chapter 2 outlines what equipment was used, how the measurements were conducted, and how things were defined in order to extract the parameters of interest such as peak pressure, peak core temperature, and induction time. It discusses how the piston head crevice was designed to minimize piston corner vortex and describes the configurations of piston heads tested in this study. It also contains the discussion of the piston O-ring pack motion and its volume variation. Finally, in that chapter the piston displacement is discussed. Chapter 3 details the model developed to simulate time-pressure records, and the assumptions introduced to derive the model. It also calculated results and a parametric study of the model. Validation of the model with measured time-pressure records are illustrated in chapter 4. The performance of several piston heads tested in this study are also compared and discussed. Following that discussion, there are examples of the simulation results whose objectives was to understand the heat transfer characteristics of the rapid compression machine during and after the compression process. Pressure drop after the compression process and the associated core temperature calculated from the model are discussed. Chapter 5 deals with hydrogen autoignition: induction time measurements at high pressures and moderate temperatures, the analysis of hydrogen oxidation mechanism, and the simulated results of time-pressure profiles, which are validated by the measured time-pressure records. The results suggest the modification of the reaction rate constant to explain the high pressure hydrogen oxidation characteristics. The final chapter gives conclusions by this study. Appendix 1 contains the analysis of the piston O-ring crevice volume: leakage check and the motion of piston O-ring packs. Appendix 2 describes the test failures and diagnoses, which can be used to improve the rapid compression machine for the future study. It also includes the discussion of abnormal ignition associated with pure oxygen tests, the reason for which has not been clarified, however, should be understood to improve measurement repeatability. Appendix 3 details the derivation of model equations described in Chapter 3 and discusses the verification

of assumptions. It also contains the derivation of compression time from measured data. Appendix 4 lists thermodynamic properties data and reaction rate constants used with CHEMKIN routines, the structure of programs to model autoignition, program lists, and measured data of hydrogen autoignition. Finally, Appendix 5 describes the additional suggestion of reaction rate for R17 for further study.

CHAPTER 2. RAPID COMPRESSION MACHINE

2.1 Introduction

Rapid compression machines (RCM) have been widely used to study the autoignition characteristics of fuel and oxygen mixtures at high pressures and temperatures, typically 1 to 5 MPa and 700 to 1100 K. One reason is that engine knock in ordinary cars occurs in a range of end-gas temperature of 800 to 1000 K and pressure of 3 to 5 MPa. Experimental data on ignition delays over a continuous range of 600-1800 K are necessary for a better understanding of engine knock and for the development of a unified mechanism to be available at wide temperature and high pressure ranges.

Most numerical studies of autoignition, either using comprehensive kinetic schemes encompassing many thousands of elementary reactions or using reduced models, have been based on an assumed spatial uniformity within the combustion chamber. Also, they assumed that the core region is compressed virtually adiabatically and comprises most of the combustion chamber volume (Griffiths *et al.* 1992, Carlier *et al.* 1990 & Halstead *et al.* 1977). However, spatial uniformity is approached only in experiments where vigorous gas motion is induced, as in the work of Griffiths (1990), or when stirred flow reactors are used, as in the work of Baulch *et al.*(1988), Gueret *et al.* (1990) and Westbrook *et al.* (1988).

Autoignition in RCMs, however, has often been observed to be non-uniform. Furutani (1993) observed that the onset of piston-compression ignition is spatially heterogeneous and very

local as if it propagates into the combustible volume. A vortex motion is observed at the piston face and cylinder wall interface as the cylinder wall moves towards the piston (Tabaczynski *et al.* 1970) and the numerical study by Schreiber *et al.* (1993) shows that the predominant motion within the central core remains in the direction of the piston motion, while a *roll-up vortex* causes recirculation at the periphery of the cylinder. Griffiths *et al.* (1993) stated that the quantitative implications for kinetic modeling as a consequence of the assumed idealization have been rarely addressed.

In this study, following the approach by Park (1990) the RCM is equipped with a special piston head crevice that can swallow the thermal boundary layer generated during the compression process, to avoid the creation of a corner vortex between the piston head and the wall. This way, temperature non-uniformity effects in the core gas, where autoignition will take place, can be minimized. The design of a piston head, implemented to realize uniform core properties and well-defined core behavior , will be presented in this chapter.

The followings are discussed in this chapter: the experimental system, operating parameters, pressure and induction time measurements, piston head crevice used to prevent the piston corner vortex from generating and piston motion during compression process.

2.2 Rapid compression machine

2.2.1 Experimental system

The rapid compression machine (RCM) built by Park (1990) was modified and used for studies of autoignition (Lee 1993) (Fig.2.2.1). RCM geometry and operating conditions are listed in Table 2.2.1. The piston is driven downwards by compressed air. The area ratio between the driving piston side and the combustion chamber piston side is 4 to 1. The stroke and the clearance height can be adjusted to fit a desired compression ratio of up to 19. The hydraulic

Table 2.2.1 Characteristics of the rapid compression machine.

Cylinder bore	5.08 cm
Maximum stroke	~11 cm
Maximum compression ratio	~19
Clearance height	0.6~2.0 cm
Max. peak pressure	~7 MPa
Compression time	10~30 ms
Max. peak temperature	~1300 K

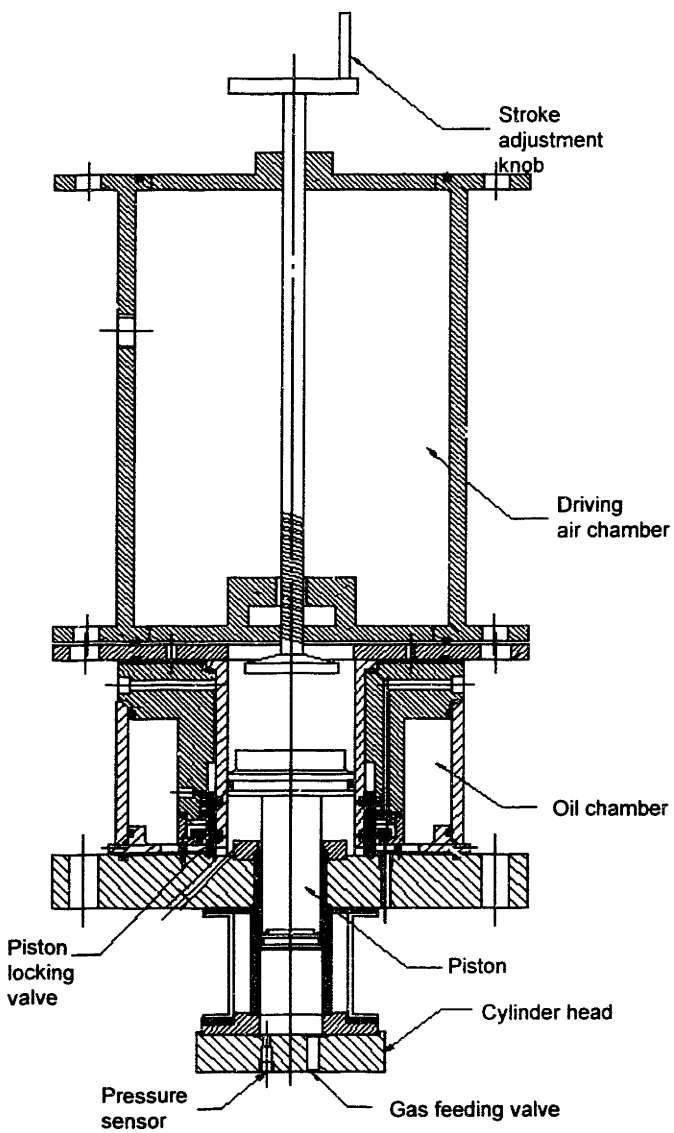

Figure. 2.2.1 Cross sectional view of the Rapid Compression Machine.

oil through variable-area-orifice can adjust acceleration and deceleration characteristics of the piston motion. Gas mixture can be compressed within 10~30 milliseconds to pressures up to 7 MPa. The piston travels at a constant velocity (~5 m/sec) throughout most of its stroke. The reaction chamber is axisymmetric, cylindrical shape, and combustion takes place in a closed constant volume when the piston came to rest. Fuel and gases used had research grade purity or maximum available. The mixture condition was determined by measuring partial pressures with a MKS 122A (range 0-1000 mmHg) diaphragm pressure gauge with an accuracy of 0.1 mmHg (13.33 Pa). Gaseous reactants (consisting of fuel and gases in predetermined proportions) were loaded into the cylinder prior to firing the machine. Compression of the fuel-gas mixture was possible to pressures up to 7 MPa. Core temperatures during the compression process and up to the peak* pressure point (non-reactive) are calculated from the measured pressure using the isentropic relation (Refer to Fig. 2.2.2 for definitions) :

$$\ln(\frac{T}{T_i}) = \int_{p_i}^{p} \frac{\gamma(T)-1}{\gamma(T)} d\ln p \qquad (2.2.1)$$

Compressed peak temperatures in the range 800-1100 K were available by this method.

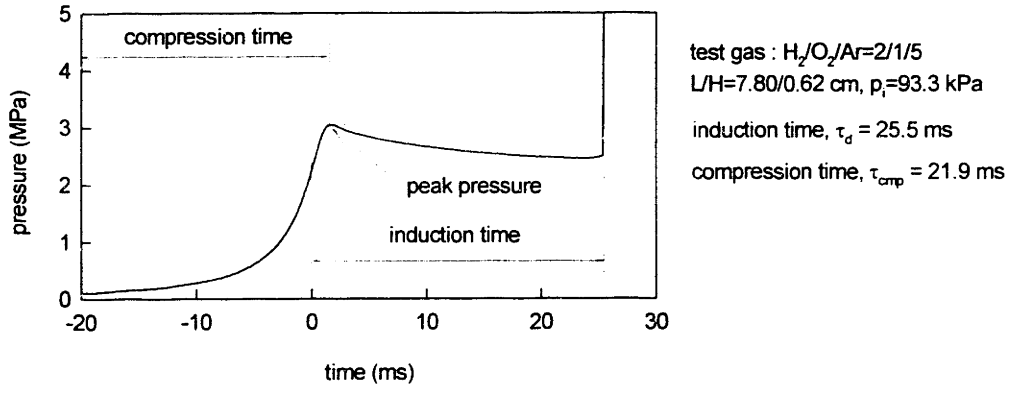

Figure 2.2.2 Definitions of compression time, induction time, and peak pressure.

* pressure when the compression process is completed. Thereafter, the cylinder volume is kept constant.

Repeatability was verified by performing about ten measurements at several operating parameters covering experimental ranges. Pressure-time records were measured by a piezoelectric transducer (Kistler 6123 : range 200 bar, linearity ± 0.2 %) located on the bottom side of the combustion chamber. The voltage signal from a charge amplifier was stored in a PC through a data acquisition board (DT 2821) and recorded digitally at frequency of 100 kHz. Fig. 2.2.3 shows an overall diagram for the experimental system.

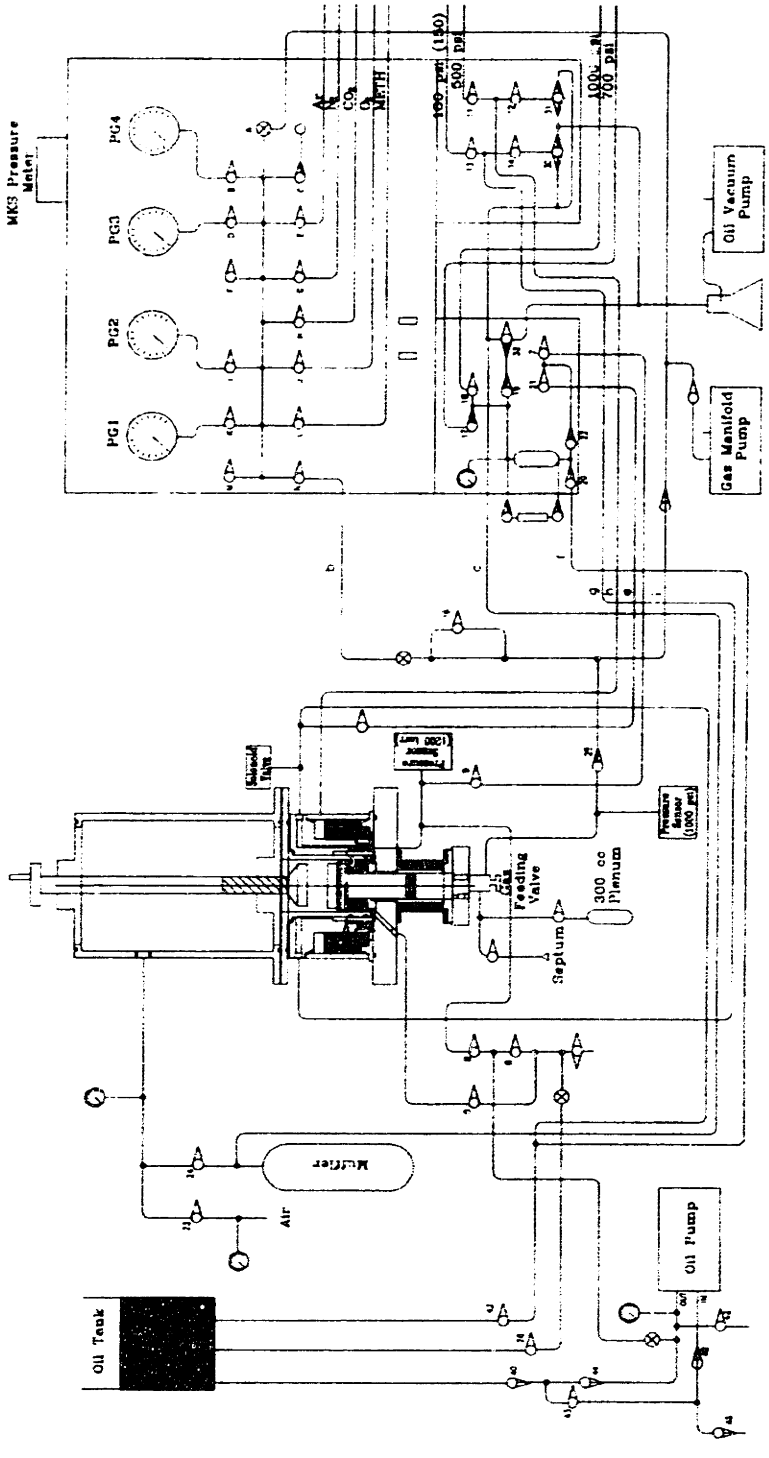

Figure 2.2.3 An overall diagram of the experimental system.

2.2.2 Operating parameters

Figure 2.2.4 (a) shows three typical pressure measurements in the rapid compression machine for combustion chamber, hydraulic oil pressures near the speed control orifice and piston locking valve. Locations are presented in Fig.2.2.4 (b). Among several operating parameters for the RCM, the following parameters were kept constant to maintain consistent measurements:

(a) driving air pressure (~1.2 MPa): The driving air pressure is an important operating parameter to control the compression time, which affects the peak pressure and therefore peak temperature as shown in Fig.2.2.5. Thus, the driving air pressure was kept fixed.

(b) oil pressure sustaining piston underneath driving piston (~2 MPa).

(c) oil pressure to lock the piston locking valve (~2.8 MPa).

(d) speed control orifice opening angle (30 degree).

Some operating parameters were varied to obtain the required pressure and temperature at the peak when the compression process completed. This was performed by three methods: (i) changing the initial pressure of reactant gases to maintain a constant peak temperature (Fig.2.2.6

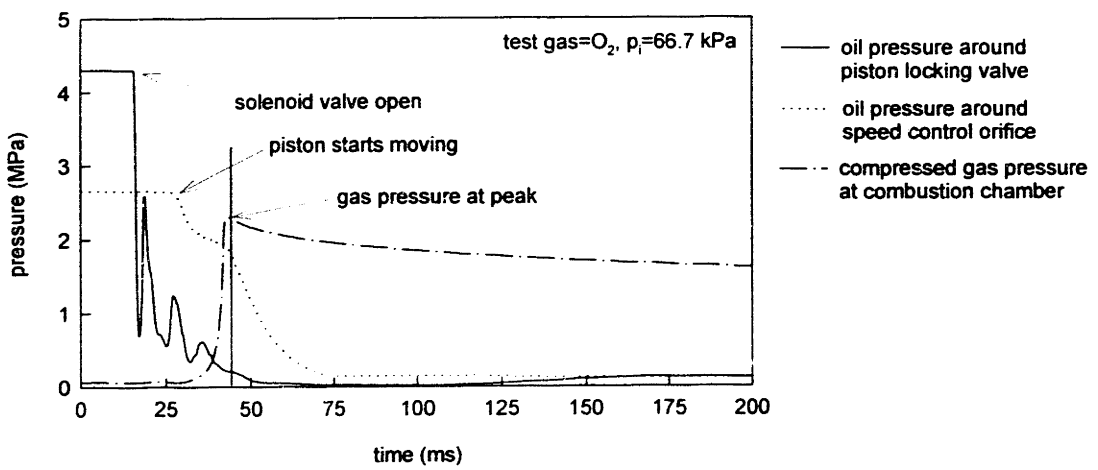

Figure 2.2.4 (a) Pressure records of hydraulic oil and combustion chamber.

(continued)

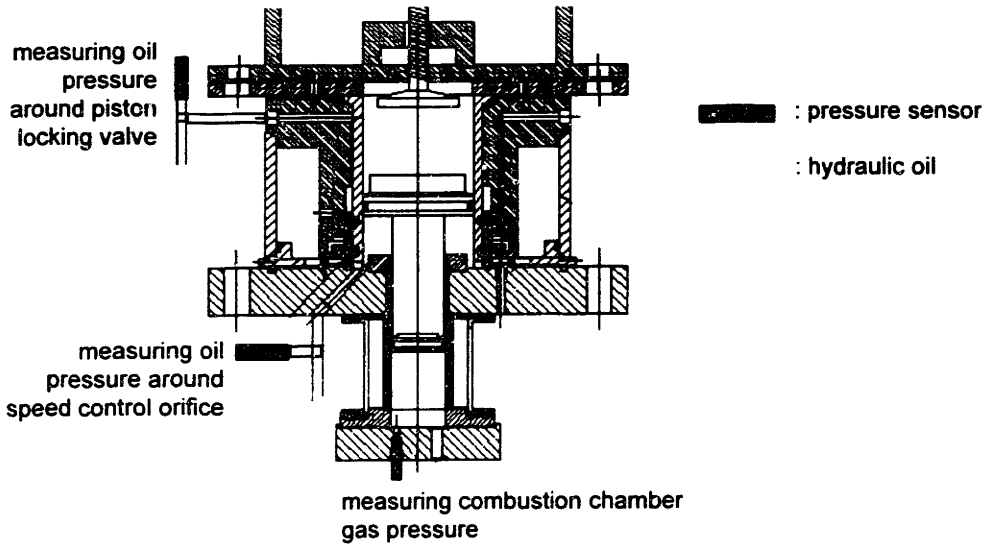

Figure 2.2.4 *(continued)* (b) Locations at which pressures were measured.

(a)), (ii) changing strokes while maintaining approximately constant peak pressure (Fig.2.2.6 (b)) and (iii) Ratio between non reactive components (N_2, Ar) was varied (Fig. 2.2.6 (c)): When a compression ratio, that is, the stroke and clearance height are kept constant, it is necessary to alter the heat capacity of the reactant mixture in order to change the temperature reached at the end of compression while maintaining approximately constant peak pressure.

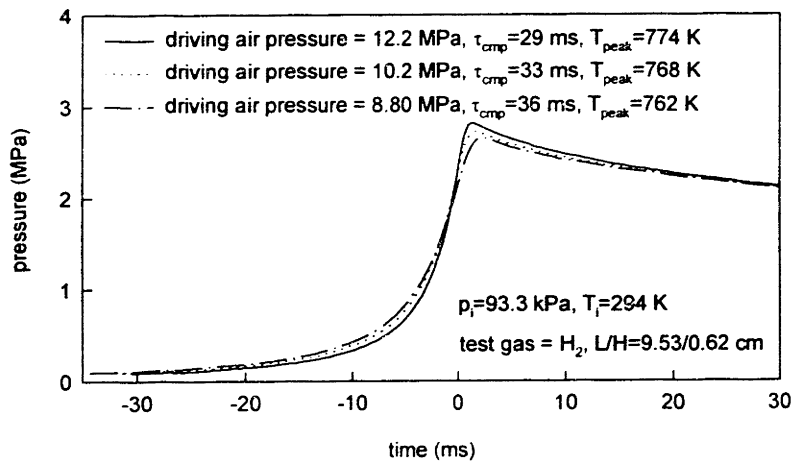

Figure 2.2.5 Measured pressure-time records depending on an operating parameter of the driving air pressure. The peak temperature can be affected, since the compression time is changed depending on the driving air pressure.

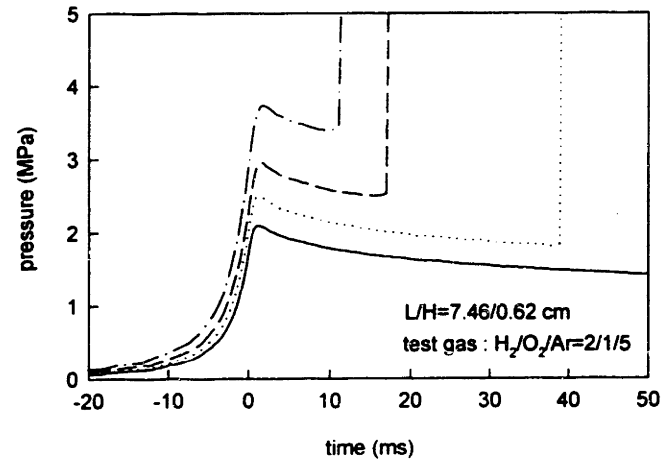

p_i=120.0 kPa
p_{peak}=3.73 MPa, T_{peak}=986 K
p_i=93.3 kPa
p_{peak}=2.95 MPa, T_{peak}=993 K
p_i=80.0 kPa
p_{peak}=2.50 MPa, T_{peak}=989 K
p_i=66.7 kPa
p_{peak}=2.10 MPa, T_{peak}=990 K

(a) Variable initial pressures. ΔT_{peak}=±3.5 K

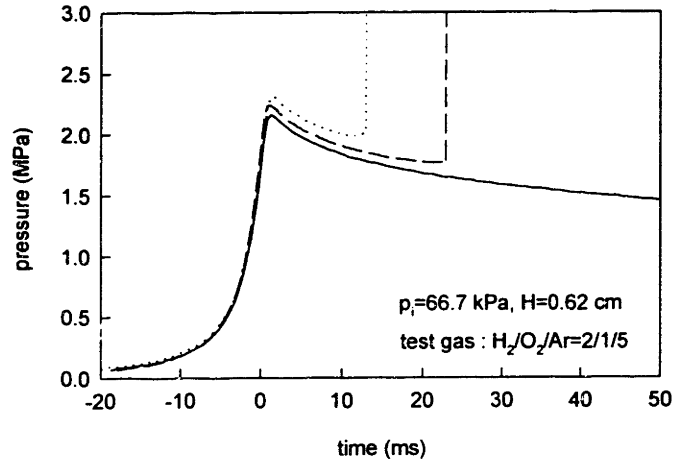

L=8.28 cm
p_{peak}=2.28 MPa, T_{peak}=1000 K
L=8.00 cm
p_{peak}=2.24 MPa, T_{peak}=993 K
L=7.80 cm
p_{peak}=2.16 MPa, T_{peak}=982K

(b) Variable stroke. Δp_{peak}=±0.06 Mpa

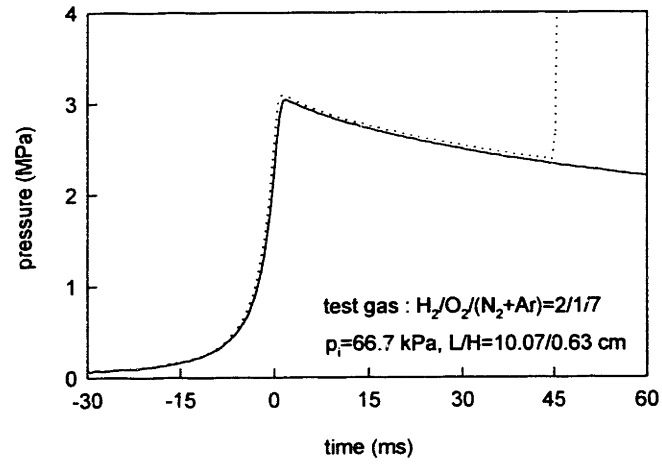

N_2/Ar=3.85/3.15, γ_{peak}=1.412
p_{peak}=3.09 MPa, T_{peak}=944 K
N_2/Ar=4.2/2.8, γ_{peak}=1.405
p_{peak}=3.04 MPa, T_{peak}=928 K

(c) Variable specific heat ratios. Δp_{peak}=±0.03 Mpa

Figure 2.2.6 Variation of operating parameters to achieve the required peak pressure and temperature of gas mixtures.

2.3. Pressure measurement

2.3.1 Reactants pressure

Figure 2.3.1 shows a typical partial pressure measurement of reactants mixture by MKS 122A diaphragm pressure gauge. Each fuel/gas component was loaded into a combustion chamber at the predetermined ratio and uniform mixing was obtained by waiting enough time. In the case of gaseous fuel such as hydrogen, fuel + oxygen + inert gas mixture (at the required ratio) was prepared in a cylinder bomb in advance and loaded into a combustion chamber in order to prevent the mixture composition from varying from run to run.

2.3.2 Pressure-time records

Typical measured pressure profiles (using a Kistler 6123 pressure transducer) have been presented in previous sections (Refer to Fig.2.2.6). The *core* temperature of reactants mixture *during* the compression process, and the *peak* temperature when the piston motion ceases, can be derived from the measured pressure-time records (with the assumption of isentropic process and no chemical reaction assumed by Eq.2.2.1). The *repeatability* of the pressure measurement within an acceptable range is important to ensure that the associated temperature behavior is

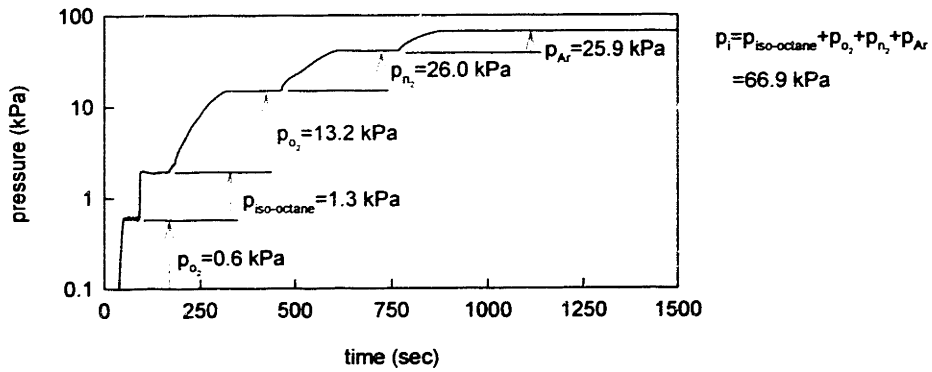

Figure 2.3.1 Pressure-time records of fuel(iso-octane) and gas mixture.

reproducible. Although careful experimental procedures are followed, the minimum pressure deviation is limited by the resolution of measuring devices. The minimum ideal deviation can be estimated from the following sensitivity analysis. Since

$$\frac{p_{peak}}{p_i} \sim CR^{\bar{\gamma}-1} \quad \text{and} \quad \frac{T_{peak}}{T_i} \sim \left(\frac{p_{peak}}{p_i}\right)^{\frac{\bar{\gamma}-1}{\bar{\gamma}}},$$

$$\frac{\Delta p_{peak}}{p_{peak}} = \sqrt{\left(\frac{\partial p_{peak}}{\partial p_i}\right)^2\left(\frac{\Delta p_i}{p_{peak}}\right)^2 + \left(\frac{\partial p_{peak}}{\partial \bar{\gamma}}\right)^2\left(\frac{\Delta \bar{\gamma}}{p_{peak}}\right)^2} \tag{2.3.1}$$

$$\frac{\Delta T_{peak}}{T_{peak}} = \sqrt{\left(\frac{\partial T_{peak}}{\partial p}\right)^2\left(\frac{\Delta p}{T_{peak}}\right)^2 + \left(\frac{\partial T_{peak}}{\partial p_i}\right)^2\left(\frac{\Delta p_i}{T_{peak}}\right)^2 + \left(\frac{\partial T_{peak}}{\partial \bar{\gamma}}\right)^2\left(\frac{\Delta \bar{\gamma}}{T_{peak}}\right)^2} \tag{2.3.2}$$

where $\bar{\gamma} = \frac{\gamma(T_i)+\gamma(T_{peak})}{2}$ was assumed.

At typical experimental conditions, a comparison was made between the estimated minimum deviation limited by the resolution of the measuring devices and the measured deviations as shown in Fig.2.3.2. The results indicate that the measured pressure-time records were well

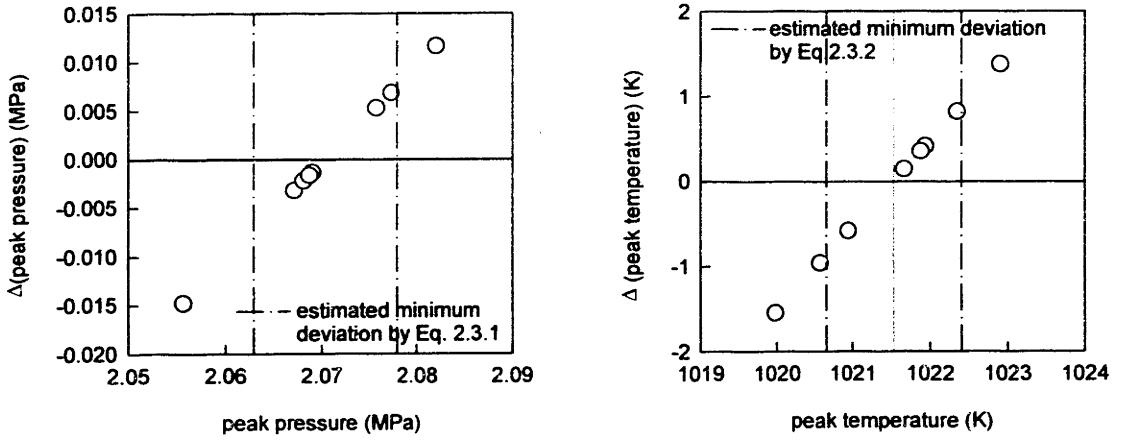

Figure 2.3.2 Comparison of deviations of measured peak pressure and calculated peak temperature from measured pressure records. Deviations are close to the estimated minimum ideal errors (limited by the sensor resolutions described in section 2.2.1). Eight measurements were made at the identical experimental conditions: Test gas was $H_2/O_2/N_2/Ar$ = 2/1/0.175/6.825, L/H = 6.98/0.62 cm. T_i=292.8±0.2 K. p_i=66.7 kPa.

repeatable within acceptable range, hence the peak temperature (calculated from isentropic relation assuming no chemical reaction during compression process) as well. Thus, the following repeatabilities have been applied to measurements throughout this study.

$$\Delta p_{peak} = \pm 0.015 \text{ MPa (or 15 kPa) and } \Delta T_{peak} = \pm 2 \text{ K} \qquad (2.3.3)$$

The effect of the peak temperature deviation on induction time will be discussed in section 2.4. Heat losses during the compression process result in peak pressure 20-30 % lower than the calculated adiabatic peak pressure for a given compression ratio. Figure 2.3.3 shows the several parameters of the rapid compression machine:

(i) Ratio of the peak pressure to the calculated adiabatic pressure (Fig.2.3.3 (a)).

(ii) Cooling time scale to reach isothermal equilibrium (Fig.2.3.3 (b)).

(iii) Leakage around the gas feeding valve and/or piston head O-ring (*blow-by leakage*) (Refer to Appendix A.1.1 for details).

(iv) Feasibility of experimental method to measure piston and O-ring crevice volumes (Details described in Appendix A.1.2).

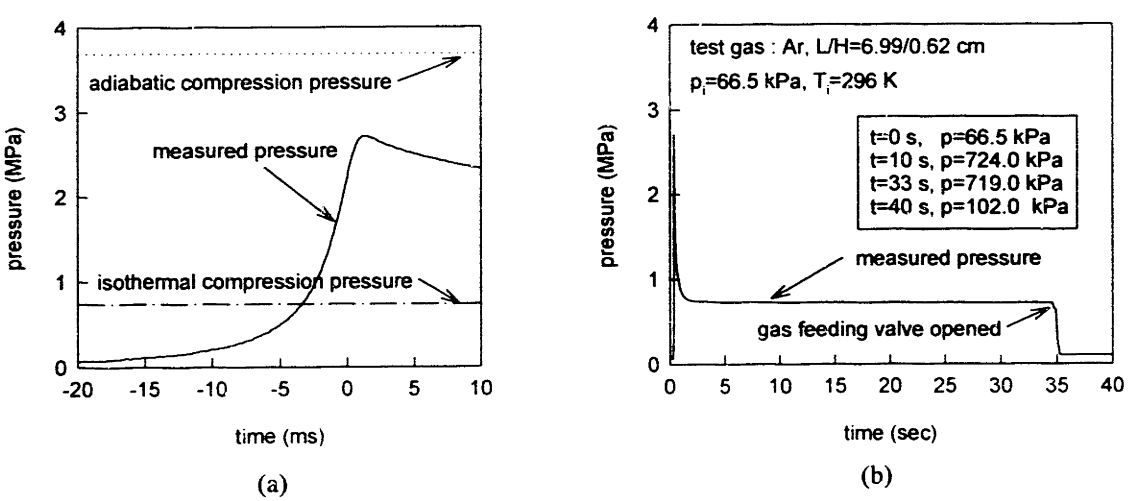

Figure 2.3.3 Measured pressure-time record showing compression and cooling of test gas to the initial temperature. (a) time 0 was shifted to the steepest point during compression process. Measured pressure reaches 74% of the adiabatic compression process. (b) After t > ~5 sec, chamber gas cools down very close to the wall temperature. At t=34s, gas feeding valve is opened.

2.4. Induction time

The *induction time* (definition follows) is derived from a measured pressure-time record. In general, induction times of up to 40 milliseconds have been observed, however, a few measurements up to 100 ms were made for iso-octane autoignition (Lee 1993).

The time interval of interest (*i.e.* the time before flame passage) in a spark ignition engine encompasses as long as 20 ms at moderate engine speeds. Hydrocarbon autoignition (or fuel of interest) may occur mostly within this time interval over a wide temperature range (800-1100 K). The induction time measured in this study involved this induction time range (up to 40 ms). Within these time and temperature ranges, marked changes in the chemical kinetic interactions and energy release can be developed.

Several definitions for *induction time* have been used in the literature (only as applied for *single-stage* ignition or the overall induction time):

(i) Schreiber *et al.* (1993): Time interval between the moment that the piston stops to the moment in the post-compression process when the *maximum pressure gradient* is attained.

(ii) Park (1991) : Time between the intersection of the *steepest* slope with the post-compression pressure and the point during explosion where core temperature is 1100 K.

(iii) Yetter, Rabitz & Hedges (1991) : Time during explosion when d^2T/dt^2 is maximum.

(iv) Ohta *et al.* (1986) : Time measured from the end of compression to the hot flame onset. Regardless of gradual or fast pressure rise during explosion, the hot flame (or red light emission) coincides with very fast rates of pressure rise.

In this study, the induction time is defined as the interval between the moment of *the steepest slope* during compression process to the moment of *the maximum pressure gradient* ($\geq 10^5$ MPa/s, that is, 10 MPa (maximum operating pressure) pressure rise during 0.1 ms) after the

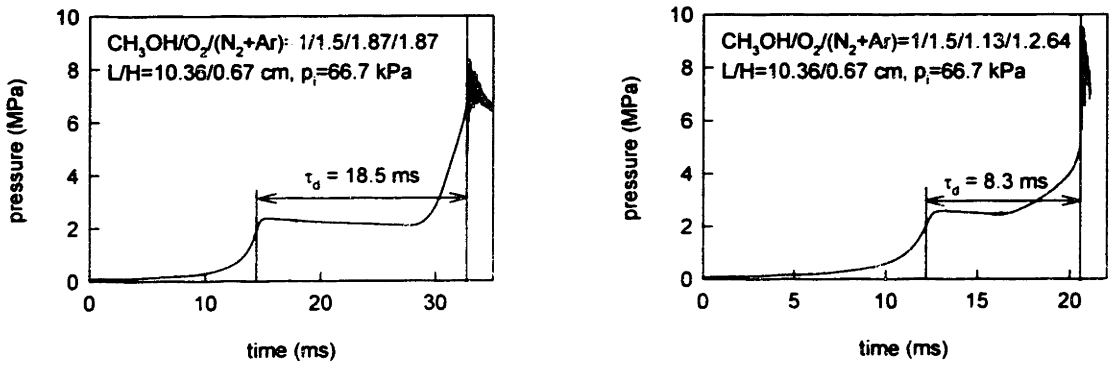

Figure 2.4.1 Measured induction times according to the definition by this study. Induction time is defined as the interval between the moment of the steepest slope during the compression process to the moment of the maximum pressure gradient ($\geq 10^5$ MPa/s) after compression.

compression process. Induction times, calculated from measured pressure profile using the criterion defined as the above, are shown in Fig.2.4.1.

The above four definitions only differ significantly in the starting point of the induction period. Although most of the temperature rise takes place near the end of the compression, when studying relatively short induction times (Fig.2.4.2), chemical reactions which possibly occur during compression should be included. Thus, induction time is calculated from the steepest slope during compression, at which temperature reaches around 850-950 K. This temperature range is not much lower than the peak temperature. This definition also provides a less

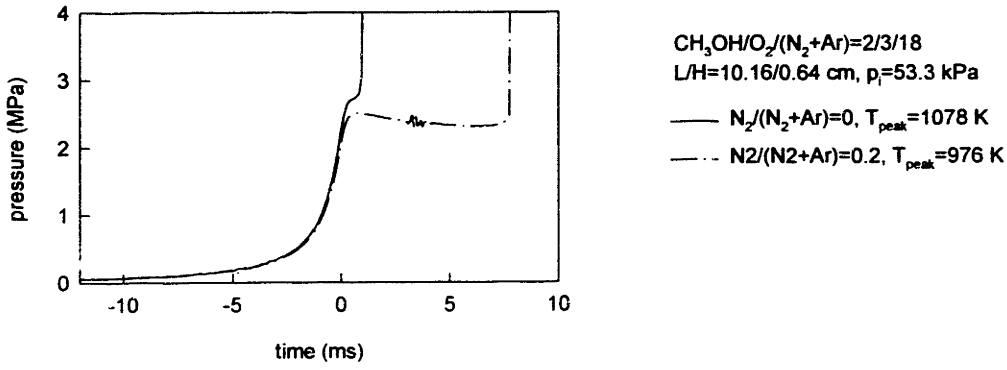

Figure 2.4.2 A comparison of measured pressure-time records when short induction time was observed. Possible chemical reaction during compression process needs to be considered for autoignition study.

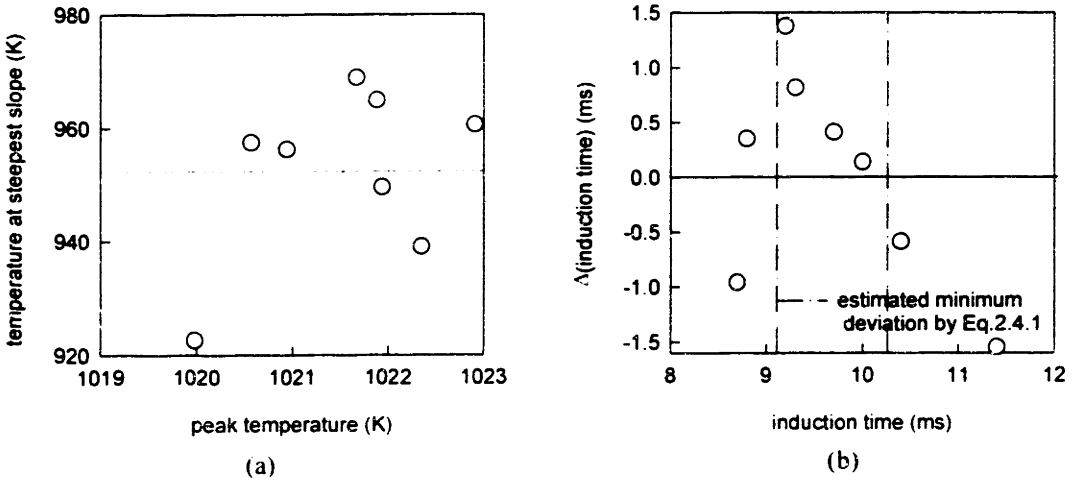

Figure 2.4.3 (a) Comparison between the peak core temperature and the temperature at the steepest slope. (b) Comparison of deviations of induction time derived from measured pressure records. Deviations are compared to the estimated minimum errors. Eight measurements were made at the identical experimental conditions : Test gas was $H_2/O_2/N_2/Ar$ = 2/1/0.175/6.825, L/H = 6.98/0.62 cm. T_i=292.8±0.2 K. p_i=66.7 kPa.

ambiguous point than the peak pressure, which can be non-existent after compression (see Fig.2.4.2). Figure 2.4.3 (a) compares the peak temperature to the temperature at the steepest slope during the compression process. Temperatures at the steepest slope are high enough to affect the overall induction time. The time interval between the occurrence of the steepest slope and the peak point is about 0.9 ± 0.3 ms.

Figure 2.4.3 (b) shows the repeatability (within ± 1.5 ms) of the measured induction time for hydrogen autoignition. The estimation of minimum deviation was performed as follows and compared to the measured deviation. The induction time is approximately

$$\tau_d \sim a\left(\frac{p_{peak}}{RT_{peak}}\right)^b \exp(E_a / RT_{peak}) .$$

Thus, the relative deviation can be given by:

$$\frac{\Delta\tau_d}{\tau_d} = \sqrt{\left(\frac{\partial\tau_d}{\partial p_{peak}}\right)^2\left(\frac{\Delta p_{peak}}{\tau_d}\right)^2 + \left(\frac{\partial\tau_d}{\partial T_{peak}}\right)^2\left(\frac{\Delta T_{peak}}{\tau_d}\right)^2} . \qquad (2.4.1)$$

Measured induction times were close to the estimated minimum deviation, which is limited by the resolution of measuring devices. The results indicate that induction time repeatability is about ± 1.5 ms for hydrogen autoignition.

2.5. Piston crevice*

2.5.1. Piston head crevice

Visualization experiments have shown that a *vortex* motion is observed at the piston face and cylinder wall interface as the cylinder wall moves towards the piston (relative to the piston moving along the wall) as shown in Fig.2.5.1. Nikanjam & Greif (1978) also pointed out that there is some effect on the heat flux due to mixing in the gas resulting from the vortex that forms at the piston-wall interface. Park's (1990) piston head crevice design was a first attempt of suppressing these effects. Comparison of simulated and experimental results (will be discussed in chapter 4) showed that suppression was not achieved with that initial design.

Figure 2.5.2 shows a KIVA II simulation of piston vortex with nitrogen gas. The piston head simulated in (a) (same as in Fig. 2.5.3. (a) by Park 1991) shows that the scraped boundary layer may not be successfully captured into piston crevice, although the KIVA II simulation could not reproduce accurately RCM pressure measurements, due to the lack of resolution near the thin boundary layer. In the case of Fig. 2.5.3 (b), in which cross sectional area was increased to 1.5 time that of (a), the corner vortex was swallowed fully into the *piston crevice* and severe fluid motion did not disturb the cylinder gas significantly.

Therefore, it is necessary to optimize the piston crevice in terms of volume and shape. Its surface to volume ratio must be maximized to ensure that the captured mass cools down to the wall temperature as soon as possible in order not to cause any secondary chemical reaction during/after compression process. Ease of modeling, when the condition of mass is well

---

* Piston crevice consists of piston head crevice and piston O-ring crevice.

understood, can be attained as well. Figure 2.5.3 and table 2.5.1 show the piston heads tested in this study.

In figure 2.5.3, piston head #1 was designed by Park (1990) as a first attempt to capture the roll-up boundary layer into piston crevice volume. Piston head #2 has enlarged piston O-ring crevice volume compared to piston head #1, to investigate the movement of O-ring packs along O-ring groove during/after the compression process. Piston head #3 is normal and flat one without piston head crevice except the narrow gap between piston and cylinder wall. This piston head was tested as a limiting case, where vigorous piston corner vortex is presumably generated during the compression process. Piston head #4 has enlarged piston head crevice volume to see the effect by increasing piston head crevice volume, of which configuration has a high surface to volume ratio. Piston head #5 has enlarged wedge shaped crevice compared to piston head #1. This piston head was tested to show that the head crevice volume of piston head #1 was not large enough to accommodate the swallowed volume. Finally, piston head #6 was designed and used by this study to swallow boundary layer and thus implements well-defined gas behavior. Design of the piston head crevice (#6, Fig.2.5.3 (f)) suggested in this study to minimize the generation of piston corner vortex is discussed in the following section.

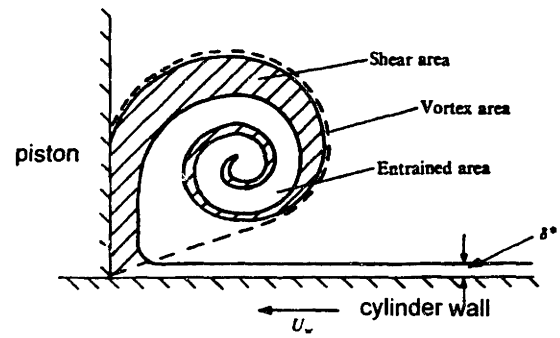

Figure 2.5.1 Sketch of vortex flow (Tabaczynski, Hoult & Keck 1970).

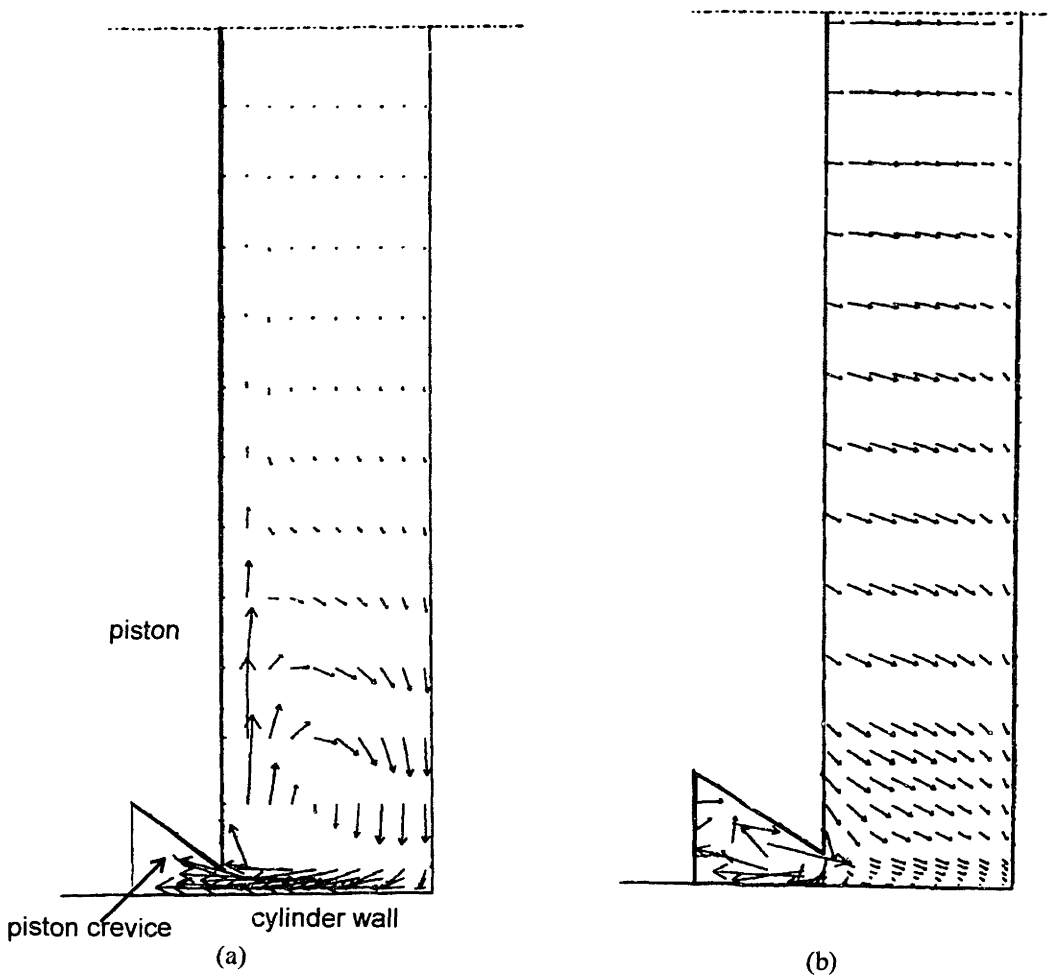

Figure 2.5.2 Simulation of piston corner vortex by KIVA II on a 20X40 mesh (dense near the wall). The sectional area of the crevice for (b) was increased 1.5 times of that of (a), which is same as in Fig.2.5.3 (a). The piston speed and time of travel was matched to that of rapid compression machine measurement. Test gas was nitrogen.

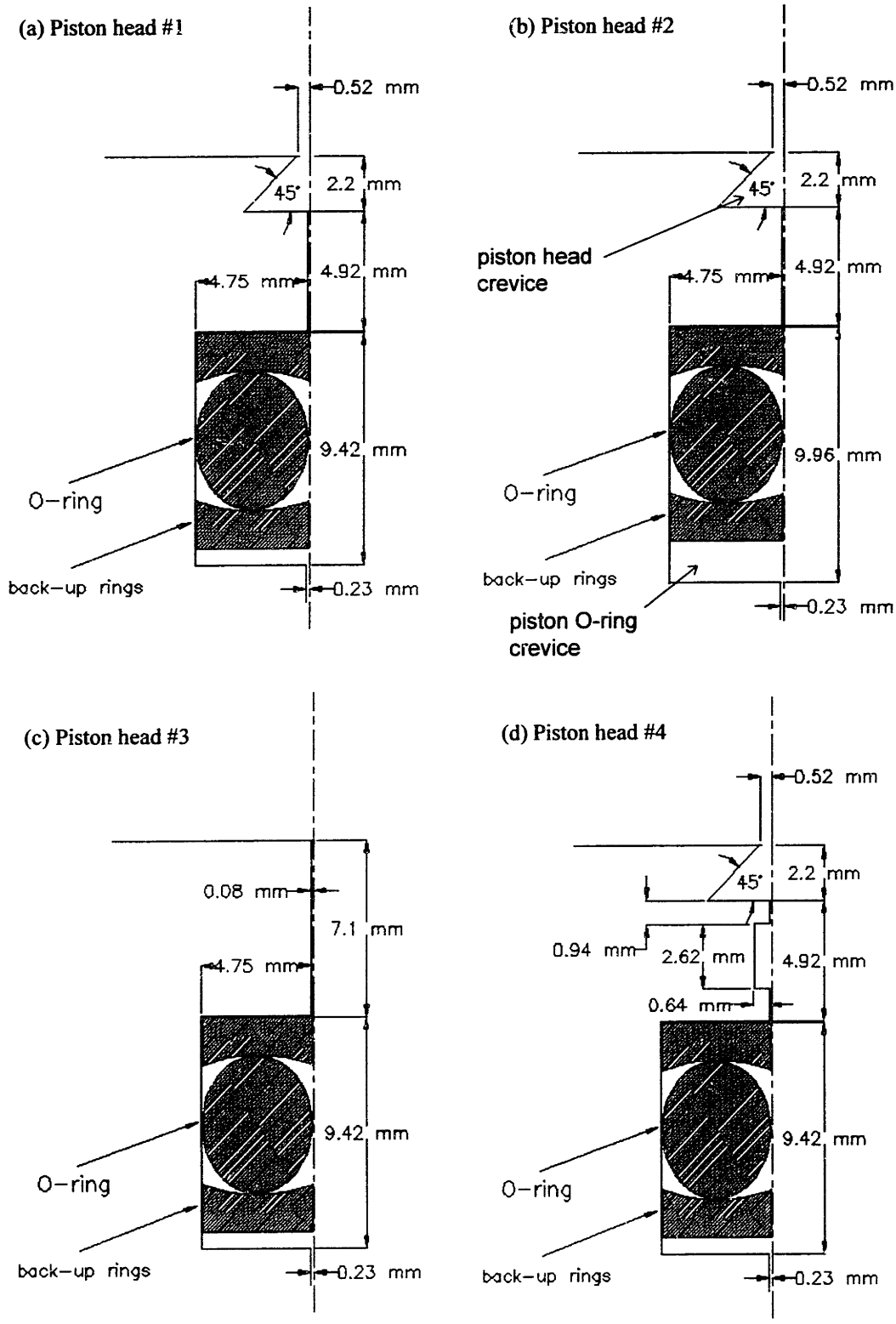

Figure 2.5.3 Configuration of piston heads.

(continued)

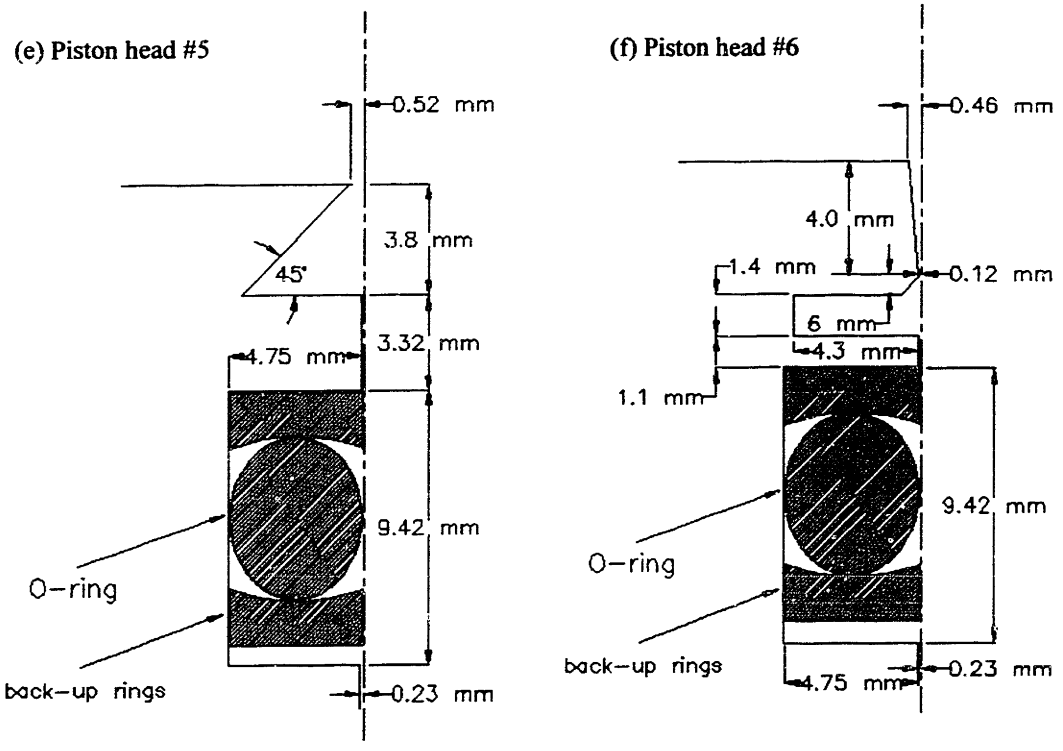

Figure 2.5.3 *(Continued)*

Table 2.5.1 A comparison of piston head crevice volume. Piston head no. corresponds to the configurations of piston head in Fig. 2.5.3.

piston head no.	configuration	crevice volume (cm^3)	remarks
#1	wedge shaped crevice	0.728±0.220	Fig. 2.5.3 (a) (Park 1991)
#2	enlarged (*w.r.t.* #1) O-ring groove : to investigate movement of O-ring packs	0.728±0.231	Fig. 2.5.3 (b)
#3	flat piston head : to compare with the limiting case	0.264±0.231	Fig. 2.5.3 (c)
#4	enlarged gap (*w.r.t.* #1) : to see effect by changing crevice volume	0.993±0.271	Fig. 2.5.3 (d)
#5	enlarged wedge shaped crevice (*w.r.t.*#1) : to see effect by changing crevice volume	1.520±0.234	Fig. 2.5.3 (e)
#6	isothermal piston crevice : to design isothermal piston crevice	1.318±0.142	Fig. 2.5.3 (f)

2.5.2. Design of an isothermal piston crevice

During and after a compression process, generation of a *piston corner vortex* must be avoided in order to prevent uncertainty caused by mixing of cold thermal boundary layer and hot reacting gas. More quiescent conditions in the reacting mixture can be attained by capturing the scraped thermal boundary layer into a piston crevice and suppressing the corner vortex. Note that the fluid boundary layer is thinner than thermal boundary layer at conditions of interest, since the Prandtl number is less than one. While the piston is moving along the cylinder wall and the scraped thermal boundary layer is successfully being captured into a piston crevice, the captured volume in a piston crevice must quickly reach thermal equilibrium with the wall, i.e., *isothermal* status. This is necessary not only to ease modeling heat transfer characteristics of the RCM, but to reject any possibility of chemical reaction occurring in a piston crevice. The determination of a piston crevice volume was performed based on the following design criteria :

(a) Developed thermal boundary layer should be captured fully into a piston crevice volume.

(b) Captured gases should cool down to the wall temperature as soon as possible.

(c) Piston crevice volume should be minimized not to reduce compression ratio.

All dimensions are based on the worst case scenario, i.e., for the maximum stroke, highest pressure associated with maximum specific heat ratio and the thickest thermal boundary layer.

The model used to calculate the optimal piston crevice volume in order to capture the scraped thermal boundary layer is shown in Fig. 2.5.4. During the compression process the mass to be captured in the piston crevice volume is calculated to be

$$m_{cr} = \int_0^{t_{cmp}} \left(\int_0^d 2\pi r' \rho' dy' \right) v dt \qquad (2.5.1)$$

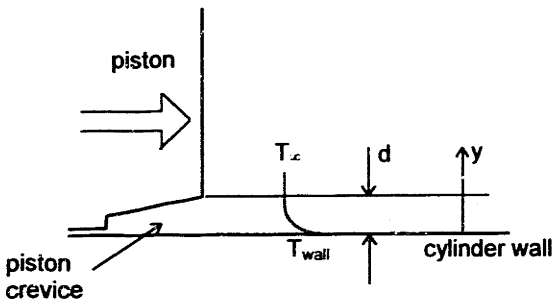

Figure 2.5.4 Schematic of model to calculate piston crevice.

where ρ is the density of gas mixture entering the piston crevice, d is the height of entrance gap of piston crevice and v is the piston speed.

When the compression process is completed, this mass (consisting of thermal boundary layer and region external to the thermal boundary layer up to the overall height of d) is assumed to equal to the mass accumulated in a piston crevice which is assumed to be at the wall temperature. Thus, the piston crevice volume can be calculated from the following relation :

$$V_{cr} = \frac{m_{cr}}{\rho_{peak}}$$

$$= \frac{m_{cr}}{p_{peak} / RT_{wall}}$$

$$= \frac{v}{p_{peak} d} \int_0^{t_{cmp}} \left(2\pi r' \int_0^d p \frac{T_{wall}}{T'} dy' \right) dt \qquad (2.5.2)$$

where $r'=r'(y)$ is the radial dimension of cylinder as a function of y. That is, $r'(y=0)$ is the radius of cylinder. The gas constant was assumed constant throughout the thermal boundary layer. The temperature profile will be calculated and the model will be validated in the following chapter. Validation of this piston head crevice design will be discussed as well. The configuration of piston crevice is described in Fig.2.5.3 (f).

2.5.3 Piston O-ring crevice

An *O-ring* seals the gas by blocking any potential leak path of a fluid (liquid or gas) between two closely spaced surfaces. As the two surfaces are brought together, forming a gland, they squeeze the cross section of the O-ring. This squeezing action results in a deformation of the O-ring cross's section. In applications where higher pressure is exerted by the confined fluid, the O-ring is forced to the side of the gland, away from the pressure. As it is pressed against the side, the O-ring's cross section is deformed into a "D" shape. The elastomer exerts equal force in all directions and is forced up to (but not into) the gap between the mating surfaces. *Back-up rings*, made from a material harder than the O-ring, are often used to prevent extrusion in high pressure applications and designed to fit in the downstream side of the groove, close to the clearance gap in order to provide support for the O-ring.

The configuration of O-ring and back-up ring installed along piston head to seal the gap between the piston and cylinder wall are shown in Fig.2.5.5. The motion of O-ring packs *during* and *after* the compression process inside a groove can be understood from the operating oil pressure around the piston O-ring packs as shown in Fig.2.2.4. The hypothesis of O-ring pack position was shown in Fig.2.5.6. *During* the compression process, the O-ring pack was assumed to be at position pictured in (b) not in the free position pictured in (a), since the hydraulic oil

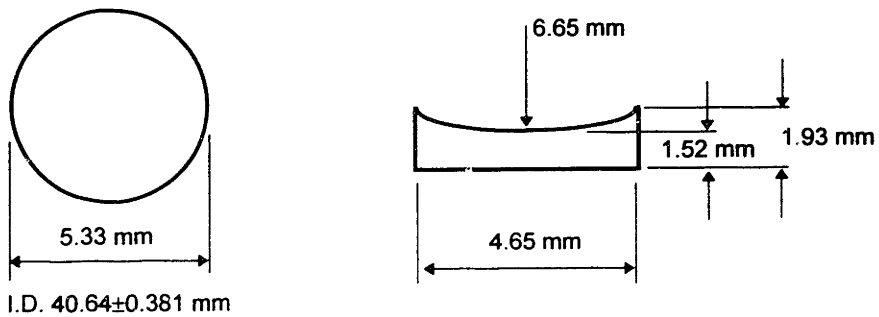

(a) Cross sectional view of O-ring (2-326) (b) Back-up ring

Figure 2.5.5 Configuration of piston O-ring and back-up ring (not to scale).

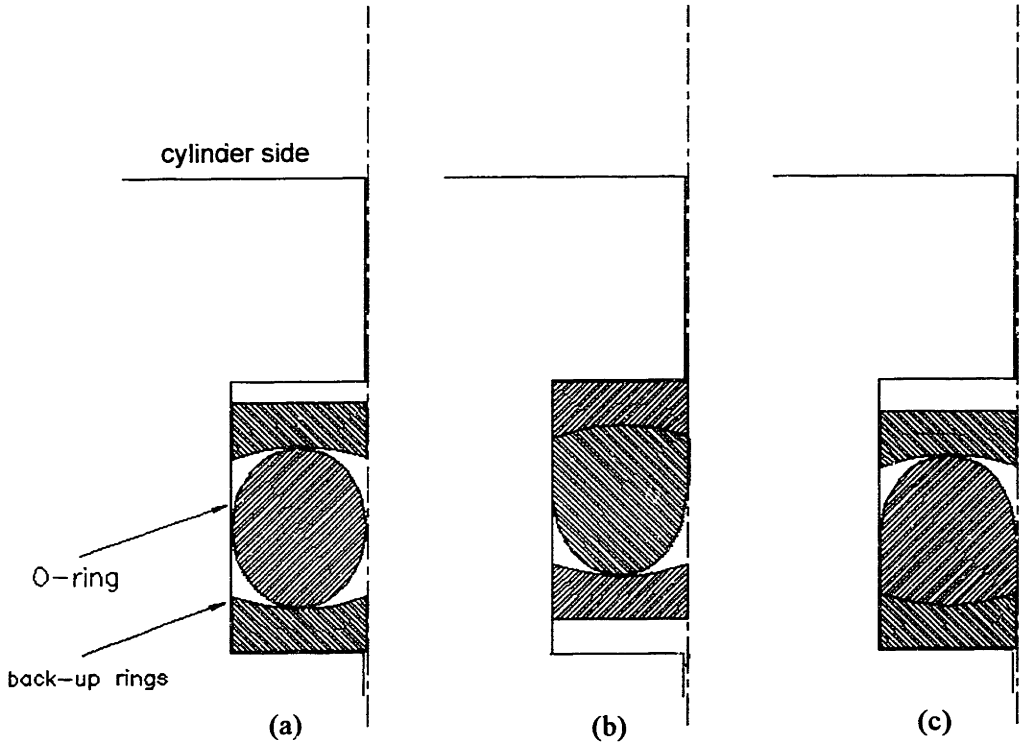

Figure 2.5.6 Hypothesis of O-ring positions. (a) free position, (b) during the compression process and (c) after the compression process. It is noted that back-up ring is not for sealing.

pressure is much higher than cylinder pressure at this moment. *After* the compression process, the hydraulic oil pressure is released to ambient pressure (refer to Fig.2.2.4 regarding time span) while the cylinder pressure maintains a higher pressure. Therefore the O-ring pack is squeezed away from high pressure side toward the other side (relative to the initial position) of the O-ring groove as shown in Fig.2.5.6 (c), since back-up rings do not seal the groove and the O-ring is squeezed and deformed away from the higher pressure side to fill the groove. Based on this hypothesis, the O-ring crevice volume* was calculated as follows: $V_{\text{o-ring crevice}} = 0$ ($t \leq t_{cmp}$, *i.e. before* the peak) and $= 1.37\ cm^3$ ($t >> t_{cmp}$, *i.e.* after the compression process). Validation of this hypothesis by experimental data is discussed in Appendix A.1.2.

---

* Unoccupied O-ring groove volume by O-ring and back-up rings at cylinder side.

2.6 Piston motion

In the design of the RCM's piston motion, extreme rates of deceleration were minimized for the purpose of mechanical reliability, and the maximum piston speed was limited in order to avoid compressibility effects and transition to turbulence (Park 1990, Affleck & Thomas 1968). In most numerical studies of the rapid compression machine, the mechanical motion of the piston was simulated by a constant piston speed. However, piston displacements were calculated (Park 1990, Affleck & Thomas 1968) and measured (Nikanjam & Greif 1978). A comparison of typical displacement profile is shown in Fig 2.6.1.

As discussed in section 2.4, chemical reaction may not be negligible near the end of compression, because most of temperature rise takes place near the end of compression. For this reason, the piston motion was assumed to accelerate rapidly to a constant velocity, and

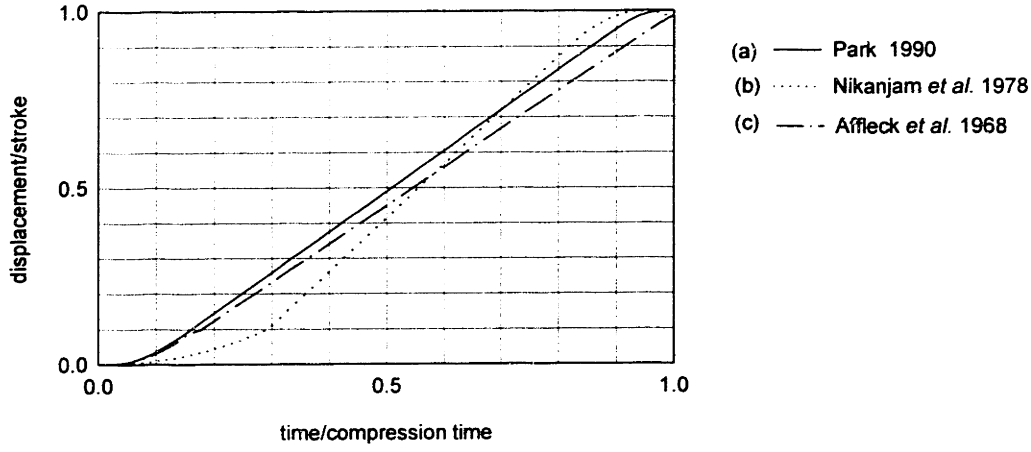

Figure 2.6.1 A comparison of piston motions in normalized displacement and time scale

	(a)	(b)	(c)	
stroke, L (mm)	78.4	130	165.1	
τ_{cmp} (ms)	20	30	13	7
average piston speed (m/s)	4	4.3	12.7	23.6
bore (mm)	5.08	38	38.1	
clearance height, H (mm)	6	38	38.1	
air driving pressure (MPa)	2.07		1.38	3.45
Reference	Park 1990	Nikanjam 1978	Affleck 1968	

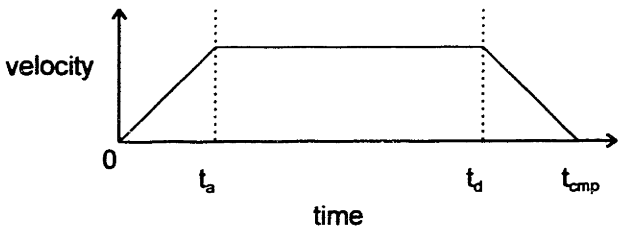

Figure 2.6.2 Velocity profile assumed to calculate piston motion.

decelerate at equal rate. The velocity profile is shown above and acceleration and deceleration times were assumed to be 10% of compression time. The displacements during acceleration and deceleration duration were assumed to be 10 % of the stroke respectively. Figure 2.6.3 shows a comparison between measured pressure profile and calculated pressure (Details of the calculation is discussed at the following chapter). The resulting pressure profile accurately describes the assumed performance of the piston motion in terms of pressure profile. Note that the temperature difference calculated at t=0 (the steepest slope during compression) is significant depending on piston motion. Compression time is derived from measured pressure-time records and correlated in an empirical relation. Refer to appendix A.3.3 for the derivation of compression time from measured data.

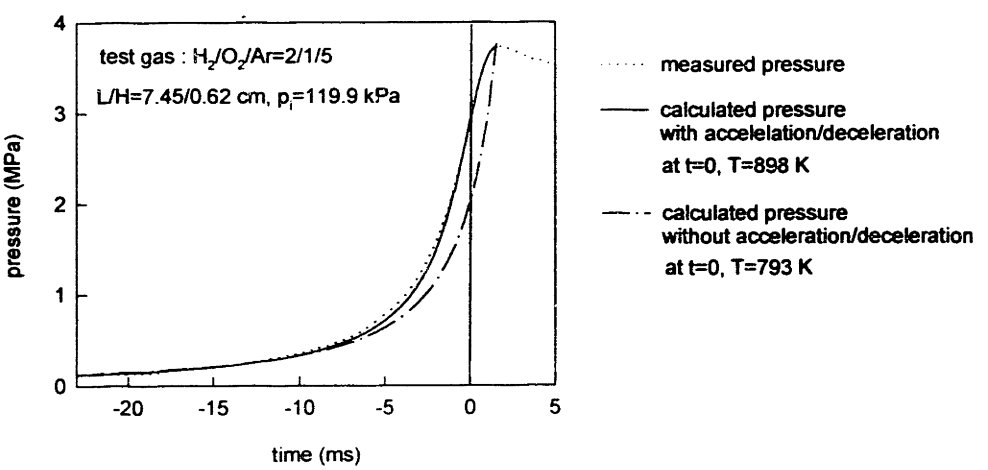

Figure 2.6.3 Calculated pressure profiles during compression process. A comparison was made between zero acceleration/deceleration and 10 % acceleration/deceleration in terms of compression time and stoke. Temperatures at t=0 were calculated for both cases.

CHAPTER 3. THERMODYNAMIC MODEL

3.1. INTRODUCTION

The study of autoignition characteristics of fuel-oxidizer mixtures in rapid compression machines (RCMs) requires accurate characterization of the *core gas*[1] region, where most of the reaction occurs. As discussed in the previous chapter, in most RCMs the core temperature is not uniform, because it is disturbed by the roll-up of the *thermal boundary layer*[2]. The present device avoids that effect — and hence creates well defined core conditions — by virtue of its piston head crevice, which can contain the thermal boundary layer. A new piston head crevice design employed in the present RCM was discussed in Ch.2, in which the growing cold boundary layer is stored during the compression process. It is assumed then that there exists a reaction *core* at a uniform temperature, a *thermal boundary layer* that grows as heat is conducted away to the cold walls, and a nearly *isothermal crevice* region where mass from the scraped thermal boundary layer is stored. In order to verify this, a simple heat transfer model has been developed that includes the effects of heat transfer and piston crevice volume. This model was combined with a chemical kinetic model to simulate the effect of heat transfer on the core temperatures during autoignition. In this chapter, the model's assumptions and the derivation of equations will be discussed. Results, calculated to understand the behavior of gas mixture during and after

---

1 The region where temperature gradients are almost uniform, *i.e.*, what is not confined to the growing thermal boundary layer.

2 The region where temperature gradients (resulting from a heat exchange process between the gas and the wall) are present in a cylinder.

compression process, will be shown as well. Comparison of model predictions and measurements of the pressure history in a rapid compression machine will be presented at the following chapter.

3.2. OBJECTIVES

In order to adequately model the detailed chemical kinetics of the reacting system for comparison with experimental measurements, the state of the reacting mixture must be accurately known. If induction times are relatively short, heat losses can be neglected, as some investigators have assumed. In this case, a constant volume reaction model is adequate, and a more complex chemical kinetic model can be used in simulations (Carlier *et al.* 1990). At the other extreme, detailed fluid motion can be modeled using multidimensional computations coupled with a relatively simple chemical kinetic model (Halstead *et al.* 1977, Griffiths *et al.* 1992). In either case, the highly temperature sensitive nature of chemical kinetics requires precise understanding of the core gas behavior, since most of the reaction takes place there.

The objective of this part of work was to:

(i) Develop a simple one dimensional analytical model for the heat transfer and autoignition during compression, based solely on knowledge of the geometry of the chamber, the compression time and gas properties.

(ii) Verify the accuracy of such a model against experimental data obtained by using flat piston head (see Fig.2.5.3 (c)) and crevice-containing piston (see Fig. 2.5.3 (f)) over a range of conditions which are typical of autoignition. (*will be discussed in the following chapter.*)

In this study, a general unsteady heat transfer model was incorporated into the usual chemical kinetic rate integration procedure, thus allowing for calculation of the temperature and

pressure drop that accompany heat transfer after peak pressure is reached. A discussion of model equations is found in the following section.

3.3 THERMODYNAMIC MODEL

In a RCM, the gas is compressed by the piston motion to the final position within milliseconds. Fig. 3.3.1 shows a typical measured pressure profile during and after the compression process. Clearly, there is a significant pressure (and corresponding temperature) drop due to heat losses through the cylinder walls before autoignition, when the pressure rapidly increases, take place.

During the compression process, the temperature increases in the core region away from the walls, while a thermal boundary layer develops between the wall temperature and the core temperature. The crevice on the piston head was designed to accommodate the mass of the boundary layer as compression proceeds. After the compression process, the piston is locked into place and the mixture is slowly cooled by conduction to the walls.

The model is based on the fact that the thermal boundary layer is relatively thin compared to cylinder dimensions during compression and prior to autoignition, a similar approach to that taken by Keck (1981). Experimental pressure profiles (Fig. 3.3.1) indicate that

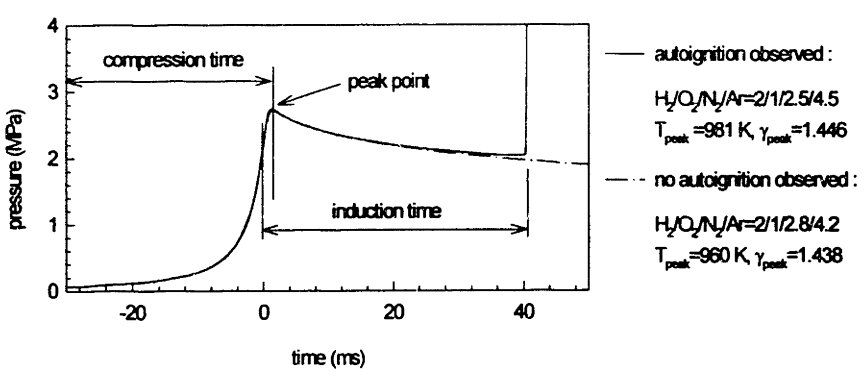

Figure 3.3.1 Measured pressure profiles for hydrogen autoignition. p_i=0.067 MPa, T_i=293 K, L=10.07 cm and H=0.62 cm. Induction time measured from t=0 at inflection point during compression process.

for typical experimental conditions, the pressure drops in reacting and non-reacting cases are similar during the most of the induction period, except for the small time period where the energy release becomes significant. Therefore, the growth of the thermal boundary layer as the quiescent gas cools via conduction to the walls can be assumed to be unaffected by the reactions taking place in the chamber during the induction period. The geometry of the RCM chamber and the associated piston head crevice are shown in Fig. 3.3.2.

3.3.1 Assumptions for thermodynamic model

Assumptions used for the thermodynamic model in the RCM are as follows (verification of each assumption will be discussed in Appendix A.3.2) :

(a) the thermal boundary layer thickness is small compared to the chamber dimensions, so that a one dimensional model can be employed.

(b) no chemical reaction takes place in the boundary layer.

(c) heat transfer is controlled by heat conduction from the core gases to the wall, with no

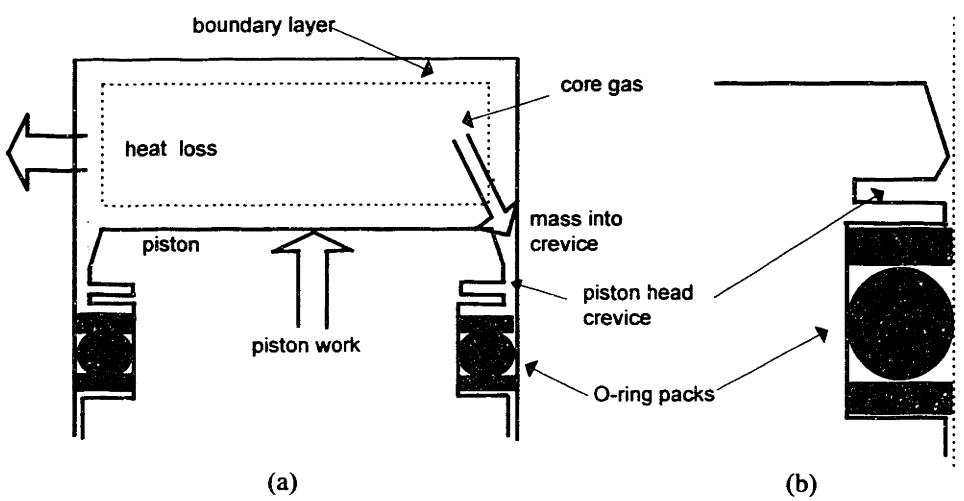

Figure 3.3.2 A schematic of cylinder and piston head crevice.
(a) Definitions for thermodynamic system. Dotted line (·····) indicates core volume.
(b) Configuration of piston head crevice (not to scale, refer to Fig.2.5.3 (f)).

appreciable convective motion along the piston motion.

(d) the thermal boundary layer thickness is smaller than the entrance gap of a piston head crevice, and the length of a crevice is long enough to cool down the entering gas, so that the gas in the piston head crevice is nearly isothermal, at the same temperature as the walls (refer to section 2.5.2).

(e) surface reactions and thermal diffusion are negligible.

(f) pressure is a function only of time.

(g) the gas in the chamber obeys the ideal gas law.

(h) the chamber walls remains at the initial temperature T_i.

(i) the ratio of specific heats (γ) is a function only of temperature.

(j) the gas constant R is uniform : $R_\infty = R_{bl} = R_{cr} = R$.

(k) the piston head crevice consists of the volume between the piston and the cylinder wall, above the O-ring packs which seal the combustion chamber (Fig. 3.3.2).

The equations for the evolution of the pressure and temperature based on above assumptions are derived at the following section.

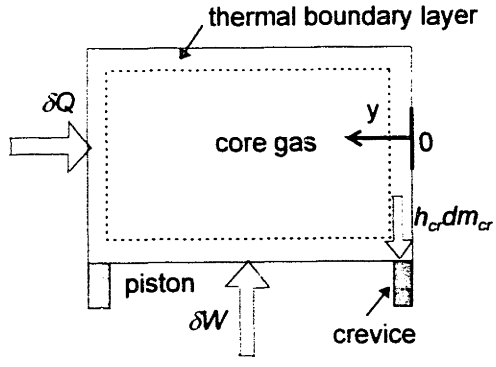

Figure 3.3.3 A schematic diagram of thermodynamic model. $\delta Q(<0)$ represents heat transfer through the wall. $\delta W(<0)$ denotes work done by the system. $h_{cr}dm_{cr}$ represents enthalpy transfer associated with mass going into crevice volume. y is the coordinate direction normal to the cylinder wall.

3.3.2 Model equations

Figure 3.3.3 shows a schematic diagram of the thermodynamic model, which consists of three regions distinguished by thermodynamic characteristics : *core*, *thermal boundary layer* and *piston crevice*. $\delta Q(<0)$ represents heat transfer through the wall. $\delta W(<0)$ denotes work done by the system. $h_{cr}dm_{cr}$ represents enthalpy transfer associated with mass going into crevice volume and y is the coordinate direction normal to the cylinder wall. Table 3.3.1 represents thermodynamic characteristics of each region.

The energy and mass balance equations are derived for each region and solved simultaneously to yield the pressure history in the chamber, and the evolution of the thermal boundary layer is calculated.

i) *Core* volume

Mass conservation:

$$m = m_{\infty} + m_{bl} + m_{cr} \text{ or } dm_{\infty} = -d(m_{bl} + m_{cr}) \tag{3.3.1}$$

Volume conservation:

$$V = V_{\infty} + V_{bl} \text{ or } dV_{\infty} = dV - dV_{bl} \tag{3.3.2}$$

Energy conservation*:

$$dU_{\infty} = -pdV_{\infty} + h_{\infty}dm_{\infty} \tag{3.3.3}$$

where the internal energy for the core volume can be represented by :

$$dU_{\infty} = d(m_{\infty}u_{\infty}) \tag{3.3.4}$$

and the specific internal energy can be calculated from

---

* *i.e.* it is assumed that energy is transferred reversibly in/out of the core via compression/expansion or mass transfer into the boundary layer.

Table 3.3.1 A comparison of thermodynamic characteristics of each region consisting of system.

	volume	temperature	chemical reaction
core	$V_\infty(t)$	$T_\infty(t)$	*yes*
boundary layer	$V_{bl}(t)$	$T_{bl}(t:y)$	*no*
crevice	V_{cr}=*constant*	T_{cr}=*constant*	*no*

$$u_\infty = \sum_{i=1}^{K} h_i Y_i - \frac{p}{\rho_\infty} \tag{3.3.5}$$

where the specific enthalpy is

$$h_i = h_{f,i}^o + \int_{T_o}^{T_\infty} c_{p,i} dT \tag{3.3.6}$$

Species equation:

$$\frac{dY_i}{dt} = \frac{\dot{w}_i M_i}{\rho_\infty} \tag{3.3.7}$$

State equation:

$$p = \rho_\infty R_\infty T_\infty \tag{3.3.8}$$

ii) *Thermal boundary layer*

Energy conservation:

$$dU_{bl} = \delta Q - pdV_{bl} - h_\infty dm_\infty - h_{cr} dm_{cr} \tag{3.3.9}$$

where conduction heat transfer through the cylinder wall is defined as (temperature gradient will be discussed later).

$$\delta Q = -k_w A(y) \left.\frac{dT}{dy}\right|_{y=0} dt \tag{3.3.10}$$

where A is the area over which heat is being lost; the sum of piston, head and side wall areas. The thermal conductivity, k_w, is evaluated at the wall condition.

Since in a crevice no chemical reaction is assumed to occur (Table 3.3.1), the composition of the mass is frozen and same as initial components. Thus, enthalpy associated with the mass going into/out of a piston crevice volume is defined as (the energy-average

temperature T'_{cr} will be defined later).

$$h_{cr} \equiv \begin{cases} c'_{p,cr} T'_{cr} & dm_{cr} > 0 \\ c_{p,cr} T_{cr} & dm_{cr} < 0 \end{cases}, \tag{3.3.11}$$

The mass in the crevice can be calculated from

$$m_{cr} = \frac{V_{cr}}{R_{cr} T_{cr}} p \quad \text{or}$$

$$dm_{cr} = \frac{V_{cr}}{R_{cr} T_{cr}} dp + \frac{p}{R_{cr} T_{cr}} dV_{cr} \tag{3.3.12}$$

where dV_{cr}=0 during the compression process. Refer to section A.1.2 regarding the displacement of O-ring pack after the compression process.

State equation:

$$p = \bar{\rho}_{bl} \bar{R}_{bl} \bar{T}_{bl} \tag{3.3.13}$$

where the mass average density can be defined as

$$\bar{\rho}_{bl} = \frac{p}{\bar{R}_{bl} \bar{T}_{bl}} = \frac{1}{V_{bl}} \int_0^{\delta_t} \frac{pA(y)}{RT} dy \tag{3.3.14}$$

and the mass average temperature can be defined as

$$\bar{T}_{bl} = \frac{V_{bl}}{\int_0^{\delta_t} \frac{A(y)}{T} dy} \tag{3.3.15}$$

From given t and $V(t)$, dependent variables p, T_∞, δ_t and Y_i can be calculated by solving above equations simultaneously. Finally Eqs.(3.3.1)-(3.3.15) were reduced to (3+K) equations to find (3+K) dependent variables (refer to Appendix A.3.1. for the derivation procedures):

(a) Mass conservation for the total volume including core, boundary layer and crevice volume.

$$\left(\frac{V_\infty}{V} + \frac{V_{bl}}{V} \frac{T_\infty}{\bar{T}_{bl}} + \frac{T_\infty}{T_{cr}} \frac{V_{cr}}{V} \right) \frac{dp}{p} - \frac{V_\infty}{V} \frac{dT_\infty}{T_\infty} - \frac{V_{bl}}{V} \frac{T_\infty}{\bar{T}_{bl}} \frac{d\bar{T}_{bl}}{\bar{T}_{bl}} + \left(1 - \frac{T_\infty}{\bar{T}_{bl}} \right) \frac{dV_\infty}{V} + \frac{T_\infty}{T_{cr}} \frac{dV_{cr}}{V} = 0 \tag{3.3.16}$$

(b) Energy conservation for the core volume:

$$d\left[\left(\sum_{i=1}^{K} h_i^o + \int_{T^o}^{T_\infty} c_{p,i}\,dT\right) Y_i\right] = c_{p,\infty} dT_\infty + \sum_{i=1}^{K} h_i^o\, dY_i$$

$$= \frac{dp}{\rho_\infty} \tag{3.3.17}$$

Note that Eq.(3.3.17) can be reduced as follows in the case that chemical reaction is neglected:

$$c_{p,\infty} dT_\infty = \frac{dp}{\rho_\infty} \tag{3.3.18}$$

or

$$\frac{dT_x}{T_x} = \frac{\gamma(T_x)-1}{\gamma(T_x)} \frac{dp}{p} \tag{3.3.19}$$

which represents the isentropic relation between the core temperature and pressure when the chemical reaction is not involved.

(c) Species equations for the core volume (K equations):

$$\frac{dY_i}{dt} = \frac{\dot{w}_i M_i}{\rho_\infty} \tag{3.3.20}$$

(d) Energy conservation for the boundary layer :

$$\left[\left(\frac{1}{\bar{\gamma}-1}\right)_{bl} \frac{V_{bl}}{V} + \left(\frac{\gamma}{\gamma-1}\right)_{\infty} \frac{V_\infty}{V} + \left(\frac{\gamma}{\gamma-1}\right)_{cr'} \frac{T'_{cr}}{T_{cr}} \frac{V_{cr}}{V}\right] \frac{dp}{p} + \left(\frac{\bar{\gamma}}{\bar{\gamma}-1}\right)_{bl} \frac{dV_{bl}}{V} +$$

$$\left(\frac{\gamma}{\gamma-1}\right)_{x} \frac{dV_x}{V} - \left(\frac{\gamma}{\gamma-1}\right)_{x} \frac{V_x}{V} \frac{dT_x}{T_x} + \left(\frac{\gamma}{\gamma-1}\right)_{cr'} \frac{T_{cr'}}{T_{cr}} \frac{dV_{cr}}{V} = -\frac{1}{pV} k_w A(y) \left.\frac{dT}{dy}\right|_{y=0} dt \tag{3.3.21}$$

where properties T'_{cr} and $\gamma'_{cr'}$ are calculated at conditions denoted in Eq.(3.3.11). T'_{cr} is the energy-averaged temperature for the mass going into (*during compression process*) the isothermal crevice, which can be calculated from: (see Fig.3.3.4)

$$T'_{cr} = \frac{\int_0^d \rho c_p T dy}{\int_0^d \rho c_p dy} = \frac{\int_0^d c_p dy}{\int_0^d \frac{c_p}{T(y)} dy} \qquad (3.3.22)$$

After compression, mass leaves the isothermal crevice, as implied by Eq (3.3.12), since the pressure is decreasing. The mixing, idealized by the one dimensional model, satisfies the mass and energy balances.

Thus, from Eq.(3.3.16), (3.3.17), (3.3.20) and (3.3.21), pressure and core temperature can be calculated from the given time and geometric inputs of piston motion. The following section describes the temperature profile within boundary layer used for this model.

3.3.3 Temperature profile within the boundary layer

In the case that heat transfer is controlled by heat conduction from the core gases to the wall, with no appreciable convective motion along the piston motion taken into account (convective transport in the radial direction *towards* the wall is a result of the temperature gradient and the associated increase in density within the boundary layer), the temperature gradient at the wall can be calculated as was done in the non-reacting, variable time dependent pressure case by Keck (1981):

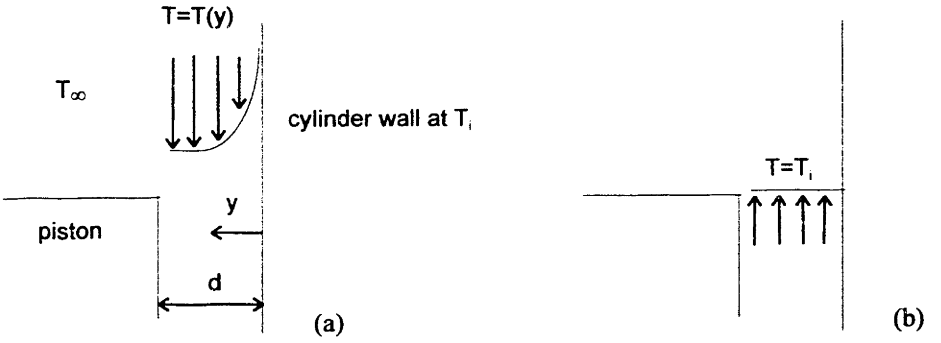

Figure 3.3.4 A schematic diagram showing temperature gradient of the mass (a) *coming into* (during compression process) isothermal crevice. (b) *coming out* (after compression process) of crevice. d is the gap distance between piston and wall.

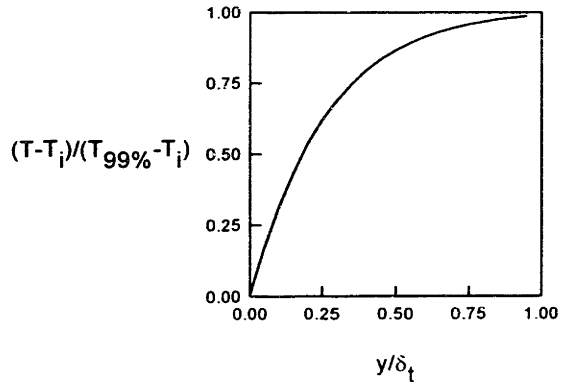

$$\frac{T(y)-T_i}{T_{\infty,99\%}-T_i}=f\left(\alpha_i,\frac{y}{\delta_t}\right)$$

Figure 3.3.5. Non-dimensionalized temperature profile within boundary layer. $T_{99\%}$ denotes that thermal boundary layer thickness was calculated where temperature reaches 99% of the core temperature. Note that the profile is time-independent. $H_2/O_2/Ar=2/1/5$. α_i was calculated at $p_i=0.067$ MPa and $T_i=299$ K.

$$\frac{T(\eta,t)}{T_\infty}=1+\int_0^t erfc\left(\frac{\eta}{2}\left(\alpha_i\int_{t'}^{t}\left(\frac{p^{\cdot}}{p_i}\right)dt^{\cdot}\right)^{-\frac{1}{2}}\right)\frac{d}{dt'}\left(\frac{T_i}{T_\infty'}\right)dt' \tag{3.3.23}$$

where time zero is here the initial time before compression, and the scaled space coordinate was introduced as defined in (Keck 1981) :

$$\eta(x,t)=\int_0^x\frac{\rho'}{\rho_i}dy' \tag{3.3.24}$$

When the temperature and pressure relation in Eq.(3.3.23) is approximately non-dimensionalized, a time-independent profile can be obtained as shown in Fig. 3.3.5.

The profile is only a function of the non-dimensionalized thermal boundary layer thickness and the thermal diffusivity at the initial temperature and density. Note that the thermal boundary layer thickness was defined to be the point where temperature in boundary layer reaches 99% of the core temperature. Table 3.3.2 summarizes the derived model equations.

Table 3.3.2 A summary of derived model equations.

equation	description	remarks
(i) *Core*		
$dm_x = -d(m_{bl} + m_{cr})$	mass conservation	Eq. (3.3.1)
$dV_x = dV - dV_{bl}\ (V = V_x + V_{bl})$	volume conservation	Eq. (3.3.2)
$dU_x = -pdV_x + h_x dm_x$	energy conservation	Eq. (3.3.3)
$dU_x = d(m_x u_x)$	internal energy	Eq. (3.3.4)
$u_x = \sum_{i=1}^{K} h_i Y_i - \frac{p}{\rho_x}$	specific internal energy	Eq. (3.3.5)
$h_i = h_i^o + \int_{T_o}^{T_x} c_{p,i} dT$	specific enthalpy	Eq. (3.3.6)
$\frac{dY_i}{dt} = \frac{\dot{w}_i M_i}{\rho_x}$	species equation	Eq. (3.3.7)
$p = \rho_x R_x T_x$	state equation	Eq. (3.3.8)
ii) *Thermal boundary layer*		
$dU_{bl} = \delta Q - pdV_{bl} - h_x dm_x - h_{cr} dm_{cr}$	energy conservation	Eq. (3.3.9)
$\delta Q = -k_i A(y) \left.\frac{dT}{dy}\right\|_{y=0} dt$	heat conduction	Eq. (3.3.10)
$m_{cr} = \frac{pV_{cr}}{R_{cr} T_{cr}}$	state equation	Eq. (3.3.12)
$h_{cr} \equiv \begin{cases} c'_{p,cr} T'_{cr} & dm_{cr} > 0 \\ c_{p,cr} T_{cr} & dm_{cr} < 0 \end{cases}$	enthalpy associated with mass going into crevice	Eq. (3.3.11)

Equations to be solved

equation	dependent variables	remarks
$\left(\frac{V_x}{V} + \frac{V_{bl}}{V}\frac{T_x}{\bar{T}_{bl}} + \frac{T_x}{T_{cr}}\frac{V_{cr}}{V}\right)\frac{dp}{p} - \frac{V_x}{V}\frac{dT_x}{T_x} - \frac{V_{cr}}{V}\frac{T_x}{\bar{T}_{bl}}\frac{d\bar{T}_{bl}}{\bar{T}_{bl}} + \left(1 - \frac{T_x}{\bar{T}_{bl}}\right)\frac{dV_x}{V} + \frac{T_x}{T_{cr}}\frac{dV_{cr}}{V} = 0$	p, T_x,, δ_t	(3.3.16)
$\left[\left(\frac{1}{\bar{\gamma}-1}\right)_{bl}\frac{V_{b'}}{V} + \left(\frac{\gamma}{\gamma-1}\right)_x \frac{V_x}{V} + \left(\frac{\gamma}{\gamma-1}\right)_{cr'}\frac{T'_{cr}}{T_{cr}}\frac{V_{cr}}{V}\right]\frac{dp}{p} + \left(\frac{\bar{\gamma}}{\bar{\gamma}-1}\right)_{bl}\frac{dV_{bl}}{V} +$ $\left(\frac{\gamma}{\gamma-1}\right)_x \frac{dV_x}{V} - \left(\frac{\gamma}{\gamma-1}\right)_x \frac{V_x}{V}\frac{dT_x}{T_x} + \left(\frac{\gamma}{\gamma-1}\right)_{cr'}\frac{T_{cr'}}{T_{cr}}\frac{dV_{cr}}{V} = -\frac{1}{pV} k_w A(y) \left.\frac{dT}{dy}\right\|_{y=0} dt$	p, T_x,, δ_t	(3.3.21)
Reacting case :		
$d\left[\left(\sum_{i=1}^{K} h_i^o + \int_{T^o}^{T_x} c_{p,i} dT\right) Y_i\right] = c_{p,x} dT_x + \sum_{i=1}^{K} h_i^o dY_i = \frac{dp}{\rho_x}$	p, T_x,, Y_i	(3.3.17)
$\frac{dY_i}{dt} = \frac{\dot{w}_i M_i}{\rho_x}$	Y_i	(3.3.20)
Non-reacting case:		
$c_{p,x} dT_x = \frac{dp}{\rho_x}$ or $\frac{dT_x}{T_x} = \frac{\gamma(T_x) - 1}{\gamma(T_x)}\frac{dp}{p}$	p, T	(3.3.19)

Where temperature profile in boundary layer is $\frac{T(y) - T_i}{T_{x,99\%} - T_i} = f\left(\alpha_i, \frac{y}{\delta_t}\right)$

3.4 RESULTS

The thermodynamic characteristics of the gas mixture calculated by this model are discussed in the following section.

Figure 3.4.1 (a) shows typical results for the calculated and measured pressures for the compression of nitrogen. Compression takes place during about 30 ms, at the end of which peak pressure is achieved. After compression, as heat continues to be transferred through the cylinder walls, the measured pressure drops gradually. The measured time-pressure record was accurately reproduced by the model, both of which are compared with adiabatic compression (Eq.3.4.1) and isothermal compression (Eq.3.4.2)) for reference in Fig.3.4.1 (a).

For adiabatic compression:

$$\ln(\frac{p_{ad}}{p_i}) = \int_{V_i}^{V} \gamma(T)\ d(\ln\frac{V_i}{V}) \tag{3.4.1}$$

and for isothermal compression:

$$\frac{p_{iso}}{p_i} = \frac{V_i}{V} \tag{3.4.2}$$

The isentropic pressure, p_{ad}, was calculated to determine the amount by which the measured pressure deviates from isentropic conditions. In most cases, the peak pressure was within about 20 % of the isentropic value.

Figure 3.4.1 (b) shows the calculated thermal boundary layer thickness during the compression process. The thickness of the thermal boundary layer represents at maximum about 15 % of the clearance height, and its value is comparable to the entrance gap to the piston head crevice (0.046 cm). The thermal boundary layer thickness is here defined at the distance of which the temperature attains 99% of core temperature. The definition of the thermal boundary-

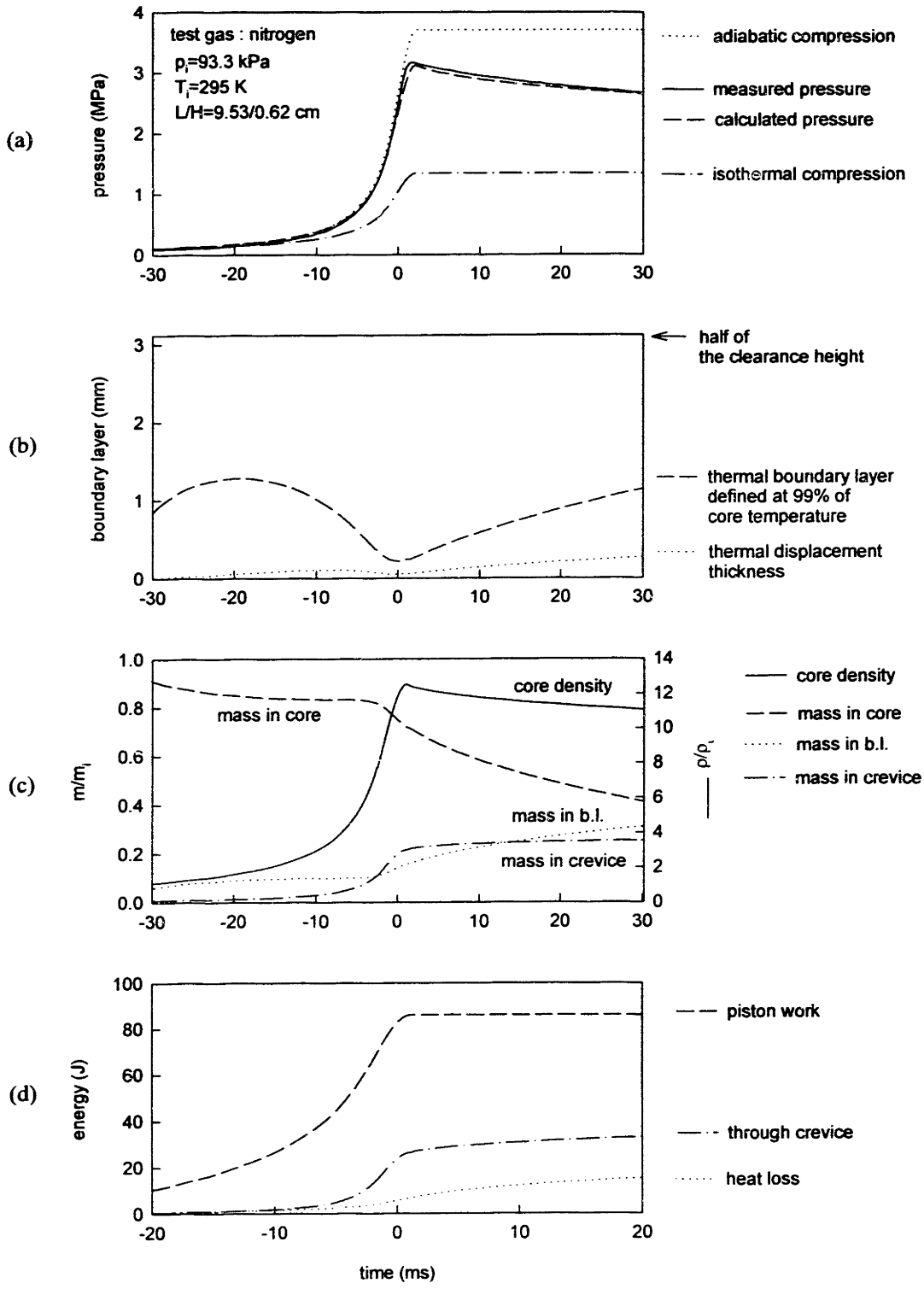

Figure 3.4.1 (a) Comparison between measured pressure and calculated pressure. (b) calculated thermal boundary layer thickness (c) calculated core density, mass in core, crevice and boundary layer. (d) calculated piston work, heat loss through the cylinder wall and energy associated with mass in piston crevice. Test gas: nitrogen. L/H=9.53/0.62 cm, p_i=93.3 kPa, piston head #6 (Fig.2.5.3 (f)).

layer thickness is to a certain extent arbitrary because transition from the temperature in the boundary to that outside of it takes place asymptotically. That is, however, of no practical importance, because the temperature in the thermal boundary layer attains a value which is very close to the core temperature already at a small distance from the wall, where the temperature differs by 1 percent from the core temperature.

As shown in Fig. 3.4.2, thermal boundary layer thickness varies significantly depending on the temperature criterion used to determine its thickness. Also note that the typical magnitude of a Prandtl number (~0.7) during compression process implies that the viscous boundary layer (in which the velocity gradient exists during the compression process) is thinner than the thermal boundary layer thickness. Therefore, since the boundary layer is thin compared to the smallest characteristic dimension of geometry (that is, half of the clearance height), the assumptions for one-dimensional modeling and the design criteria of new piston head (#6) (discussed in section 2.5.2) are valid.

Instead of the thermal boundary layer thickness, another quantity is sometimes used: the thermal displacement thickness δ_d, which is defined in Eq (3.4.3).

$$\delta_d = \int_0^x \left(\frac{\rho}{\rho_x} - 1 \right) dy \tag{3.4.3}$$

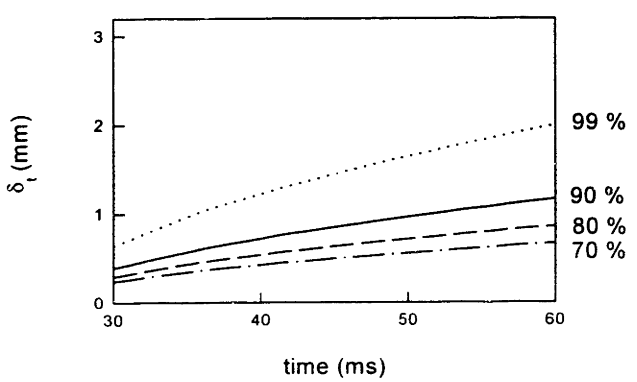

Figure 3.4.2 Comparison of thermal boundary layer thickness as a function of temperature criteria (% to core temperature).

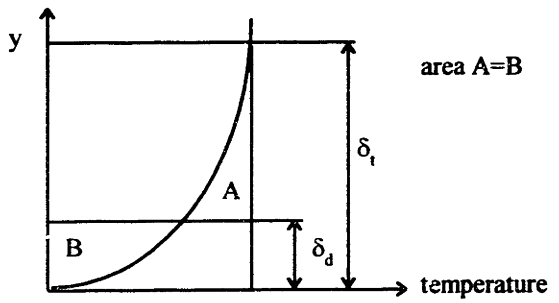

Figure 3.4.3 Displacement thickness δ_d in a boundary layer. Coordinate y is normal to the wall.

The thermal displacement thickness indicates the distance by which the external profiles of temperature are shifted owing to the formation of the thermal boundary layer (see Fig. 3.4.3). In this case, the thermal displacement thickness is about 0.23 times of the boundary layer thickness δ_t (*i.e.*, $\delta_d / \delta_t \sim 0.23$) as calculated from by Eq. (3.4.4).

$$\delta_d = \int_0^{\delta_t} \frac{T_\infty}{T(y)} dy - \delta_t \tag{3.4.4}$$

The calculated thermal displacement thickness is also compared with thermal boundary layer thickness in Fig. 3.4.1 (b).

Figure 3.4.1 (c) shows the evolution of the core gas density and the mass within the core region during and after the compression process. About 80% of the total mass remains within the hot core, the density of which does not change significantly after the compression process. It also shows that a significant amount of mass enters into the piston crevice, which affects thermodynamic characteristics of the cylinder gas. As shown in Fig.3.4.1 (d), energy lost into the crevice is larger than heat loss through the cylinder wall.

The temperature profile in the thermal boundary layer was discussed in section 3.3. Although such temperature profile was assumed from the analysis of thermal boundary layer in a gas subject to time dependent pressure variation (Keck 1981), a slight change in this profile does not significantly alter the overall behavior of calculated core temperature, as shown in

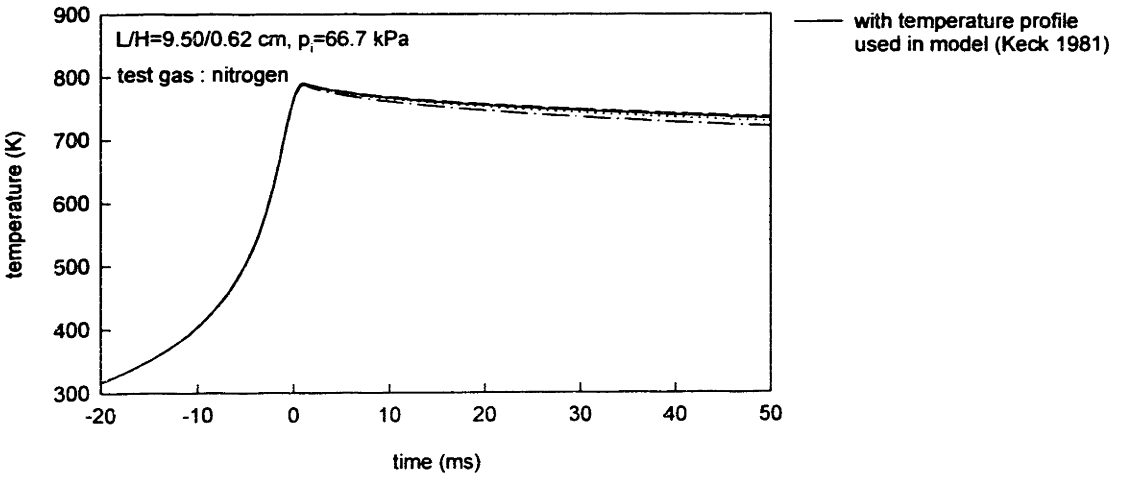

(a) Calculated core temperature variation depending on temperature profile in thermal boundary layer. Each temperature profile is shown in (b).

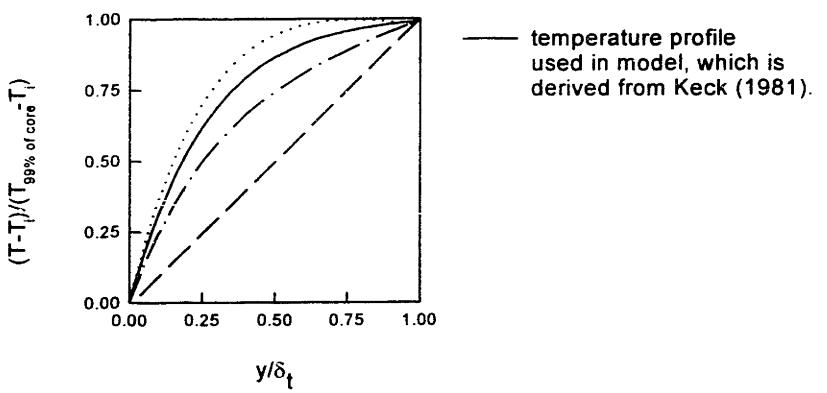

(b) Variations of temperature profile to calculate pressure history in (a).

Figure 3.4.4 Effect of varying temperature profile on core temperature prediction.

Fig.3.4.4(a). The deviation of temperature profiles from the one calculated by the model is not significant, because the thermal boundary layer is thin and the density change in thermal boundary layer is small between each temperature profile (see Fig.3.4.4. (b)).

Also, from the analytical result that mass in thermal boundary layer occupies about 20 % of the total mass (see Fig. 3.4.1 (c)), and the density in thermal boundary layer is larger near the wall (due to lower temperature), it can be shown that the calculated core temperature profiles are

not very sensitive to assumed temperature profile in thermal boundary layer.

The effect of including chemical reaction during compression process on calculating autoignition is analyzed. When the chemical reaction during compression process is included in calculating autoignition, the overall induction time change is small, less than 1 ms as shown in Fig. 3.4.5. Thus, chemical reaction during compression process is excluded in calculation of autoignition for this study. The difference in time between the steepest point (at which induction time starts to be measured for measured data) and peak point (from which chemical reaction is included for modeling of autoignition), which is about 0.9 ms, will be regarded as a known error in calculating induction time. Note that when investigating very high temperature and short induction time, the inclusion of compression process should be considered.

Finally, figure 3.4.6 shows the calculated pressure and temperature profiles. The case with no autoignition is presented in Fig. 3.4.6 (a), in which the temperature drops gradually in a similar way as pressure. In contrast, when chemical reaction is involved due to autoignition, the temperature increases due to energy release during induction time as shown in Fig.3.4.6 (b). As core temperature increase significantly, the pressure begins to increase and show a rapid increase

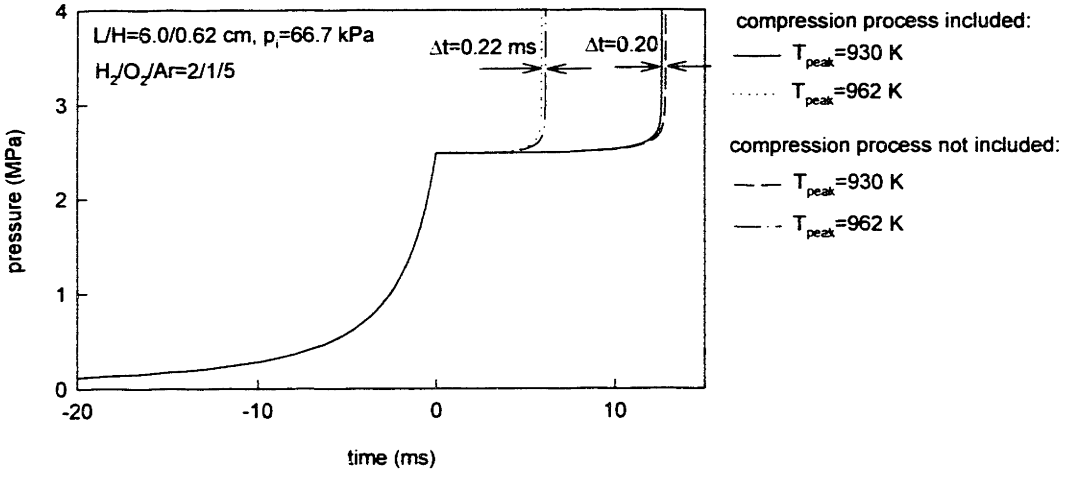

Figure 3.4.5 Effect of including compression process on calculating autoignition. Note that heat loss was not included.

due to accelerating reactions, leading to autoignition. Pressure and temperature calculated with no heat loss are also compared with model in Fig.3.4.6 (b), which apparently shows longer induction time than the adiabatic case. Model verification through measurements will be discussed at the following chapter.

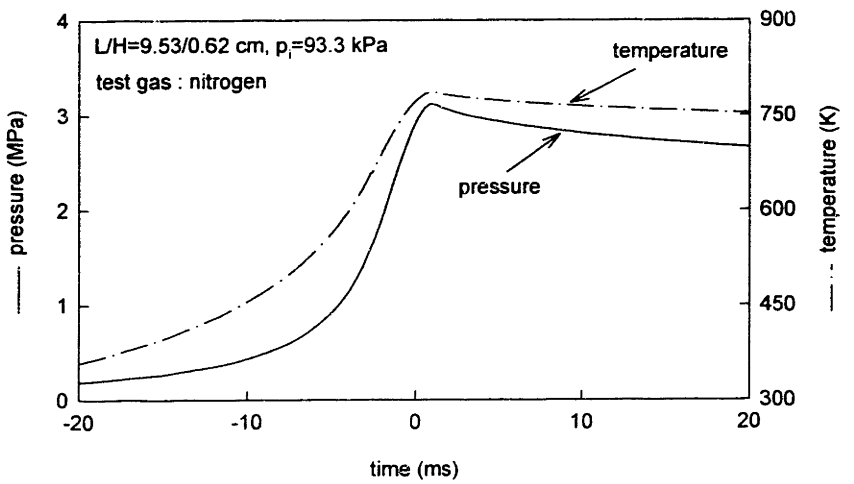

(a) case without autoignition for nitrogen

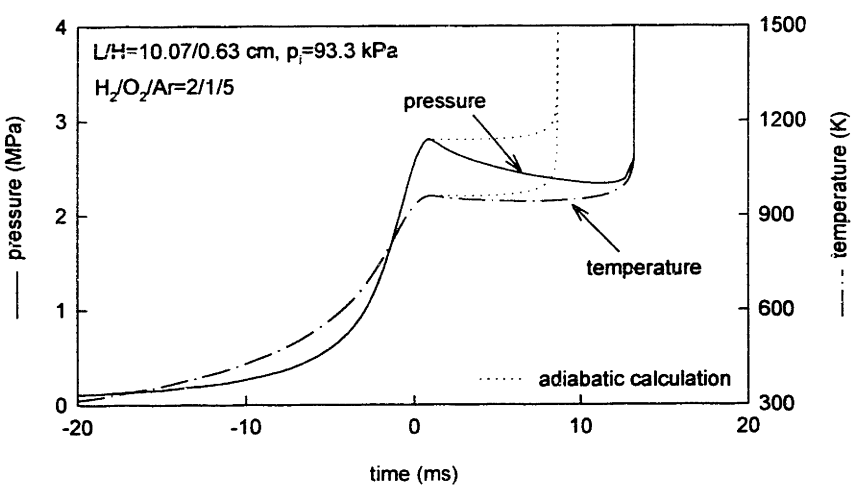

(b) case with autoignition for hydrogen

Figure. 3.4.6 Calculated pressure and core temperature histories for hydrogen autoignition. Note that adiabatic calculation in (b) was performed with peak values as initial conditions.

CHAPTER 4. HEAT TRANSFER CHARACTERISTICS

4.1 Introduction

In most RCMs the core temperature is not uniform, being disturbed by the roll-up of the thermal boundary layer. The present device was designed to avoid such an effect by incorporating a crevice on the piston head that can contain the thermal boundary layer and create well-defined core conditions. In order to verify that this happens, a heat transfer model was developed (as discussed in chapter 3) that maintains simplicity while including the effects of heat transfer and piston crevice volume. The availability of a simple model of heat transfer to determine pressure and temperature drops in the core gas after compression is desirable, since the variation can be incorporated into complex chemical kinetics models without requiring physically unreasonable fits to temperature and pressure (Griffith *et al.* 1993, Halstead *et al.* 1977).

The model also provides insight into an optimized crevice design, which has been implemented (piston head #6 in Fig.2.5.3.(f)). Once the model has been validated, the existence of an adiabatic core (in the case where no chemical reactions are involved) without interference of the thermal boundary layer can be shown to be a plausible assumption, and temperature predictions can be made with confidence. While the model is simple, it has been shown to accurately predict peak pressure and heat transfer rates.

Comparison of model predictions and measurements of the pressure history in a rapid compression machine are presented in this chapter. (Comparisons to the cases *without* autoignition are discussed in this chapter. Chapter 5 deals with the cases *with* autoignition)

4.2 Measured characteristics

The study of ignition delay times in rapid compression machines relies on the ability to estimate reaction temperatures in the chamber with reasonable accuracy, since reaction rates are very sensitive to temperature. The direct measurement of temperatures is not an easy task, given the time resolution required (on the order of milliseconds) and the difficult access to the reaction zone. Therefore, temperatures in the reaction zone prior to ignition must usually be estimated from measured time-pressure records, after making certain assumptions about the processes occurring in the reaction zone during compression. Assuming that most of the reaction takes place in the hottest region of the gas, the core, and that the gas in this region is compressed isentropically (in the case where no chemical reaction is involved), the temperature of the core gas can be calculated as:

$$\ln(\frac{T}{T_i}) = \int_{p_i}^{p} \frac{\gamma(T)-1}{\gamma(T)} d\ln p \qquad (2.2.1)$$

The characterization of the thermal state of the reaction zone in RCMs has been plagued by the fact that, during the compression process, the piston scrapes the colder thermal boundary layer forming along the wall into a vortex, producing non-uniform mixture. As a result, the fuel ignition process in RCMs has been reported to be a spatially non-uniform process characterized by flame kernels growing in a distributed manner throughout the reacting mixture (Furutani *et al.* 1993). A new design for a piston head crevice has been employed in the present RCM as shown in Fig. 2.5.3 (f), in which the growing cold boundary layer is stored during the compression process as the piston moves. The assumption in this case is that there exists a reaction core at a uniform temperature, a thermal boundary layer that grows as heat is conducted away to the cold walls, and a nearly isothermal crevice region where mass from the scraped thermal boundary

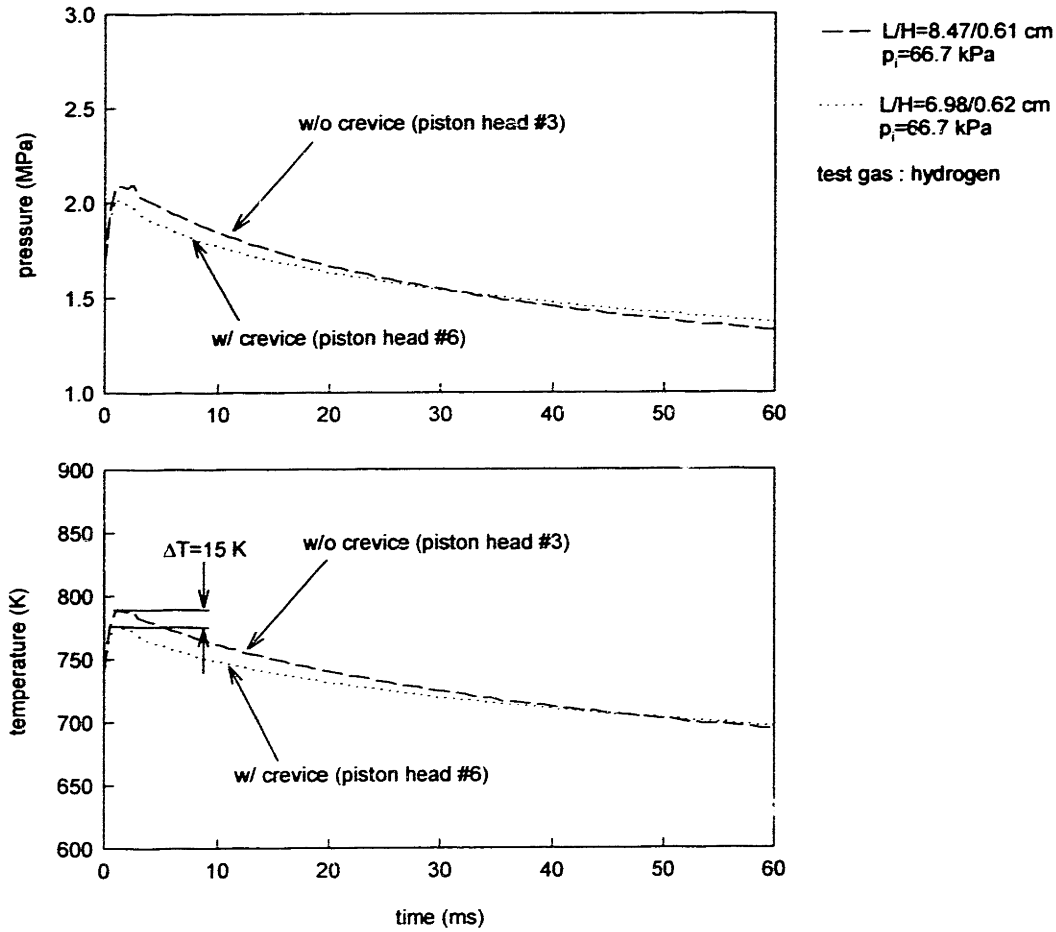

Figure 4.2.1 Comparison of measured pressures and calculated temperatures between piston head #3 (w/o piston head crevice in Fig.2.5.3 (c)) and piston head #6 (w/ piston head crevice in Fig.2.5.3. (f)).

layer is stored.

Comparison between a piston head *with* piston head crevice (#6 in Fig.2.5.3 (f)) and a piston head *without* piston crevice (#3 in Fig.2.5.3 (c)) was performed to investigate the heat transfer characteristics after the compression process. Figure 4.2.1 shows the comparison of calculated core temperature (using Eq.2.2.1) between two piston heads based upon the measured pressure histories. Due to slight difference in compression ratio for each case, the peak core temperature (calculated by Eq.2.2.1 under assumption that an adiabatic core exists in both cases)

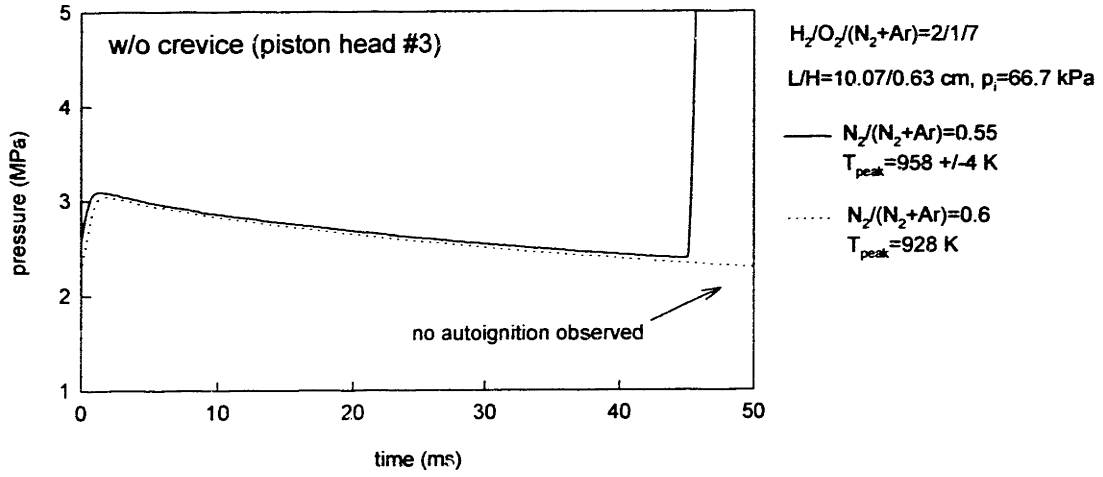

(a) piston head without head crevice (#3)

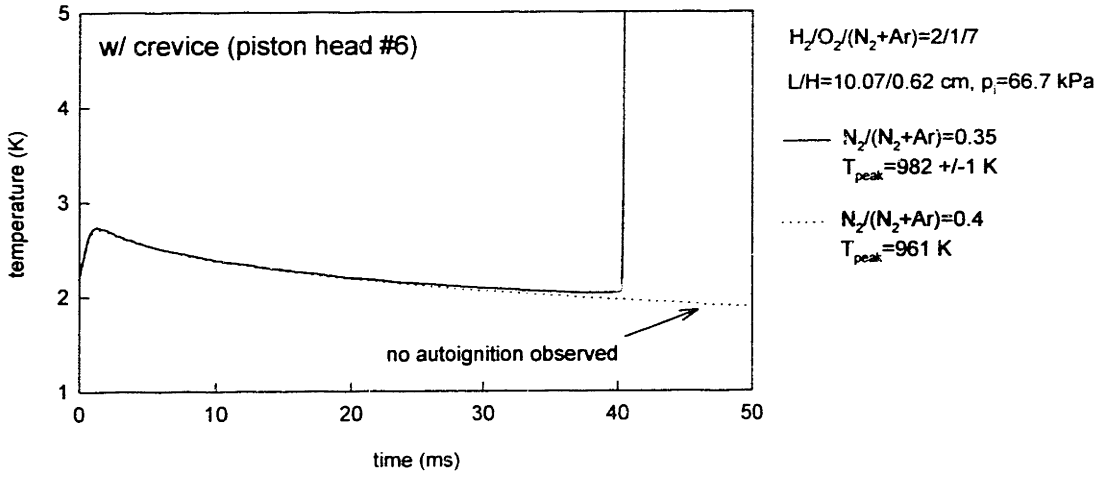

(b) piston head with head crevice (#6)

Figure 4.2.2 Comparison of measured pressure records for hydrogen autoignition between (a) piston without head crevice (#3) and (b) piston with head crevice (#6).

is about 15 K higher for piston head #3 at the peak, however, the cooling rate of the core temperature with piston head #3 is larger than that with piston head #6. Within about 50 ms, both temperatures drop to the same value, which shows that the piston head #3 (flat piston, *i.e.*, without a piston head crevice) enhances the heat loss due to more vigorous fluid motion (presumably by piston corner vortex).

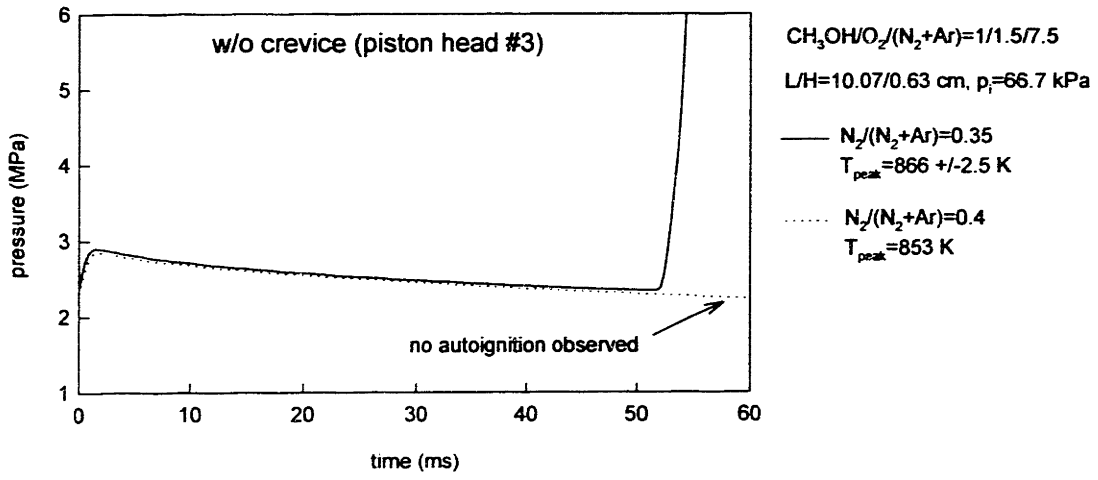

(a) piston head without head crevice (#3)

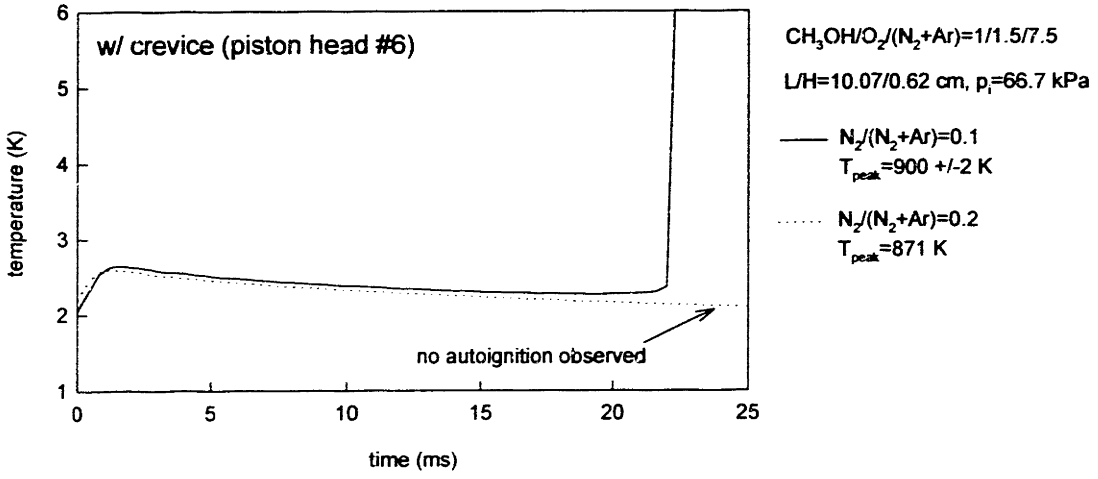

(b) piston head with head crevice (#6)

Figure 4.2.3 Comparison of measured pressure records for methanol between (a) piston without head crevice (#3) and (b) piston with head crevice (#6).

Comparisons between two piston heads (#3 and #6) were made also for fuel and oxygen mixtures. Hydrogen (Fig. 4.2.2) and methanol (Fig. 4.2.3) were tested with each piston head. The results show that, with piston head #3 (without a crevice), the pressure-time records rise very abruptly before autoignition occurs, while with piston head #6 (with a crevice) the pressure rise

(*i.e.*, temperature increase) is more gradual, which is associated with energy release in the form of heat. Vigorous fluid motion in a cylinder chamber, resulting in enhanced mixing between the reaction core and boundary layer, can be a plausible explanation why the piston head #3 shows negligible pressure rise during induction time. Comparison between measurements and model will be discussed at the following section to verify the model in predicting measured pressure histories when chemical reactions are not involved.

4.3 Comparison between measurements and the model

In this section, verification of the thermodynamic model (with *no* chemical reactions) is presented, by comparing model results to measured time-pressure records. Results show that the model is able to reproduce the measured pressure profiles over a wide range of conditions using the specially designed piston.

Figure 4.3.1 shows a comparison between the measured time-pressure record and calculated pressure history using nitrogen. During and after the compression process, the model accurately predicts the measurement. The small discrepancy of the model from the measured profile can be neglected, because the deviations in temperature (inferred from pressure difference) are within the acceptable uncertainty. Figure 4.3.2 (b) shows the comparison for the hydrogen and oxygen mixture in which autoignition is observed.

For the case of the piston head with a crevice, the remarkably good agreement between measurements and computation shows that the piston corner vortex is successfully suppressed

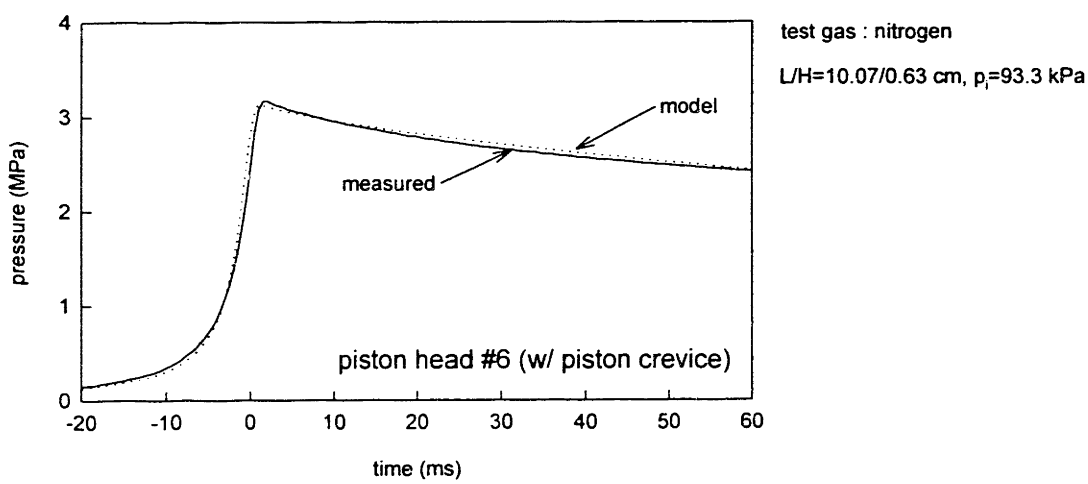

Figure 4.3.1 Comparison between measured pressure records and calculated. Test gas: nitrogen. Piston head with head crevice (#6).

and other effects such as convection associated with piston motion are negligible. Not surprisingly, the calculated pressure for the case without crevice over-predict the pressure measurements (Fig. 4.3.2 (a)), which implies that the measurements with a normal piston head (with no piston crevice) can generate a vigorous corner vortex decreasing the peak pressure, due to enhanced heat loss during compression process.

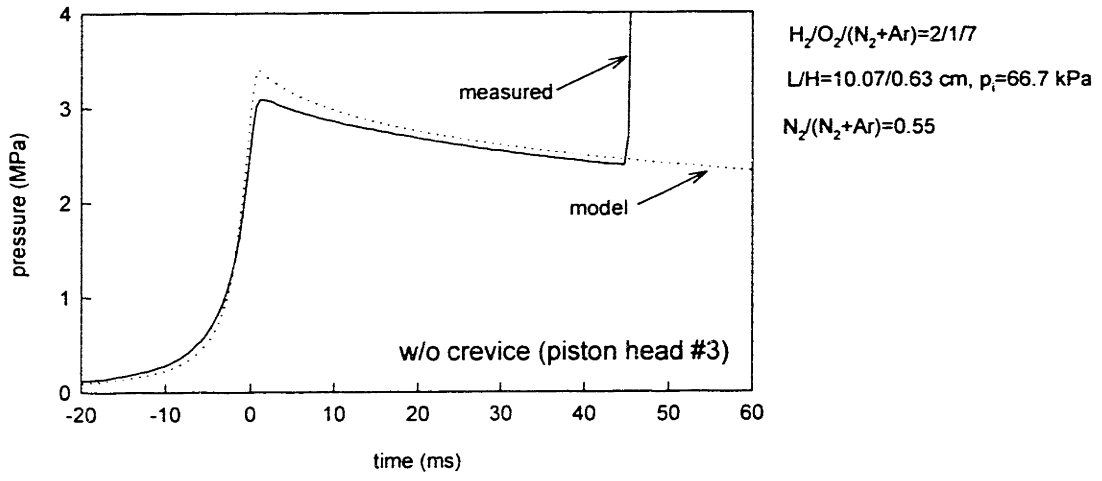

(a) piston head without head crevice (#3)

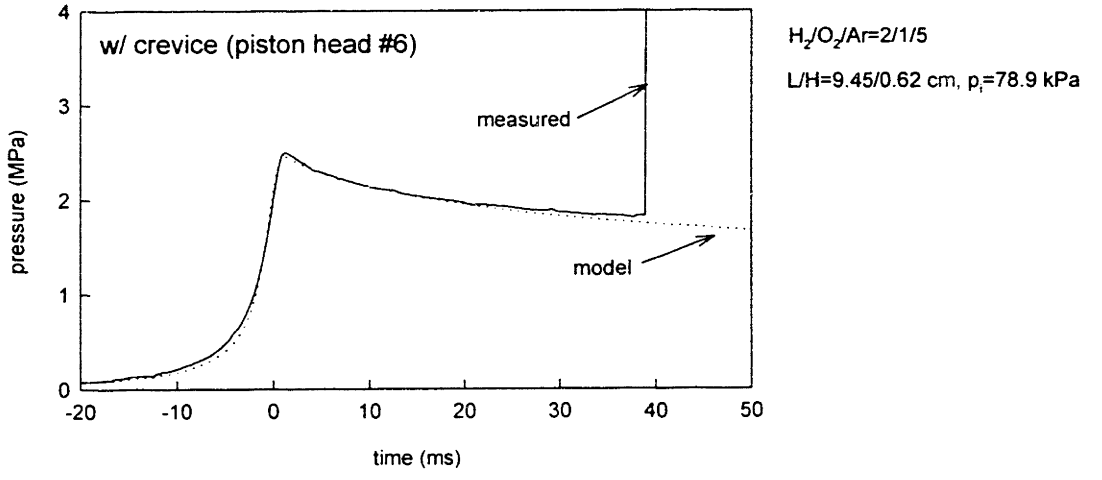

(b) piston head with head crevice (#6)

Figure 4.3.2 Comparison of measured pressure records for hydrogen autoignition between (a) piston without head crevice (#3) and (b) piston with head crevice (#6).

The measured peak pressures at the end of the compression process are compared to the calculated values, for variable stroke lengths and initial pressures, and for nitrogen test gas. Configurations of each piston head tested are summarized in Table 4.3.1 (Refer to Fig. 2.5.3 for detail). Figure 4.3.3 (a) is for piston head #1, which is equipped with wedge shaped piston head crevice (Park 1990). Clearly, model predictions of peak pressure are lower than the measured values, which implies that piston head crevice is not isothermal and consists of gas that is hotter than the wall temperature. As discussed in section 2.5.1 (Fig.2.5.2), computations confirm that the gas entering the crevice is not cooled to the wall temperature sufficiently fast. Additional analysis could be performed to figure out the temperature distribution of captured gas in this piston head crevice. Normal piston head (#3) with no piston crevice was tested and the results are shown in Fig. 4.3.3 (b). Enhancement of heat loss by vigorous fluid motion (presumably due

Table 4.3.1 Summary of piston head configuration. (Refer to Table 2.5.1 and Fig.2.5.3 for detail)

piston head no.	configuration	crevice volume (cm^3)	remarks
#1	wedge shaped crevice	0.728±0.220	Fig. 2.5.3 (a) (Park 1991)
#3	flat piston head : to compare with the limiting case	0.264±0.231	Fig. 2.5.3 (c)
#4	enlarged gap (*w.r.t.* #1) : to see effect by changing crevice volume	0.993±0.271	Fig. 2.5.3 (d)
#5	enlarged wedge shaped crevice (*w.r.t.*#1) : to see effect by changing crevice volume	1.520±0.234	Fig. 2.5.3 (e)
#6	isothermal piston crevice : to design isothermal piston crevice	1.318±0.142	Fig. 2.5.3 (f)

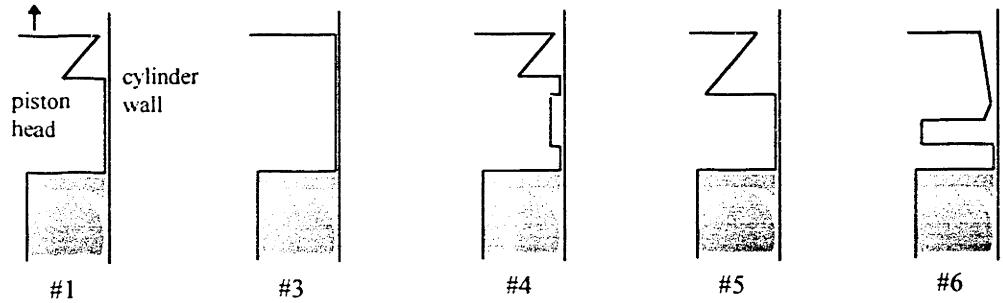

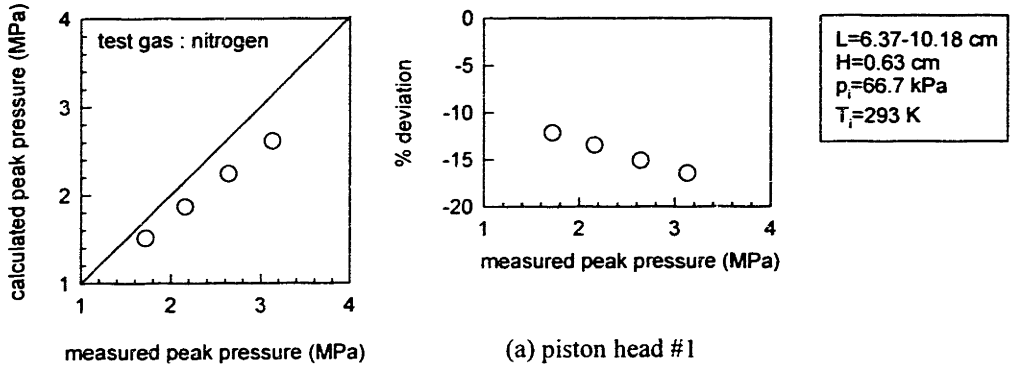

(a) piston head #1

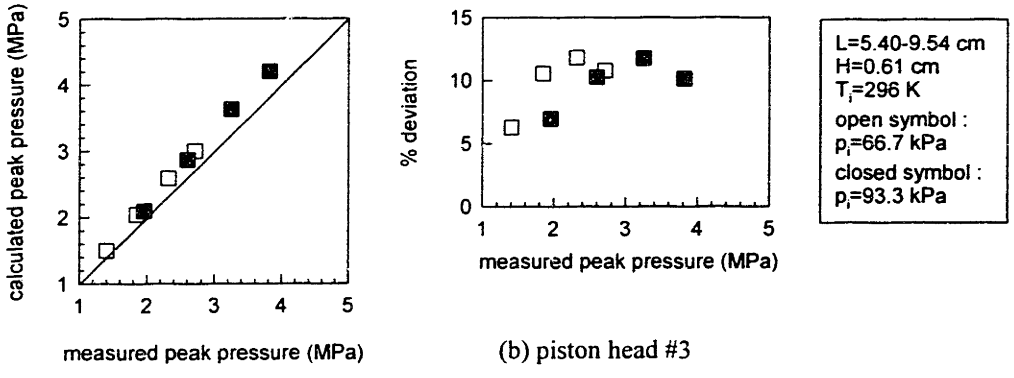

(b) piston head #3

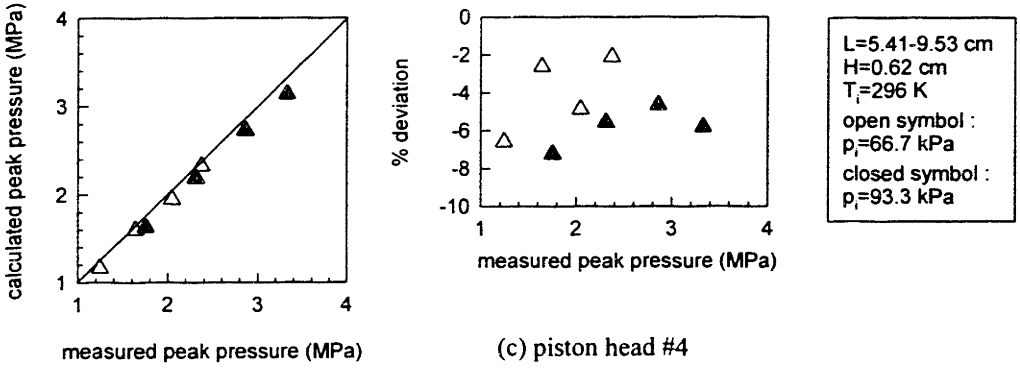

(c) piston head #4

Figure 4.3.3 Comparison between measured peak pressure and calculated peak pressure. Test gas : nitrogen. (a) piston head #1, (b) piston head #3, (c) piston head #4, (d) piston head #5 and (e) piston head #6.

(continued)

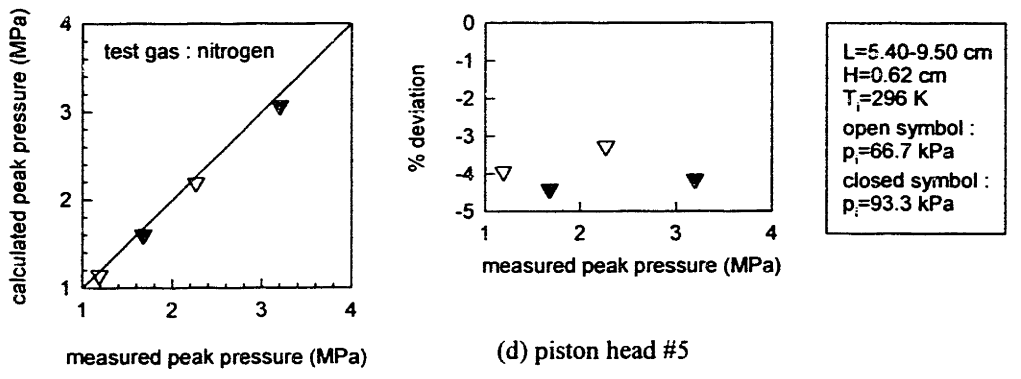

(d) piston head #5

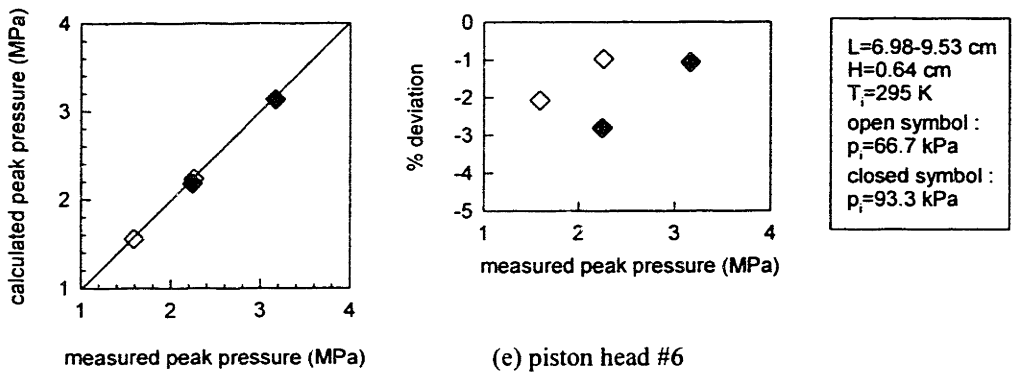

(e) piston head #6

Figure 4.3.3 *(continued)*.

to piston corner vortex) may explain the higher prediction of peak pressures than the measured values.

Piston head #4 has a larger crevice volume than piston head #1. As shown in Fig.2.5.3 (d) the increased crevice, having a relatively large surface to volume ratio, is located along the side wall of the piston head. The predicted peak pressure (Fig.4.3.3 (c)) is still less than the measured values, however, the difference is smaller than the case for piston head #1. Two explanations are possible: (i) from the shape and location of piston crevice, it is inferred that the entering gas can be cooled to the wall temperature faster than the case for piston head #1 and (ii)

since the piston head #1 does not have enough crevice volume to accommodate the scraped boundary layer, the increased crevice volume can reduce the generation of vigorous piston corner vortex.

When the wedge shaped piston crevice (#1) is enlarged (#5), predicted peak pressures are closer to the measured value as shown in Fig. 4.3.3 (d). This result implies that the piston crevice volume needs to be increased to a size greater than that of piston head #1 in order to accommodate the captured volume entering into piston crevice. As a result, the generation of piston corner vortex can be reduced. However, the entering gas may still be hotter than the wall temperature and additional work is necessary to understand its behavior if there exists temperature distribution within the captured gas.

Finally, the piston head with a crevice, designed to minimize the piston corner vortex and to *cool* the entering gas to the wall temperature quickly, was tested. As shown in Fig.4.3.3 (e), the model accurately predicts the measured values. This result validates design criteria (discussed in section 2.5.2) that piston corner vortex is successfully suppressed and the gas in the crevice reaches isothermal status quickly as it enters into a crevice. Comparison between the model and measurements also shows that heat loss by conduction is predominant, and convection heat loss is negligible in heat transfer characteristics, because the stroke variation (thus change of piston velocity) does not significantly alter the peak pressure prediction. Note that the deviation of predicted peak core temperatures due to pressure discrepancy is less than 5 K. Model verification by hydrogen autoignition measurements will be presented at the following chapter.

CHAPTER 5. HYDROGEN AUTOIGNITION

5.1. Introduction

The investigation of high pressure autoignition of combustible mixtures is of importance both as practical information in the design of combustion systems, as well as in providing fundamental measurements to verify and develop chemical kinetic models. The autoignition and explosion characteristics of hydrogen-oxygen mixtures at low pressures have been explored extensively in dilute mixtures in shock tubes: Schott & Kinsey (1958) investigated the range from 1080 to 1840 K at 0.1 MPa; Skinner & Ringrose (1965) extended the range of temperatures to 964-1075 K at 0.5 MPa, determining the change in activation energy as the state of the mixture crosses the extended second limit, and Cheng & Oppenheim (1984) obtained ignition delay times in the range of temperature from 800 to 2400 K and pressures from 0.1 to 0.3 MPa. The present measurements extend the range of pressures up to 4 MPa, where no measurements have yet been made.

Methods for investigation of autoignition and reaction characteristics of fuels at high pressures are typically rapid compression machines (RCMs), shock tubes and flow reactors. Of these, rapid compression machines can be extended to the highest pressures and concentrations. However, they typically have the disadvantage of difficult access for time-resolved diagnostics, which is typically limited to pressure measurements. Moreover, previous studies in RCMs have been hampered by the existence of temperature non-uniformities and fluid motion in the chamber resulting from the scraping of the thermal boundary layer by the piston, thus leading to

difficulties in separating the chemical kinetic from the transport effects. The objectives of this part of work were: (a) to develop a solution for the disturbance of the reacting zone in RCMs and (b) to test the predictions of the device using a well characterized reactant mixture, the hydrogen-oxygen system.

A new design of the piston crevice in the present study has been shown to minimize disturbances to the reacting zone, allowing more accurate predictions of the reacting temperatures to be made from the pressure trace as discussed in the previous chapters. Using the initial conditions, the displacement of the piston and gas molecular transport properties, a model for the state of the reactant zone is shown to accurately predict the observed pressures. Chemical kinetic model was also incorporated for predictions of the pressure history involving autoignition.

Hydrogen autoignition was measured at conditions (p=0.6-4 MPa, T=950-1050 K), which are above the second explosion limit defined as $[M]=2k_1/k_9$ (Lewis & Elbe 1987). The measured pressure records show a more gradual pressure increase in this regime than in the low pressure regime. The gradual pressure increases during the induction period indicated that the energy release during the induction time becomes significant at conditions over the second limit, as suggested by Kordylewski & Scott (1984) and Gray & Sherrington (1974). By comparing the measurements and model, a modified reaction rate constant for $H_2O_2+H=HO_2+H_2$ (R17) - one of the most important reactions for hydrogen oxidation at high pressure, and with the largest uncertainty - is suggested in this work as $k_{17}=2.3\times10^{13}\exp(-7950/RT)$. The modeled pressure history with the modified reaction rate agrees well with the measured values during the induction period over the range of conditions tested. In this chapter, the following is discussed :

(i) Hydrogen autoignition measurements.

(ii) Hydrogen oxidation mechanism, especially at pressures above the second explosion limit.

(iii) Identification of reactions important for chain branching and energy release.

(iv) Comparison between model and measured pressure records, and determination of a modified reaction rate.

5.2 Experiment

Experiments were performed using hydrogen-oxygen mixtures at peak pressures between 0.6 to 4 MPa, and peak temperatures between 950 and 1050 K, with induction times up to 45 ms (see Fig.2.2.2 for definitions). This range is well above the extended classical second explosion limit and at higher pressures than all previous measurements. The experimental conditions are summarized in Table 5.2.1. The RCM and its operation have been described in Chapter 2. The initial pressure and stroke were varied while other parameters such as the clearance height and gas mixture ratio were fixed. The single gas mixture was initially prepared as a ratio of $H_2/O_2/Ar$=2/1/5 and loaded into the combustion chamber.

The experimental conditions (peak pressure and temperature) and the measured induction times and conditions for which no autoignition was observed are shown in Fig. 5.2.1.

Table 5.2.1 Experimental parameters for hydrogen autoignition measurements.

L	7.47 - 9.98 cm
H	0.62 cm
piston head	#6 in Fig.2.5.3. (f)
p_i	0.015 - 0.12 MPa
T_i	298±2 K*
t_{cmp}	20 - 30 ms
Test gases	hydrogen, oxygen and argon

*Deviation of initial temperature designates run to run variation, not uncertainty of initial temperature.

Each experimental parameter and measured result are listed in Table A.4.4. At low temperatures, there is a gradual increase in the induction times as pressure decreases, whereas a sharp transition is observed as the pressure is decreased at high temperature through the no-ignition range. Such a transition has been previously observed at lower pressure by Schott & Kinsey (1958) and others (Kim *et al.* 1994, Cheng *et al* 1984), and is clearly illustrated in Fig. 5.2.2, where induction delay times (scaled to first order with oxygen concentrations) are plotted as a function of reciprocal temperature. Activation energies in the high temperature range are of the order of 20 kcal/mol, and at low pressures, rise to about 70 kcal/mol around 1100 K. Also shown in Fig. 5.2.2 are calculated induction times (dotted line in the figure) for *adiabatic*, constant volume autoignition of H_2-O_2 mixtures at different pressure. Although not directly comparable

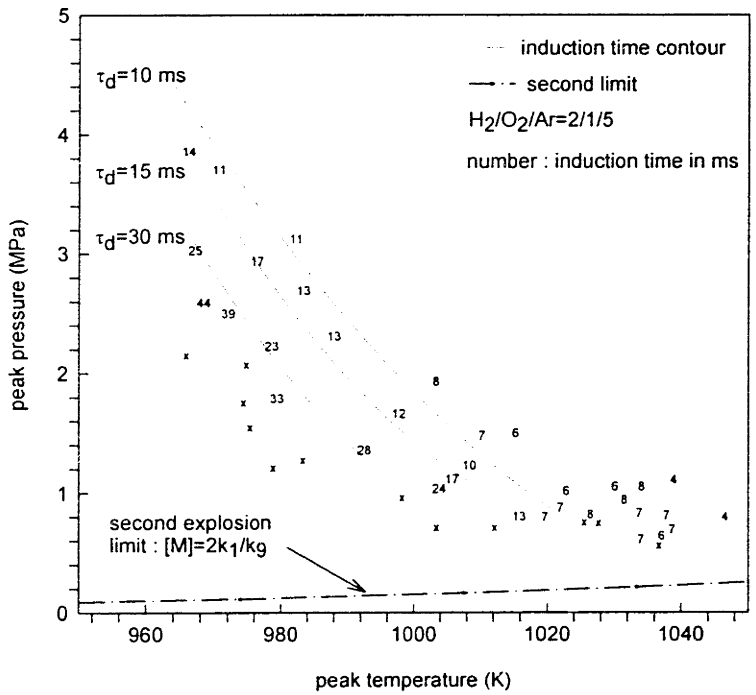

Figure 5.2.1 Range of measured induction times for hydrogen autoignition.
Pressure and temperature correspond to peak values. Numbers indicates induction time (in ms) at the corresponding (p_{peak}, T_{peak}). The x symbol represents conditions where autoignition was not observed. The second explosion limit was calculated using reaction rates by Kim *et al* (1994).

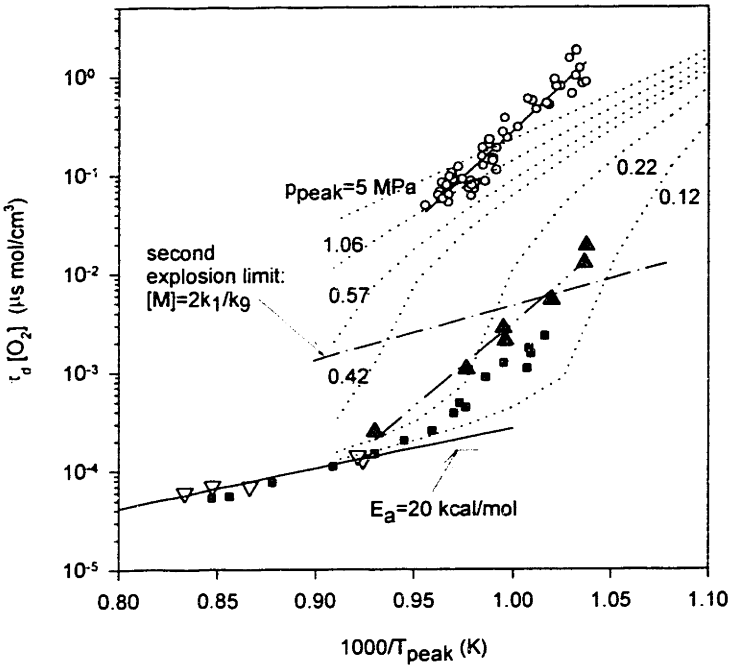

Figure 5.2.2. Arrhenius plot for hydrogen autoignition.
O This work : $H_2/O_2/Ar=2/1/5$, p_{peak}=0.6~4 MPa
▲ Skinner *et al.* (1965) : $H_2/O_2/Ar=8/2/90$, p=0.5 MPa
▽ Schott *et al.*(1958) : $H_2/O_2/Ar=1/2/97$, p=0.1 Mpa
■ Slack (1977) : $H_2/O_2/N_2=1/2/1.886$, p=0.2 MPa
— Cheng *et al.* (1984) : $H_2/O_2/Ar=2/1/27$, p=0.2 Mpa
····· adiabatic calculation : $H_2/O_2/Ar=2/1/5$, reaction rates by Kim *et al.* (1994).

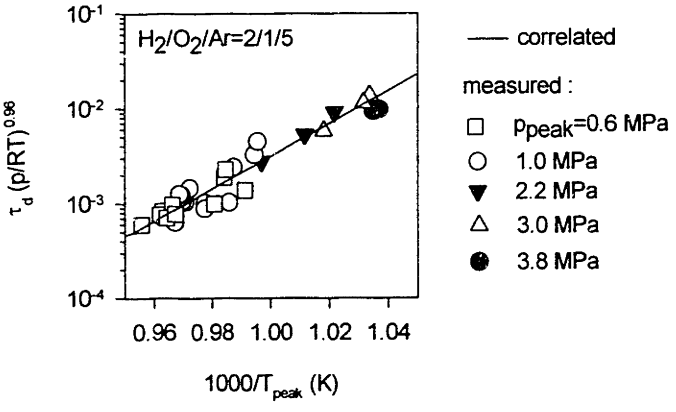

Figure 5.2.3 Comparison between measured and correlated data.
$\tau_d(p/RT)^{-0.96} = 3.72\times10^{-20}\exp(39{,}000/T)$. Units are in ms, MPa, K, R=8.314 J/mol K.

to the experimental data because of variable heat loss in each experiment, the model clearly shows two distinct limits at low and high concentrations, and a switch-over region with a high apparent activation energy.

Characteristics of measured pressure records were shown in Fig. 2.2.6 (a) and (b), showing the very rapid pressure rise. The measured induction times in the RCM can be well correlated using (Fig. 5.2.3)

$$\tau_d = 3.72\times10^{-20}(p/RT)^{-0.96}\exp(39{,}000/T) \qquad (5.2.1)$$

where units are sec, MPa, K and R=8.314 J/mol K.

5.3. Reaction rate mechanism

Autoignition modeling was performed using the thermodynamic model described in Chapter 3. Comparison with measured pressure records is discussed in the section 5.5.

5.3.1. Reaction rate constants

Table 5.3.1. Hydrogen oxidation reaction mechanism (Kim *et al.* 1994).

reactions	A[(a)]	n	E_a	UF[(b)]	T[(d)]	$\Delta h_{(1000K)}$
1. $H+O_2=O+OH$	1.91E+14	0	16.44	2	962-2,577	15.1
2. $O+H_2=H+OH$	5.13E+04	2.67	6.29	1.5	297-2,495	13.5
3. $OH+H_2=H+H_2O$	2.14E+08	1.51	3.43	1.5	250-2,581	-9.4
4. $O+H_2O=OH+OH$	2.95E+06	2.02	13.4	2.5	250-2,000	2.9
5. $H_2+M=H+H+M$[(c)]	4.57E+19	-1.4	104.38	3	600-2,000	112.9
$H_2+Ar=H+H+Ar$	5.89E18	-1.1	104.38			
6. $O+O+M=O_2+M$	6.17E+15	-0.5	0	1.3	2,000-10,000	-114.4
$O+O+AR=O_2+Ar$	1.91E13	0.0	-1.79			
7. $O+H+M=OH+M$	4.68E+18	-1	0	10		-99.3
8. $H+OH+M=H_2O+M$	2.24E+22	-2	0	2	1,000-3,000	-122.3
$H+OH+Ar=H_2O+Ar$	8.32E21	-2.0	0			
9. $H+O_2=HO_2$	4.47E13	0.0	0			
$H+O_2+M=HO_2+M$	6.17E+19	-1.42	0	3	200-2,000	-46.9
$H+O_2+Ar=HO_2+Ar$	1.51E15	0.0	-1			
10. $HO_2+H=H_2+O_2$	6.61E+13	0	2.13	2	298-773	-66.0
11. $HO_2+H=OH+OH$	1.70E+14	0	0.87	2	298-773	-37.4
12. $HO_2+O=OH+O_2$	1.74E+13	0	-0.4	1.2	200-400	-52.5
13. $HO_2+OH=H_2O+O_2$	1.91E+16	-1	0	2	254-1,050	-75.4
14. $HO_2+HO_2=H_2O_2+O_2$[(e)]	4.17E+14	0	11.98	3	650-850	-42.4
	1.29E+11	0	-1.629			
15. $H_2O_2+M=OH+OH+M$	1.20E+17	0	45.5	2	700-1,500	51.9
$H_2O_2=OH+OH$	2.95E16	0	48.4			
$H_2O_2+Ar=OH+OH+Ar$	1.91E16	0	43.0			
16. $H_2O_2+H=H_2O+OH$	1.00E+13	0	3.59	3	283-800	-70.4
17. $H_2O_2+H=H_2+HO_2$	4.79E+13	0	7.95	5	283-800	-23.6
18. $H_2O_2+O=OH+HO_2$	9.55E+06	2	3.97	3	250-800	-10.1
19. $H_2O_2+OH=H_2O+HO_2$[(e)]	1.00E+12	0	0	2	250-1,250	-33.1
	5.8E14	0	9.56			

(a) units are cm^3 mol s kcal K; $k=AT^n\exp(-E_a/RT)$.

(b) UF is an estimated uncertainty factor for the specified T range : $+\Delta k/k=UF-1$ and $-\Delta k/k=UF^{-1}-1$.

(c) Collision efficiency; $\varepsilon_{H2O}=12$, $\varepsilon_{H2}=2.5$, $\varepsilon_{Ar}=0.75$. All other species have efficiency equal to unity.

(d) T is the temperature range over which the rate constant parameters are evaluated.

(e) Reaction rate of 14 and 19 are the sums of two rate constant.

Table 5.3.2 Thermodynamic constants at 298.15 K Δh_f in kcal/mol, s, c_p in cal/mol.

species	Δh_f	s	c_p
H	52.07	27.37	4.97
O	59.52	38.66	5.23
OH	9.31	43.71	9.85
H_2	0	31.12	6.90
O_2	0	48.93	7.01
H_2O	-57.77	44.52	7.99
HO_2	3.50	54.59	8.37
H_2O_2	-32.51	55.61	10.41
Ar	0	36.96	4.97

The chemical kinetic mechanism, rates and thermodynamic data used in the simulations was extracted from Kim *et al.* (1994), since that recent work has been tested against high pressure data up to 1 MPa. The mechanism and rates are reproduced in Table 5.3.1, where 10 species and 19 reactions are used. Table 5.3.2 lists the standard enthalpies of formation, $\Delta h^o_{f,298.15K}$, entropies and specific heats for species considered in the mechanism. All of the data are from Kee *et al.* (1987) with the exception of the heat of formation of HO_2 ($\Delta h^o_{f,298.15K}$ =3.5±0.5

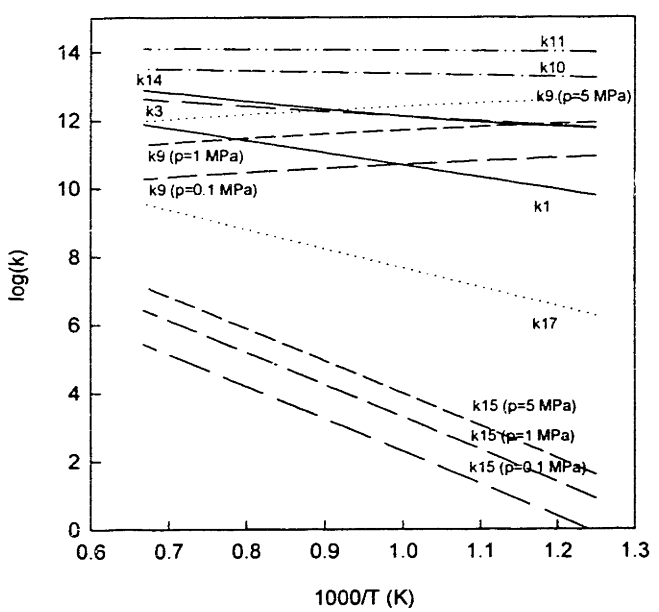

Figure 5.3.1 A comparison of important reaction rate constants consisting of hydrogen oxidation mechanism. Their relative importance is discussed in section 5.4.

kcal/mol by Shum *et al.* 1987, instead of $\Delta h^{o}_{f,298.15K}$=2.5 kcal/mol by Kee *et al.* 1987). The polynomial coefficients for all species, except HO_2, are from Kee *et al.* (1987). The polynomial coefficients for HO_2 by Ritter & Bozzelli (1987) were obtained from Hochgreb (1991) (Refer to Table A.4.1 for listed polynomial coefficients). Figure 5.3.1 shows reaction rate constants of important reactions for hydrogen oxidation. The relative importance among reactions is discussed in section 5.4. The pressure history was calculated using a modified CHEMKIN driver (Kee *et al.* 1990) combined with the thermodynamic model described in chapter 3. The structure of programs is shown in Fig. A.4.2.1.

Discussions regarding the heat of formation (used to evaluate the reverse rate constant, since the rate constants are specified for one direction only.) and the third body efficiencies (used for the dissociation/recombination reactions) follows.

5.3.2 Heat of formation

The enthalpy diagram shown in Fig. 5.3.2 shows the thermodynamic energies associated with the reactants, the products, and the transition state connecting the two. The energy difference between the reactants and products is the difference in their heats of formation and is given by

$$\Delta H^{\circ}_{reaction} = \Delta H^{\circ}_{f(products)} - \Delta H^{\circ}_{f(reactants)} \qquad (5.3.1)$$

A reaction which is highly *endothermic,* that is, which has a large positive $\Delta H^{\circ}_{reaction}$, is not likely to proceed spontaneously except at very high temperatures. A highly *exothermic* reaction, however, may do so unless the activation energy required to reach the transition state is very high; in that case, the reaction will be slow at other than very high temperatures. The calculation of reaction exothermicities is often a helpful guide in assessing the relative importance of individual reactions in a complex mechanism.

An important relationship is established by the difference between forward and reverse activation energies for a given reaction. Clearly,

$$E_{a(forward)} - E_{a(reverse)} = \Delta H^{\circ}_{reaction} \qquad (5.3.2)$$

Thus, exothermic reactions have a larger activation energy for the reverse reaction, while the opposite is true for endothermic reactions (Steinfeld 1989).

According to basic thermodynamic principles, several thermodynamic properties and constants are available from enthalpy data. Of those, the equilibrium constants are calculated and the following relationship holds for any reacting system :

$$K_c = \frac{k_f}{k_b} \qquad (5.3.3)$$

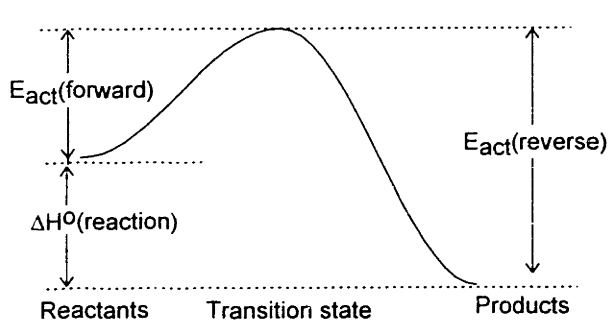

Figure 5.3.2. Enthalpy diagram for a chemical reaction.

where K_c is the equilibrium constants based on concentrations, k_f is forward rate constants and k_b is for backward (or reverse). Once the forward(or reverse) rate constants are given, the reverse(or forward) rate constants are calculated based on the relation (5.3.3). The equilibrium constant at a reference pressure can be denoted as follows (refer to Kee *et al. 1990* for notations):

$$K_c = K_p \left(\frac{p_{atm}}{RT} \right)^{\sum_{k=1}^{K} \nu_k} \tag{5.3.4}$$

where p_{atm} denotes a pressure of 1 atm. The equilibrium constants K_p are obtained from the relationship

$$K_p = \exp\left(-\frac{\Delta G^o}{RT} \right) = \exp\left(\frac{\Delta S^o}{R} - \frac{\Delta H^o}{RT} \right) \tag{5.3.5}$$

The Δ refers to the change that occurs in passing completely from reactants to products in the given reaction, and superscript o denotes the standard state (273K, 1atm). More specifically,

$$\frac{\Delta S^o}{R} = \sum_{k=1}^{K} \nu_k \frac{S_k^o}{R} \tag{5.3.6}$$

$$\frac{\Delta H^o}{RT} = \sum_{k=1}^{K} \nu_k \frac{H_k^o}{RT} \tag{5.3.7}$$

where K is the total number of species in the given reaction.

For this study, the reverse rate constants for all reactions are calculated using the thermochemical data by Kee *et al.* 1987 except data for HO_2 (Shum & Benson 1987). A study by Norton & Dryer (1989) shows that the most significant change in the heat of formation in hydrogen oxidation is for the species HO_2. Table 5.3.3 lists a comparison between several evaluations. This change has a dramatic effect as the chemistry approaches equilibrium. For example, while the forward rate constant of the important reaction $H_2O_2+H=HO_2+H_2$ (R17) is

Table 5.3.3. A comparison of estimated heat of formation for HO_2.

He of formation at 298 K (kcal/mol)	reference
2.50	Kee *et al.* 1987
3.00	Hills *et al.* 1984
3.50	Shum *et al.* 1987
5.00	Westbrook *et al.* 1979

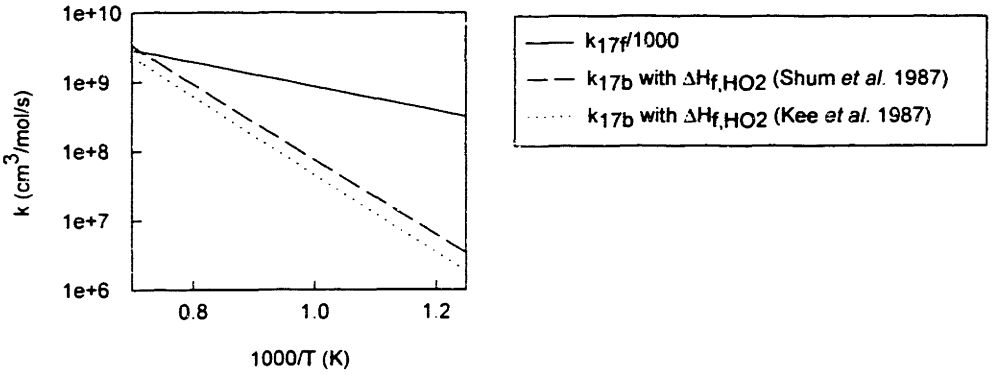

Figure 5.3.3. Calculated reverse rate constants for $H_2O_2+H = HO_2+H_2$ (R17). k_{17f} is from Tsang *et al.* (1986). k_{17b} was calculated for each heat of formation for HO_2.

identical in both mechanisms, its reverse rate constant varies by about 60 % (at 1000K) depending on the heat of formation for HO_2. Figure 5.3.3 shows this difference in the reverse rate constants with the same forward rate constant. The calculation was performed using CHEMKIN subroutines as denoted in Eq.(5.3.3-7).

In hydrogen oxidation, which is the sub mechanism for other complex fuels oxidation, several reactions include HO_2 species that are important at high pressure oxidation as well. Thus, a change in the heat of formation for HO_2 can significantly affect the overall induction time as shown in Fig. 5.3.4. A comparison was made for different heats of formation for HO_2 while

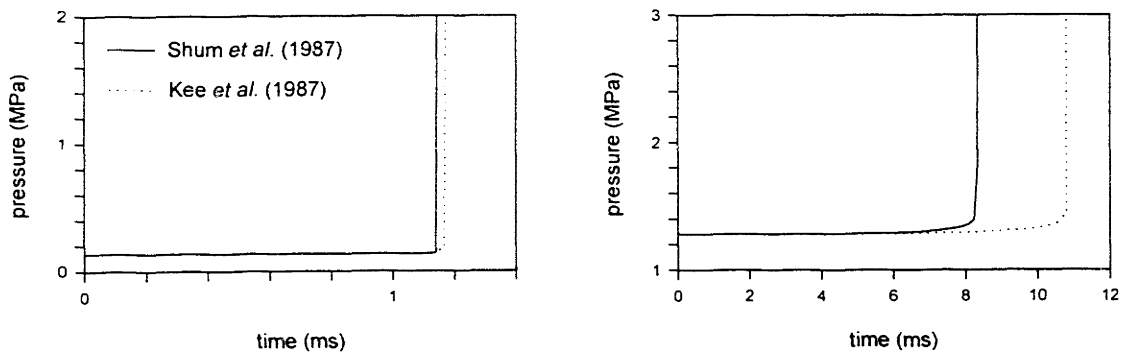

(a) p_i=0.13 MPa, T_i=960 K

(b) p_i=1.3 MPa, T_i=960 K

Figure 5.3.4. Induction time comparison depending on the heat of formation for HO_2. Reaction rates (Kim *et al.* 1994) are same for both cases except $\Delta H_{f,HO2}$. Calculation was made at adiabatic, constant volume condition with (a) p_i=0.13 MPa and T_i=960 K, (b) p_i=1.3 MPa and T_i=960 K.

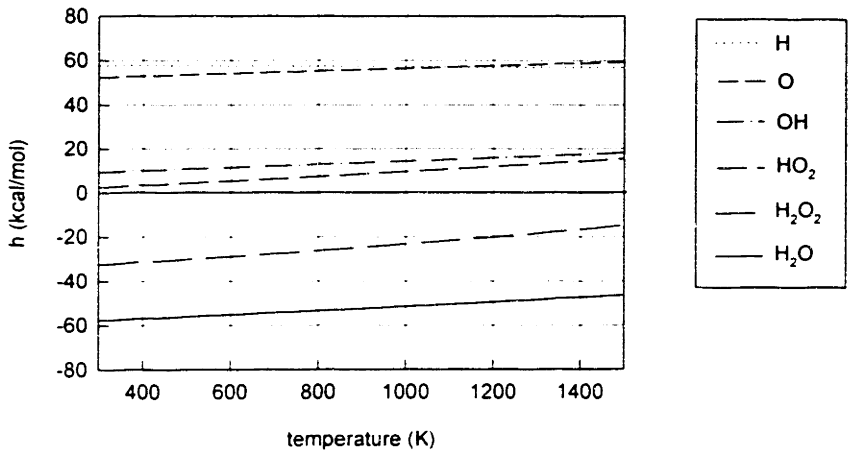

Figure 5.3.5. Enthalpy for each species and heat of formation at T=298.15 K. Using data by Kee *et al.* (1987) except HO_2, which is by Shum *et al.* (1987).

other conditions are kept constant. The result shows that the larger reverse rate constants for R17 resulting from larger heats of formation for HO_2 (Table 5.3.2) accelerate the reaction at high pressure (Fig. 5.3.4 (a): above the second explosion limit) whereas at low pressure (Fig.5.3.4 (b): below second explosion limit) the effect of the difference in $\Delta H^o_{f,HO2}$ on the overall induction time is negligible (the mechanism leading to this will be discussed in the following chapters in detail). Thus, the accurate evaluation of $\Delta H^o_{f,HO2}$ is more critical for hydrogen oxidation at high pressure than at low pressure oxidation. Figure 5.3.5 shows calculated total enthalpies for species considered in the hydrogen oxidation model.

5.3.3. Third body efficiency

A simple example of an important three-body recombination reaction is

$$H+O_2+M=HO_2+M \qquad (R9)$$

where M refers to any available third body species, required to conserve both momentum and energy in this type of reaction. In this case, the third body acts to remove the excess energy from the recombining reactants, thereby stabilizing the molecular products (Westbrook 1984, Steinfeld 1989). Third body reactions are very important at high pressures, where collisions are frequent. Though all of the important mechanistic steps and rate expressions for the H_2-O_2 mechanism are now relatively well known, studies point out that important work still needs to be done, particularly in determining *chaperon efficiencies* for different third bodies in reaction R9. As a general rule, the efficiency of each species which is present in quantities larger than about 5% should be considered. Water molecules are particularly good chaperons, with efficiency which can be 10-50 times larger than those of Ar. The chaperon efficiency increases with the number of degrees of freedom available to share collision energy. Atomic species like argon or helium are comparatively inefficient, followed by diatomic species such as N_2 and O_2, followed in turn by polyatomic species (Westbrook 1984).

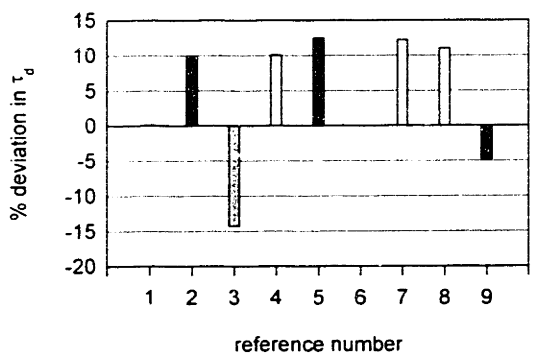

Figure 5.3.6 A comparison of % deviation in induction time according to different sets of third body collision efficiencies. Refer to Table 5.3.3 for details of each reference number. Test gas : $H_2/O_2/Ar=2/1/5$ at $p_{peak}=1.3$ MPa, $T_{peak}=960$ K.

Table 5.3.4. Comparison of third body collision efficiencies.
Values in parentheses were assumed when not assigned by each study (from $\varepsilon_{N2}/\varepsilon_{Ar}$=1.33. All other species have efficiency equal to unity). $[M]=\Sigma\varepsilon_i[C_i]$, where ε_i is ith species collision efficiency (or chaperon efficiency), C_i is concentration of ith species. Reference τ_d was calculated in adiabatic, constant volume condition using reaction rates (kim *et al.* 1994) at p_i=1.3 MPa, T_i=960 K.

ref. #	H_2O	H_2	O_2	N_2	Ar	H	O	OH	HO_2	remarks
1	6	2.5	1	(1)	(0.75)	20	1	1	1	1967,69,71(a)
2	25	1	1	(1)	(0.75)	1	1	1	1	Gutman 1967
3	1	1	10	(1)	(0.75)	1	30	1	1	Watt 1969
4	20	1	1	(1)	(0.75)	1	1	1	1	Homer 1970
5	6.5	1	0.35	0.44	(0.33)	1	1	1	1	Dixon-L. 1975
6	16	2.5	1	1	(0.75)	1	1	1	1	Norton 1989
7	6.4	1	0.4	(1)	(0.75)	(1)	(1)	(1)	(1)	Baulch 1988
8	6.5	100	0.35	0.5	(0.375)	(1)	(1)	(1)	(1)	Mass 1988
9	16	3.33	1		1	1	1	1	1	Yetter 1991
ref. τ_d	12	2.5	1	1	0.75	1	1	1	1	Kim 1994

(a) Collected from H_2 and H: Jacobs, T.A. *et al., J.Chem.Phys.*,**47**,54, 1967; for H_2O:Getzinger, R.W. *et al.,Combstion and Flame*, **13**, 271, 1969 and Gay, A. *et al., Procs. Eighth Int'l Shock Tube Sym.*, **39**,13, 1971

Table 5.3.4 lists the collision efficiencies and Fig. 5.3.6 shows their effect on the calculated induction time compared to the reference case (Kim 1994). The reference induction time was calculated at adiabatic, constant volume conditions at 1.3 MPa (initial pressure) and 960 K (initial temperature), and the calculated induction time was 8.35 ms. Although the collision efficiency for H_2O is much larger than other species, the wide changes in this efficiency does not affect the overall induction time significantly. This is because the concentrations of H_2O increase abruptly at the final stage of an induction period due to nature of the autoignition characteristics in a rapid compression machine at ranges covered by this study. From the recent version of the reaction rates (Kim *et al.* 1994), the following relation for third body efficiencies were used throughout this study:

$$[M]=1.0[N_2]+0.75[Ar]+2.5[H_2]+12.0[H_2O]+1[\text{All other species}] \quad (5.3.8)$$

Further, it is assumed that third body efficiencies, although different among species, are the same for each recombination/dissociation reaction. Studies (Warnatz *et al.* 1985) showed that this

assumption failed in reactions where the third body is chemically interacting with the collision complex, *e.g.*, $H+H+H_2=2H_2$. Finally the feature not included in the model is the dependency of chaperon efficiencies on temperature, although some reactions have been observed to exhibit a temperature dependence (Hsu *et al.* 1989).

5.4. Hydrogen oxidation mechanism

There are two main regions in the pressure-temperature space regarding the behavior of hydrogen oxidation. At relatively low pressures (below the extended second limit) the reaction is controlled primarily by the kinetics of the different reactions : energy release rates are very small and conditions are isothermal or near-isothermal. At high pressures (above the extended second limit) energy release is significant and thermal explosion is observed. Yetter *et al.*(1991) described these two regions as *strong* (or *sharp*) and *weak* (or *mild*) ignition separated by a region related to the extended classical second limit. The reaction changes from a fully branched mechanism (*strong* ignition) to a straight-chain mechanism with rare branching (*weak* ignition).

5.4.1. Chain branching and thermal explosion

The theory of thermal ignition is based upon the concept that when the rate of thermal energy release is greater than the rate of thermal energy loss, an explosive condition exists. When the contrary condition exists, thermal explosion is impossible, When the two rates are equal, critical conditions for ignition (explosion) are specified. Essentially, the same type of concept holds for the chain branching explosion. When the rate of chain branching becomes greater than the rate of chain termination, there is an explosive condition. Thus, when the external effects of heat loss or chain termination are considered, there is a greater deal of commonality between chain and thermal explosions. While the terms thermal and chain-branching explosion have been introduced separately, in many situations the self-accelerations in temperature and radicals occur simultaneously and the two phenomena must be combined (Glassman 1987). Thus, chain-branching can be understood as an explosion without significant heat release during

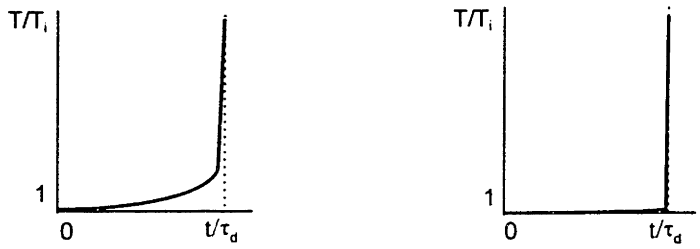

thermal explosion explosion by chain branching

Figure 5.4.1 Temperature-time diagrams for thermal and chain branching explosion.

an induction time, while the thermal explosion as an explosion due to exothermic reactions releasing apparent heat (or pressure rise at a confined volume). Figure 5.4.1 shows diagrams for a thermal and a chain branching explosion.

This distinct behavior in hydrogen autoignition is shown in Figure 5.4.2, where pressure, temperature and concentration profiles are shown as a function of time for three different initial pressures at 1000 K initial temperature (see also Fig. 5.4.3 (a) for pressure and temperature locations), under adiabatic, constant volume conditions. Below the extended second limit (Fig. 5.4.2 (a)), temperature and pressure remain essentially constant throughout the induction period, indicating that energy release is not significant. At the other extreme (Fig. 5.4.2. (c)) above the second limit, both pressure and temperature rise due to early energy release. The concentration profiles reflect the corresponding characteristics depending on the initial pressure. Note that the increase in the concentrations of HO_2 and H_2O_2 *radical* is more pronounced at high pressure (c) than at low pressure (a).

In order to understand the origin of these different characteristics, the comparison can be made between an *isothermal* and an *adiabatic* calculation in pressure and temperature space: In the isothermal case (dotted line in Fig. 5.4.3), both pressure and temperature are kept constant. The induction time is here defined at the point where the H_2O concentration peaks. In the adiabatic case, the reaction evolves from the initial temperature and pressure without heat loss at constant volume (solid line in Fig.5.4.3),

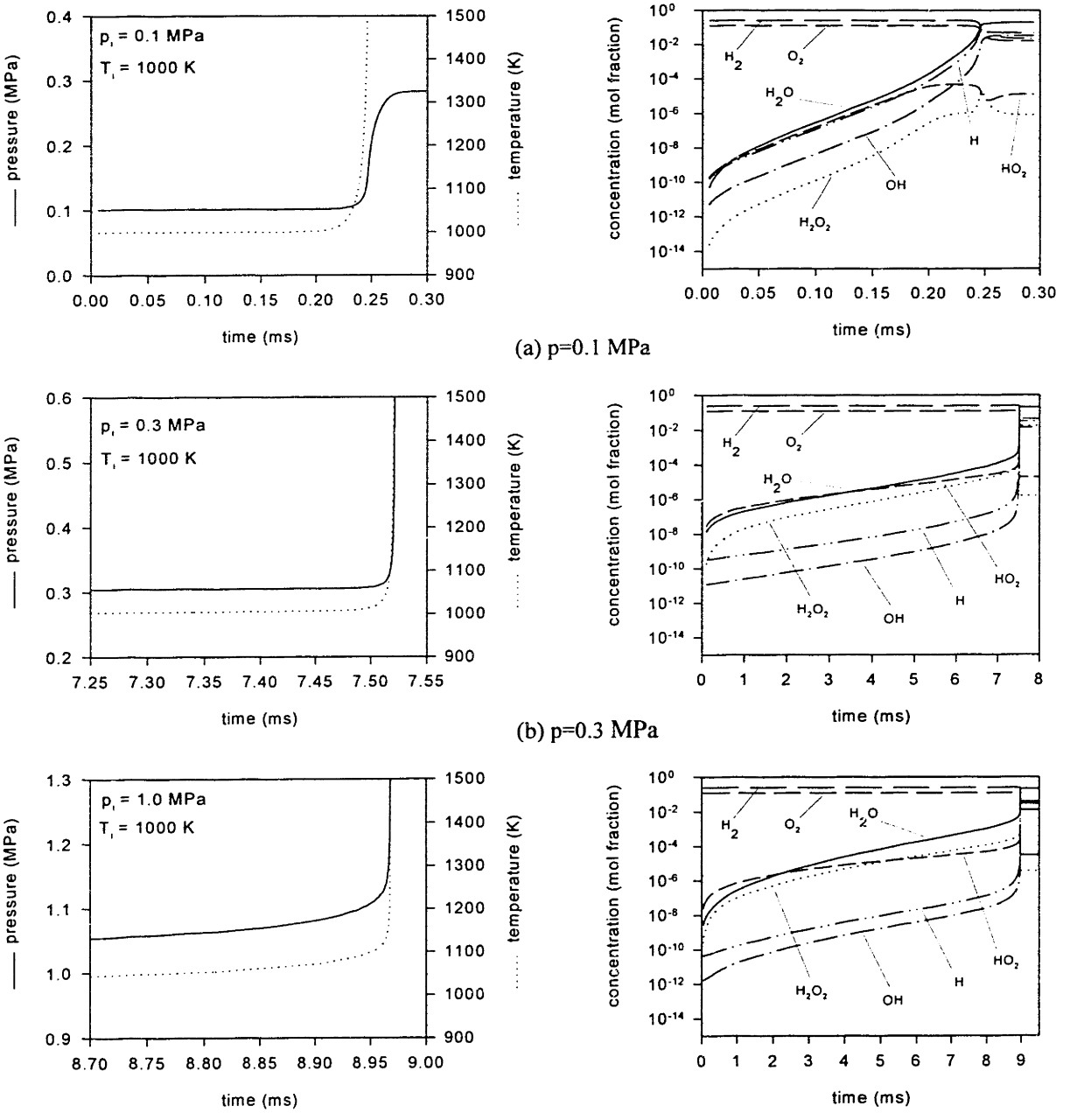

Figure 5.4.2. Pressure, temperature and species concentration as a function of initial pressure. Adiabatic calculation was performed with reaction rates by Kim *et al.* (1994). T_i = 1000 K (a) p_i = 0.1 MPa, (b) p_i = 0.3 MPa and (c) p_i = 1.0 MPa. Note that pressure and time spans are same for pressure profiles for comparison of energy release before autoignition.

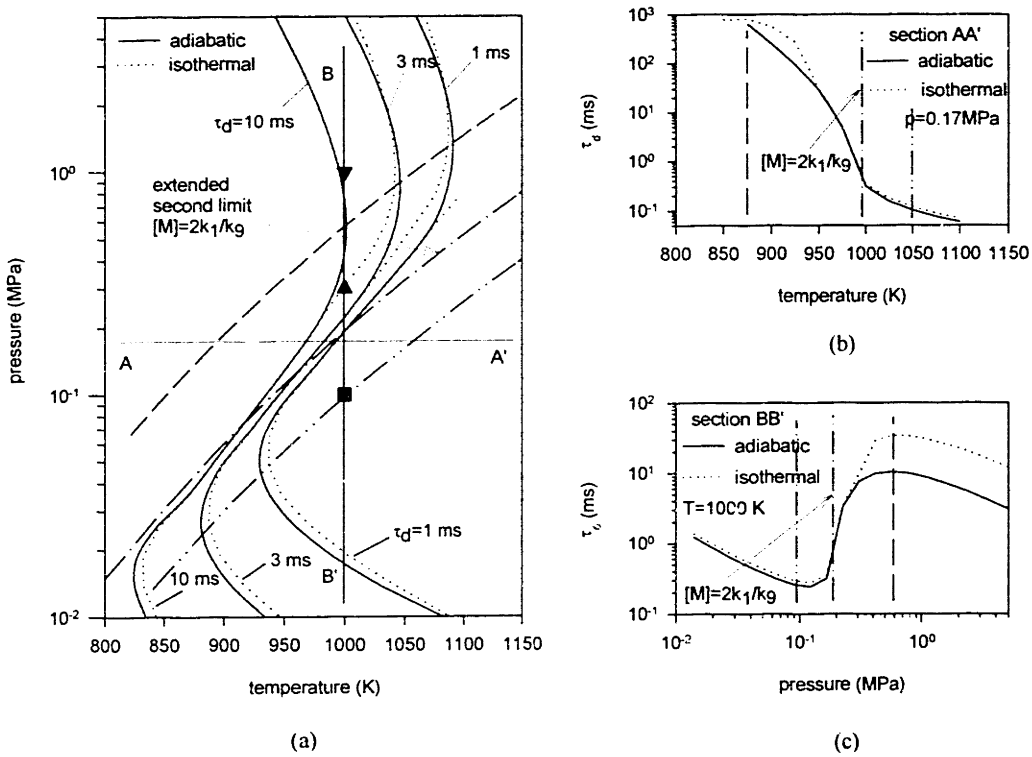

Figure 5.4.3. Induction time contour plots for hydrogen oxidation as a function of pressure and temperature. Symbols ■, ▲ and ▼ represent pressure and temperature conditions where calculations in Fig. 5.4.2 were made (respectively (a), (b) and (c)).

and the induction time is calculated at the point where the rapid pressure rise occurs (it is also where the H_2O concentration peaks). Clearly at low pressures up to the extended second explosion limit, both isothermal and adiabatic calculations show the same induction time behavior. However, at high pressures, the early energy release due to reaction plays a much more important role, as shown by the fact that the induction time in the isothermal calculation is significantly longer than that in the adiabatic case (Fig. 5.4.3 (c)). This comparison between isothermal and adiabatic calculations shows that as pressure increases and temperature decreases, which is toward above the second limit, energy release becomes significant during the induction time. Kordylewski *et al.* (1984) investigated the influence of self-heating in the second and third explosion limits (Lewis *et al.* 1987) in the hydrogen oxidation

system. They proposed that as the reactant pressure is increased toward the third limit, self-heating becomes important and influences the reaction rate mainly via the kinetics of hydrogen peroxide decomposition. The following analysis elucidates the pathways through which energy is released, as well as the reactions to which the induction time is most sensitive.

5.4.2 Reaction pathway of hydrogen oxidation

Studies show that at very low pressures the overall reaction is dominated by reactions R1, R2 and R3 (Lewis *et al.* 1987, Westbrook *et al.* 1984). (Refer to Table 5.3.1 for reaction numbers). As the pressure increases, reaction R9 becomes important and produces HO_2, which is a much less active radical than O, H and OH.

$H+O_2=O+OH$ (R1)

$O+H_2=H+OH$ (R2)

$OH+H_2=H+H_2O$ (R3)

$H+O_2+M=HO_2+M$ (R9)

Figure 5.4.4 shows the reaction flux for HO_2 and H_2O_2 as pressure changes from 0.1 MPa to 1.0 MPa while the temperature is kept constant at 1000 K. Reactions R9, R14, R15 and R17b (backward reaction) are the most important reactions associated with consumption/production of HO_2 and H_2O_2 at high pressure. Figure 5.4.5 shows the sensitivity gradients for H_2O and H_2O_2 at different pressure, indicating reactions important for completion of the overall reaction, and thus sensitive to induction time. Case (a) is for the lower pressure (p=0.1 MPa, T=1000 K), which is below the extended second limit. In this low pressure range, the most important reaction constants are R1, R2, R3, R9, R10 and R11.

$HO_2+H=H_2+O_2$ (R10)

$HO_2+H=OH+OH$ (R11)

In this range the ratio of R1 to R9 controls the overall reaction rate (Lewis *et al.* 1987). Although at low pressure reaction R9 terminates the chain, under high pressure conditions it becomes part of a chain propagating path (involving HO_2, H_2O_2) consisting essentially of reaction R9, R14

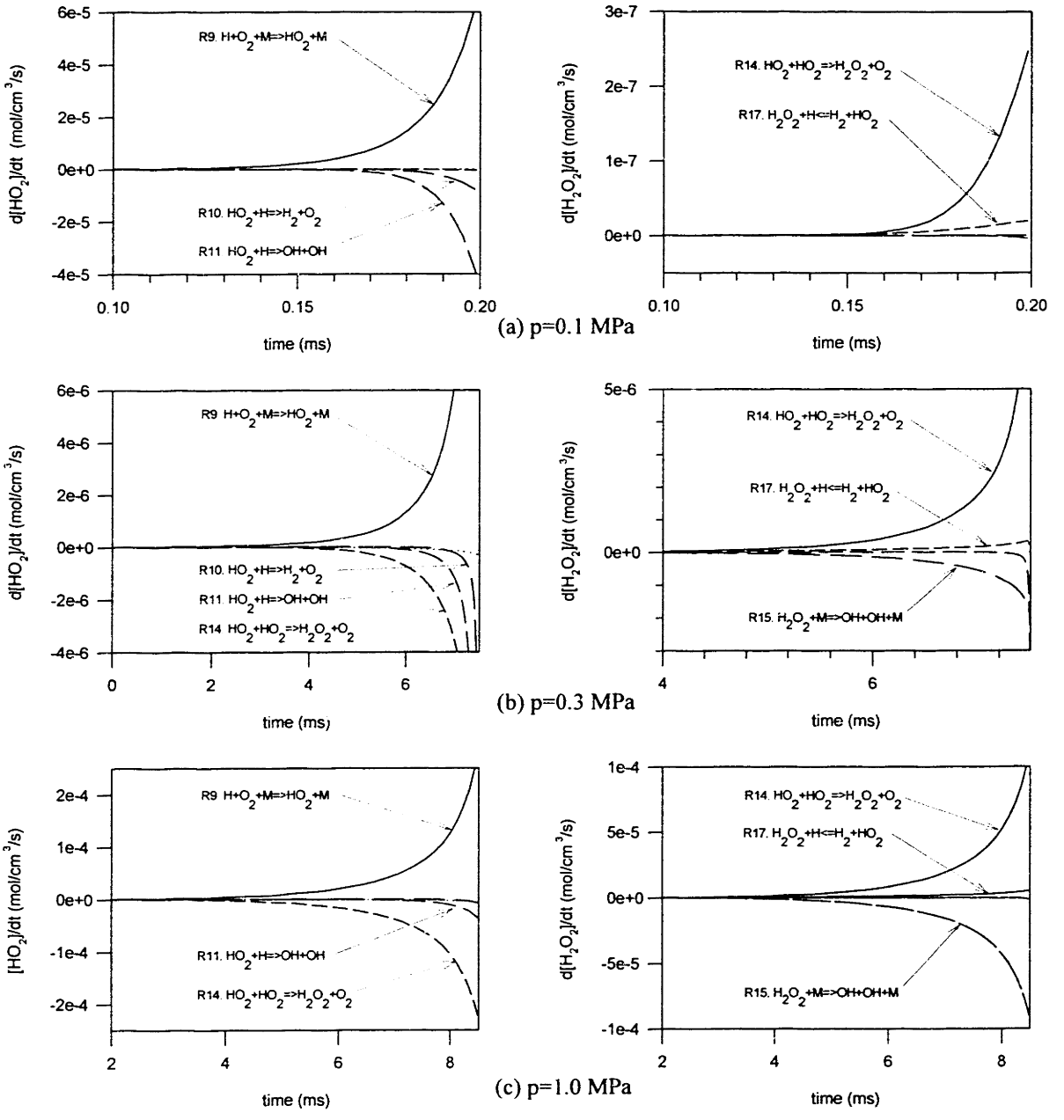

Figure 5.4.4. Flux analysis for HO_2 and H_2O_2 as pressure changes (a) 0.1 MPa, (b) 0.3 MPa and (c) 1.0 MPa. T_i=1000 K for all cases. Note that each pressure and temperature condition is same as in Fig.5.4.2 respectively.

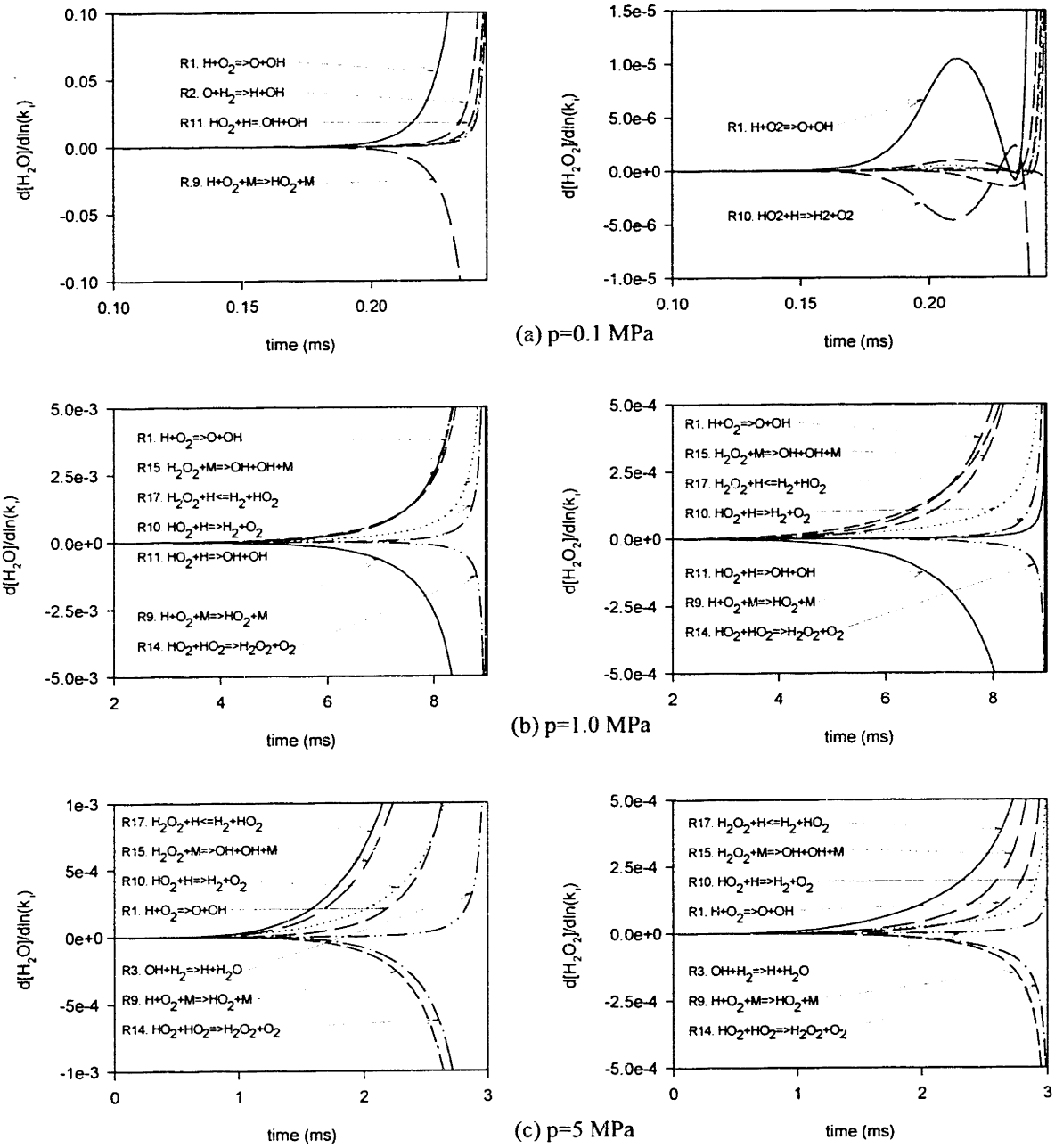

Figure 5.4.5. Sensitivity analysis for H_2O and H_2O_2 as pressure changes. (a) p=0.1 MPa, (b) 1.0 MPa and (c) 5 MPa. T_i=1000 K for all cases. Sensitivity gradient is defined as $S_{ij} = k_j[\partial C_i / \partial k_j] = \partial C_i / \partial[\ln k_j]$, where C_i is the molar concentration for species i, and k_j is the pre-exponential factor for jth reaction.

and R15 or reaction R9, R17b, and R15. The role of H_2O_2 in the overall induction time, τ_d, is not important in this pressure and temperature range indicated by the sensitivity analysis of τ_d (Fig. 5.4.6) to reactions associated with H_2O_2 production and consumption. Reactions R14, R15 and R17b are mostly associated with H_2O_2 production and consumption at pressures above the extended second limit. As the pressure increases up to the extended second limit, reactions R14, R15 and R17b become important as shown in Fig. 5.4.5 (b), (c). Sensitivity analysis to induction time (Fig. 5.4.6) also shows that these reactions are important at high pressure. Thus the following three reactions plus the above six reactions can be grouped as the most important reactions over the whole pressure range.

$HO_2+HO_2=H_2O_2+O_2$ (R14)

$H_2O_2+M=OH+OH+M$ (R15)

$HO_2+H_2=H_2O_2+H$ (R17b)

The main reaction pathways dominant at each extreme pressure region, as determined from reaction flux and sensitivity analyses, are shown in Fig. 5.4.7.

Although both reactions R14 and R17 contribute to produce the intermediate radical H_2O_2, an increase in reaction rate constant for R17 accelerates the overall reaction, whereas an increase in R14 retards the overall reaction. This can be interpreted by the pathway leading to produce the OH radical at this high pressure: The main branching pathway for production of OH radicals is the decomposition of H_2O_2. The latter is produced by the recombination of HO_2 molecules (R14) or abstraction of H from H_2 by HO_2 (R17b). These two paths are competing for HO_2. When R14 is increased, the overall rate of production of H_2O_2 is decreased (since it is in parallel with R17b, and consumed two HO_2) and this slows down the overall reaction.

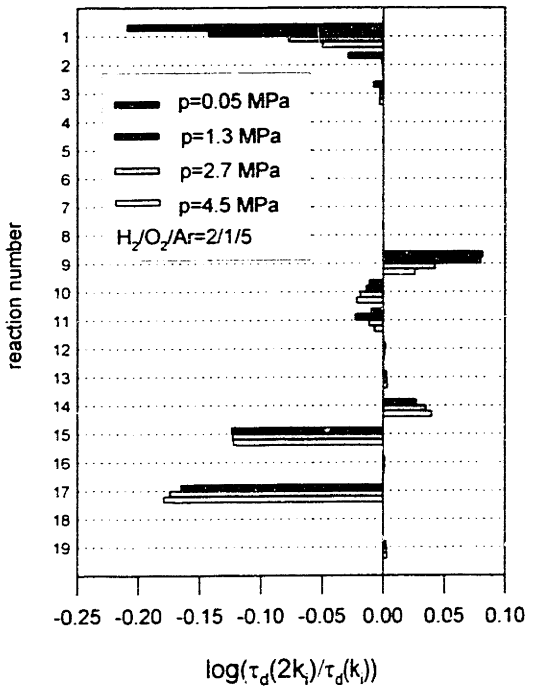

Figure 5.4.6. Sensitivity of τ_d to different reaction constants for hydrogen oxidation. $\tau_d(2k_i)$ refers to induction time after an increase in the rate coefficient of the reaction considered and its reverse reaction by a factor of two. T_i=1000 K

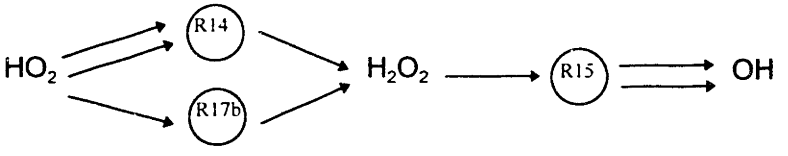

(5.4.1)

Reactions R17b through R15 consecutively consume HO_2 (which is mainly produced by reaction R9) and produce two OH radicals, which is the main radical consuming H_2 at high pressures, as the reaction pathway in Fig. 5.4.7 shows. Therefore, an increase of R17b results in faster overall reaction as shown by the sensitivity analysis in Fig.5.4.6. Figure 5.4.8 shows the comparison of calculated induction time when the involved reactions are reduced, clearly showing the importance of reaction R14, R15 and R17 at high pressures (above the second explosion limit). Finally, one needs to consider the role of highly exothermic reactions during the induction time, which is discussed at the following section.

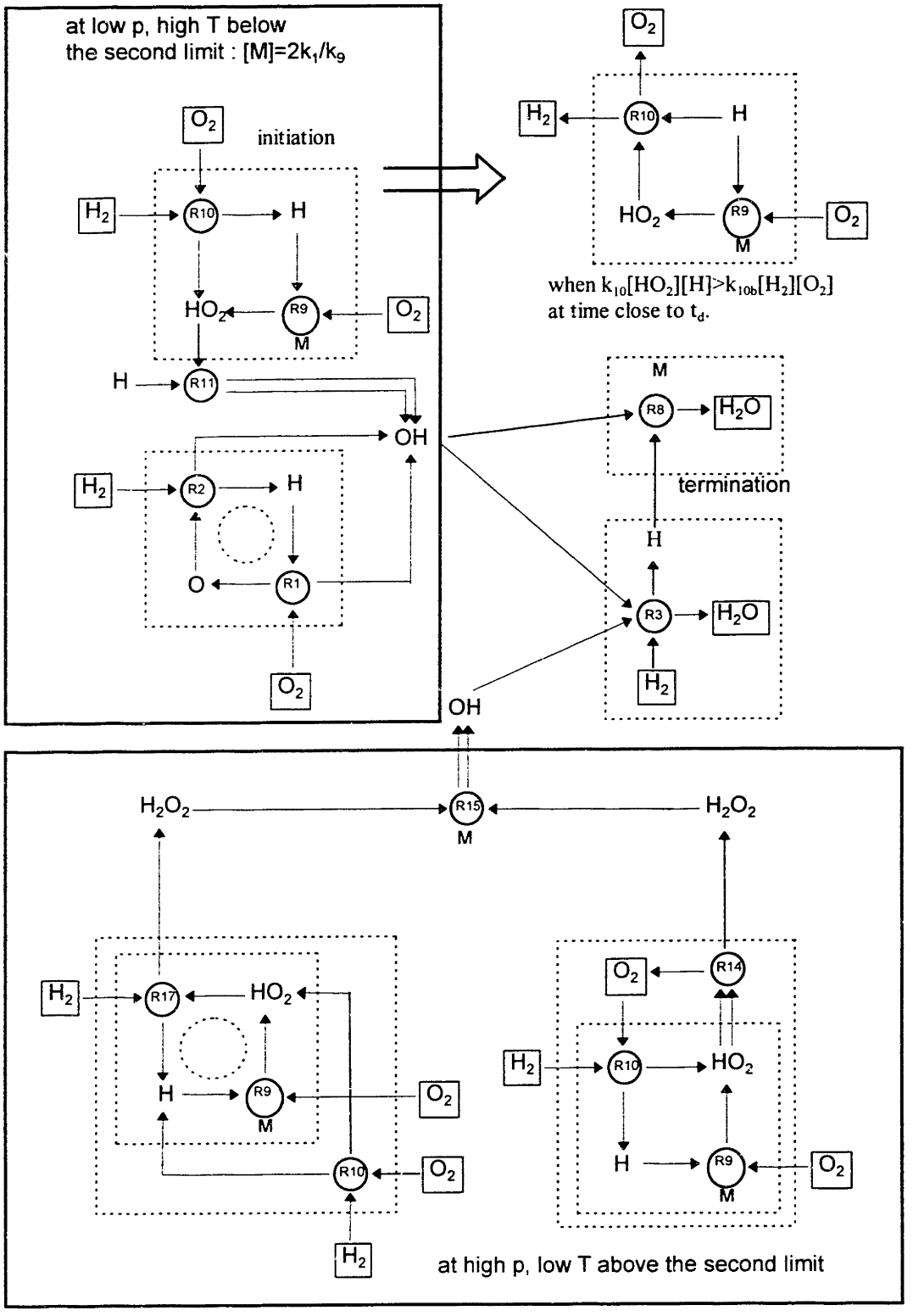

Figure 5.4.7. Main reaction paths for hydrogen oxidation with 9 reactions. Dominant reactions are separated by the second limit criterion ([M]=$2k_1/k_9$). Refer to Table 5.3.1 for reaction numbers.

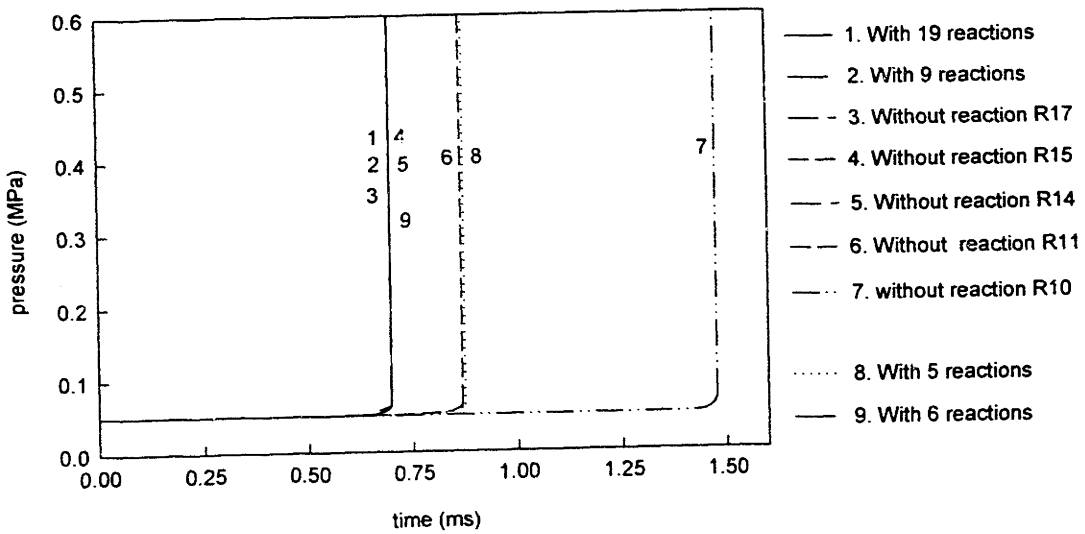

(a) p_i=0.05 MPa, T_i=950 K

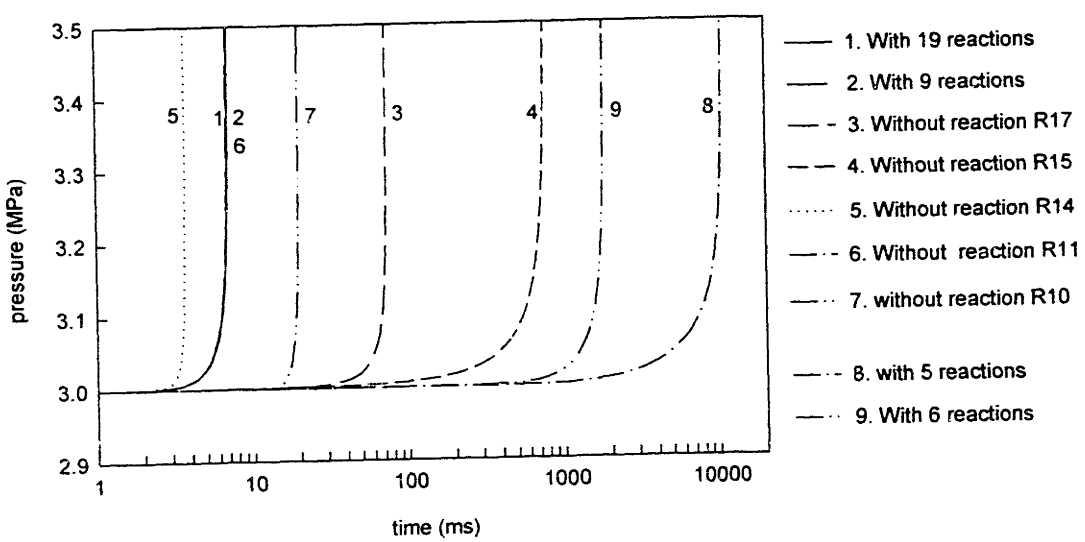

(b) p_i=3.0 MPa, T_i=950 K

Figure 5.4.8 Comparison of induction time when involved reactions are reduced. Nineteen reactions consists full mechanism. Five reaction sets consist of R1, R2, R3, R9 and R10. Six reaction sets is added with R11. Nine reaction sets include R14, R15 and R17 in addition. Constant volume and adiabatic conditions were used.

5.4.3 Exothermic reactions at high pressure pathway

Slow competing reactions (the following two paths) can become important if they are very *exothermic*. They can significantly affect the temperature of an (adiabatic) system and thus move the system into an explosive regime (Glassman 1987).

Path I	$H+O_2+M \rightarrow HO_2+M$	$\Delta h_{1000K}=$	-47 (kcal/mol)	(R9)
	$HO_2+H \rightarrow OH+OH$		-37	(R11)
	$2H+O_2 \rightarrow OH+OH$		-84	
Path II	$2H+2O_2+M \rightarrow 2HO_2+M$		-94	(R9)
	$HO_2+HO_2 \rightarrow H_2O_2+O_2$		-42	(R14)
	$H_2O_2+M \rightarrow OH+OH+M$		52	(R15)
	$2H+O_2 \rightarrow OH+OH$		-84	

For both reaction paths, the OH radical is finally consumed by reaction with H_2 (R3). Sensitivity calculations (Fig. 5.4.6) show that at higher pressures R11 is not important, whereas the second pathway may release significant energy through the increased exothermic formation of H_2O_2 via R14 (see Fig. 5.4.5).

Another main reaction path leading to chain branching is investigated to determine possibility of net energy release:

Path III	$H+O_2+M \rightarrow HO_2+M$	$\Delta h_{1000K}=$	-47 (kcal/mol)	(R9)
	$HO_2+H_2 \rightarrow H_2O_2+H$		24	(R17b)
	$H_2O_2+M \rightarrow OH+OH+M$		52	(R15)
	$H_2+O_2 \rightarrow OH+OH$		29	

These show that only reaction path II has potential to release significant amounts of energy at high pressure. Whereas path III is not exothermic as an energy release path, however,

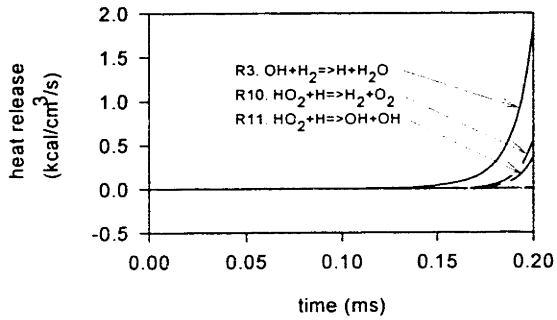

(a) p=0.1 MPa

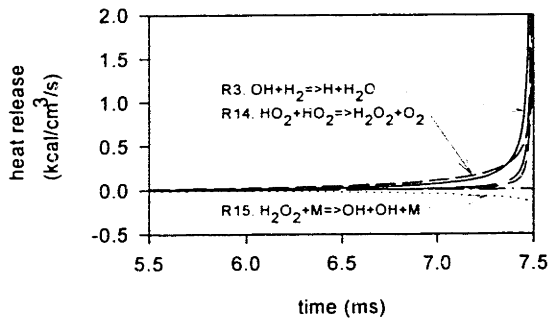

(b) p=0.3 MPa

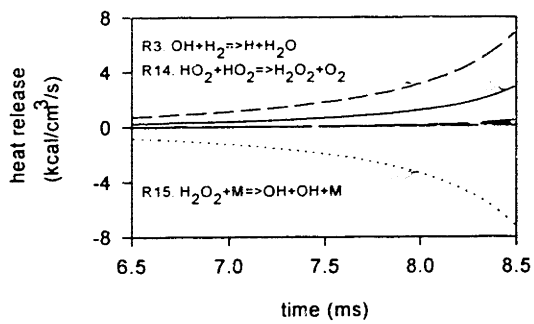

(c) p=1.0 MPa

Figure 5.4.9 Comparison of heat release rates. (a) p=0.1 MPa, (b) p=0.3 MPa, and (c) p=1.0 MPa. T_i=1000 K for all cases. Note that time spans are same for all cases to compare the relative heat release.

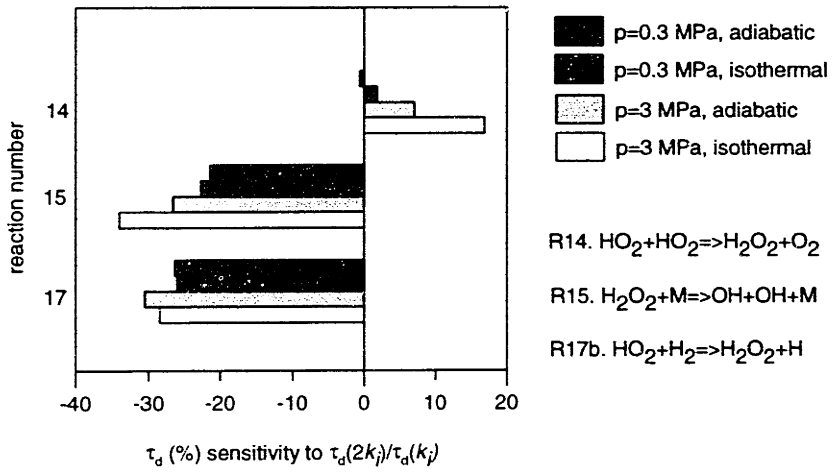

Figure 5.4.10 Induction time sensitivity comparison for reaction R14, R15 and R17. Adiabatic/isothermal calculation and different pressure ranges are used for each case. T_i=1000 K for all cases. Refer to Fig. 5.4.6 for the definition of induction time sensitivity.

path III is important as a chain branching pathway.

From the enthalpy of each species (see Fig.5.3.6) and the reaction rate constants (Table 5.3.1 or Fig 5.3.1), the energy release rate was calculated for the important reactions as shown in Fig. 5.4.9. The results indicate that at high pressures above the extended second limit (Fig. 5.4.9 (c)), R14 is the most exothermic reaction after R3 while R15 is the most endothermic reaction, and R17b is less important as an energy release path. Figure 5.4.10 compares the sensitivity of the induction time relative to these three reactions in either isothermal and adiabatic calculation. The large difference in sensitivity of τ_d to R14 in the adiabatic and isothermal cases at high pressure indicates that R14 is very important for energy release at high pressure: In contrast, R17 shows little difference in induction time sensitivity for adiabatic and isothermal cases, which indicates that R17 is responsible only for the chain branching mechanism.

5.5 Comparison between model and measurement

The model correctly captures the pressure drop due to heat loss during the induction period (see chapter 4), as well as the pressure rise prior to autoignition. Pressure histories were calculated at high (Fig.5.5.1 (a)) and low pressure (Fig.5.5.1 (b)) ranges using reaction rates by Kim *et al.* (1994) as shown in Table 5.3.1 and Table A.4.2.

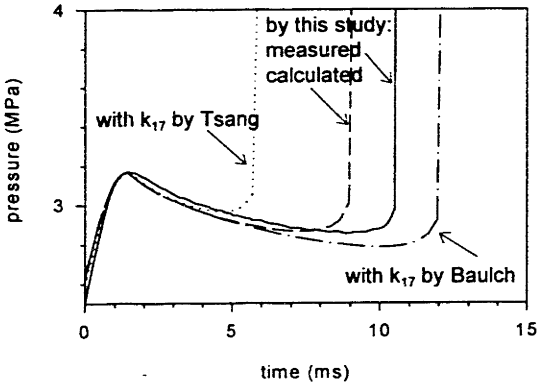

(a) T_{peak}=980 K

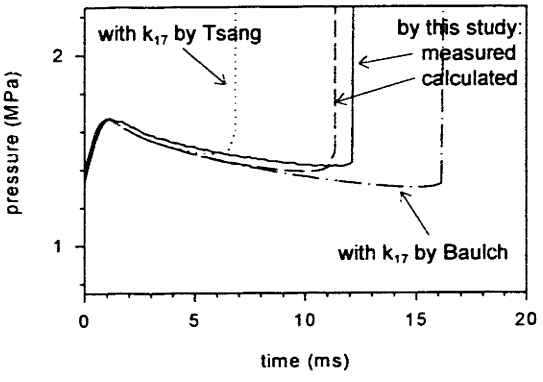

(b) T_{peak}=1000 K

Figure 5.5.1. Comparison between measured and calculated pressures.
Reaction rate constant k_{17} only was varied.

——— measured by this study
– – – – calculated by this study: $k_{17}=2.30\times10^{13}\exp(-7950/RT)$
..... Tsang *et al.* (1986): $k_{17}=4.79\times10^{13}\exp(-7950/RT)$
–·–·– D.L.Baulch *et al.* (1994): $k_{17}=1.69\times10^{12}\exp(-3750/RT)$

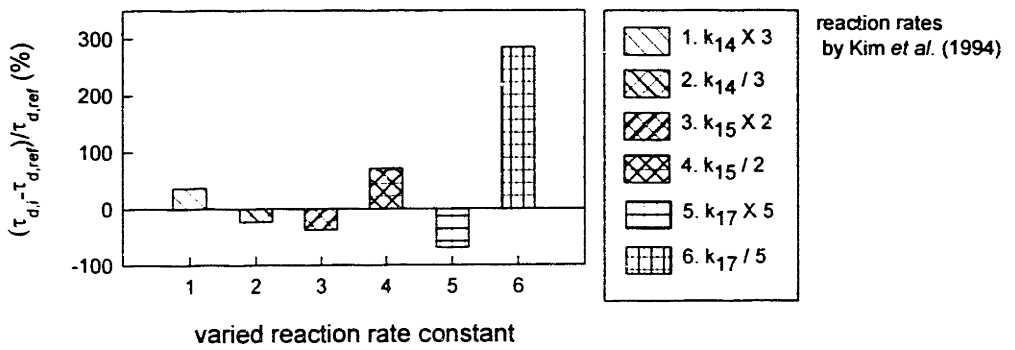

Figure 5.5.2 Comparison of calculated induction time variation in % when reaction rate constants are varied within their estimated uncertainty factor (Refer to Table 5.3.1). Reference induction time was calculated by model with L/H=8.2/0.6 cm, p_i=93.3 kPa, T_i=294 K. With reaction rates by Kim *et al.* (1994).

The calculations (dotted line) predict shorter induction times (by approximately half) compared to the measurements (solid line). The sensitivity coefficients in the previous section (Figs. 5.4.5 and Fig.5.4.6) indicate that the probable candidate reactions responsible for such discrepancies are reactions R14, R15, and R17. Figure 5.5.2 shows discrepancies between calculated induction times compared to the reference value when reaction rate constants for R14, R15, and R17 are varied within their estimated uncertainty factor (UF)* as listed in Table 5.3.1. Of these, the reaction rate constant for R17 has the largest uncertainty in its evaluation, and measurements have been available only at low to moderate temperatures (Fig. 5.5.4 and Fig.5.5.7).

An estimate for k_{17} can be made by determining the best fit parameters to assure that estimation (a) includes previous measured data, (b) is within uncertainty ranges of other estimates, and (c) matches induction times calculated and measured in this study. In order to investigate the best fit parameter values for activation energy and pre-exponential factor, measured (Refer to Table A.4.4) and calculated induction times were compared as shown in Fig. 5.5.3. Induction time deviations (in %) were calculated by:

---

* An estimated uncertainty factor UF is defined as $+\Delta k/k=UF-1$ and $-\Delta k/k=UF^{-1}-1$.

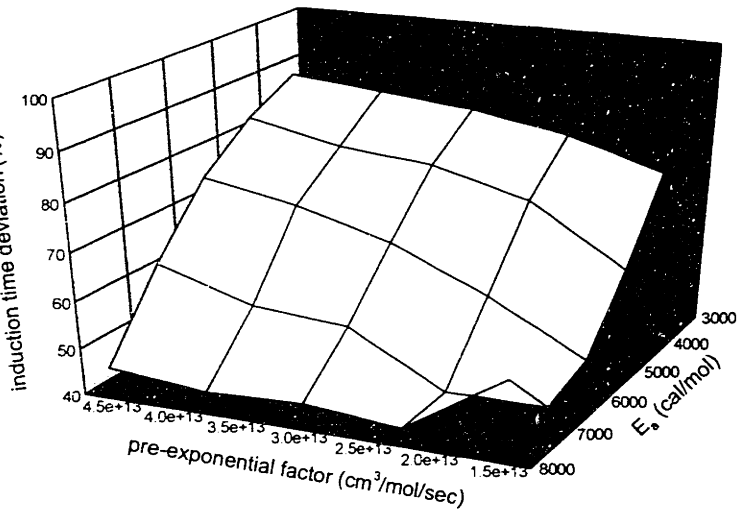

Figure 5.5.3. Distribution of calculated induction time compared to measured induction time as a function of pre-exponential factor and activation energy.

$$\text{Induction time deviation (\%)} = \frac{1}{N}\sum_{i=1}^{N}\left(\frac{\tau_{d,calculated}(i) - \tau_{d,measured}(i)}{\tau_{d,measured}(i)}\right) \times 100 \qquad (5.5.1)$$

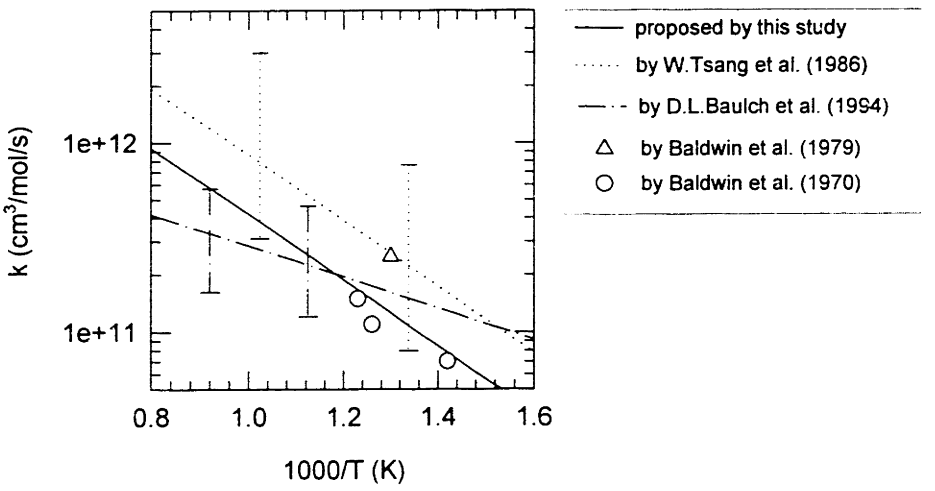

Figure 5.5.4. Reaction rate constant k_{17} for $H_2O_2+H=H_2+HO_2$.
——— proposed by this study : $k=2.30\times10^{13}\exp(-7950/RT)$
_ _ _ _ by D.L.Baulch *et al.* (1994) : $k=1.69\times10^{12}$e. p(-3750/RT), UF=2
..... by Tsang *et al.* (1986) : $k=4.79\times10^{13}\exp(-7950/RT)$, UF=5
Δ experimental data by Baldwin *et al.* (1079)
O experimental data by Baldwin *et al.* (1070)
Error bars represent uncertainty in the reported rate constant.
UF : uncertainty factor in reaction rate constant.

The result shows that, within the acceptable *ranges* (from previous estimates of this rate constant) of activation energy (3000-8000 cal/mol) and pre-exponential factor (1.5E13-4.5E13 cm^3/mol/sec), the suggested parameters show a minimum deviation of calculated induction time from measured values. With this modification for k_{17}, good agreement is found between model (dashed line in Fig.5.5.1) and experiment over the range tested. As shown in Fig. 5.5.4, the suggested reaction rate constant is located between those evaluated by Tsang *et al.* (1986) and Baulch *et al.* (1994) at temperature range of 950-1050 K.

Additional analysis was performed by comparing an induction time contour obtained from measured data with a calculated contour according to each reaction rate constant (Refer to section A.5.1 for the procedure). Figure 5.5.5 (a) shows the comparison between the induction time contour (which corresponds to 10 ms, solid line) fitted from measurements and model (dots and dot-dashes line) with k_{17} by Tsang *et al* (1986). The heat of formation for HO_2 was varied from 2.5 to 3.5 kcal/mol to determine its effect on induction time. Clearly, with this reaction rate constant the model predicts a shorter induction time. In Fig. 5.5.5 (b), calculations with the rate constant of Baulch *et al.* (1994) are compared to measurements. As discussed earlier, their rate constant leads to longer induction time predictions regardless of the heat of formation for HO_2. Finally, a comparison was made between a model with the rate constant suggested by this study and the measurements, shown in Fig.5.5.5 (c). Although the suggested reaction rate constant does not very accurately reproduce induction time over all pressure and temperature ranges tested, it is the best fit of parameters in *Arrhenius** form, that is, a function only of an activation energy and a constant pre-exponential collision factor as shown in Fig.5.5.3.

As shown in Fig.5.5.6 (a), when induction times are calculated using the reaction rates

---

* $k=A \exp(-E_a/RT)$ or $k=A\ T^n\exp(-E_a/RT)$ in a modified Arrhenius form.

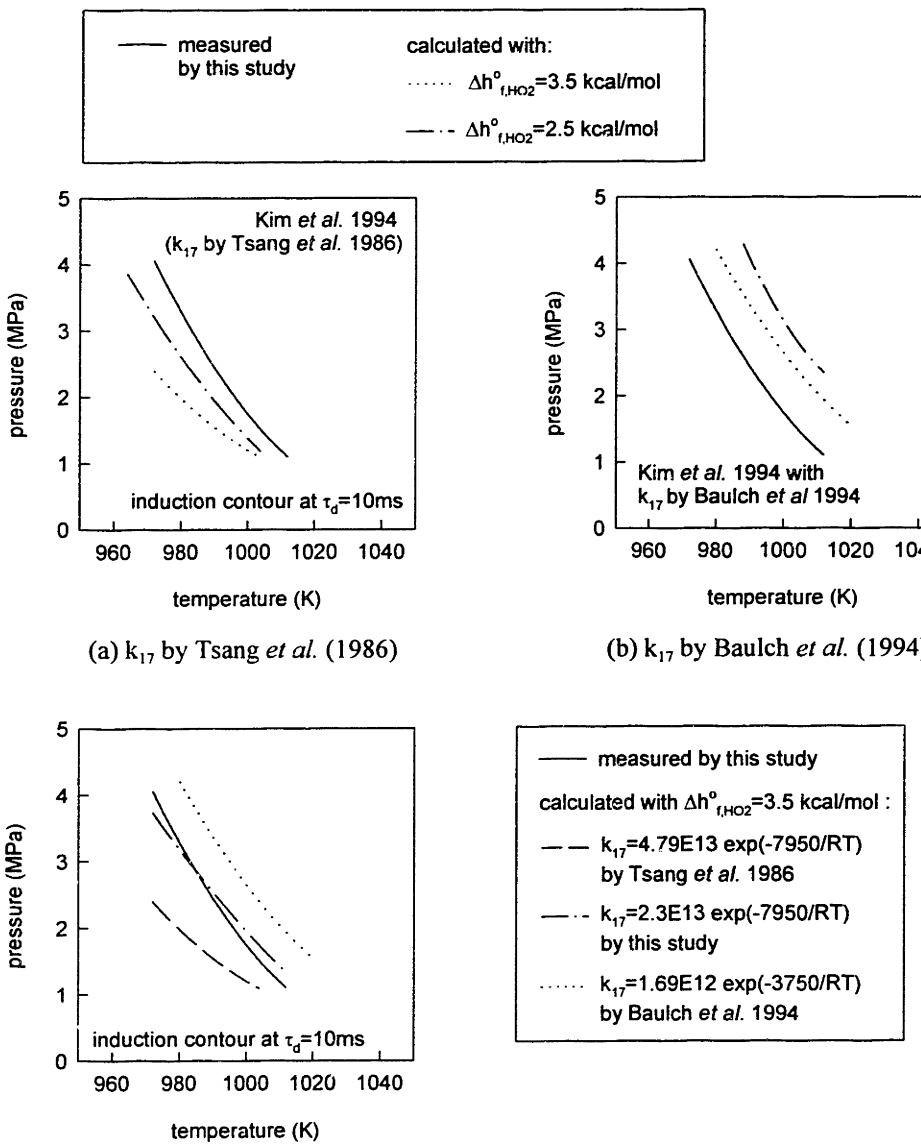

Figure 5.5.5 Comparison between measured and calculated induction time contour (τ_d=10 ms) according to each reaction rate for R17. Only reaction rate constant k_{17} and heat of formation for HO_2 were varied.

suggested by Marinov *et al.* (1995), longer times are predicted, mainly due to the differences in rate constants for R15 and R17. The effect of k_{17} (*smaller value predicts longer induction time*) has been discussed in section 5.4.2 (Also refer to section A.5.1 for comparison of reaction rate constants k_{17}). R15 is another important reaction for hydrogen oxidation at high pressures (see

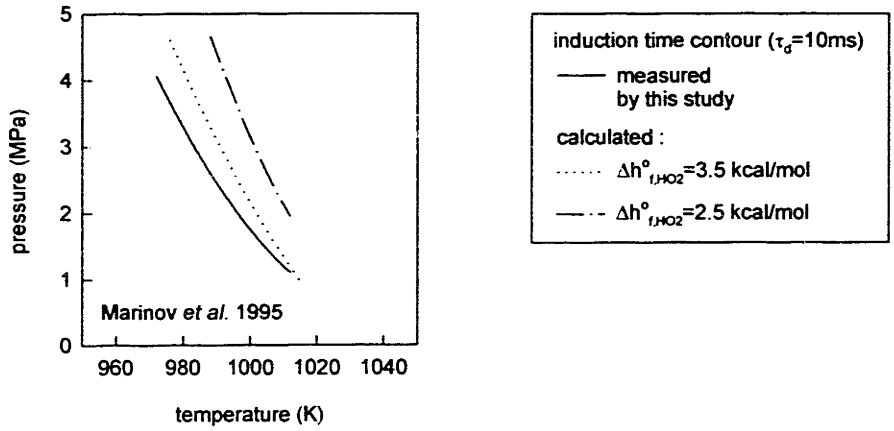

(a) Comparison between measured and calculated induction time contour. Reaction rates listed in Marivov *et al.* (1995) were used in calculation.

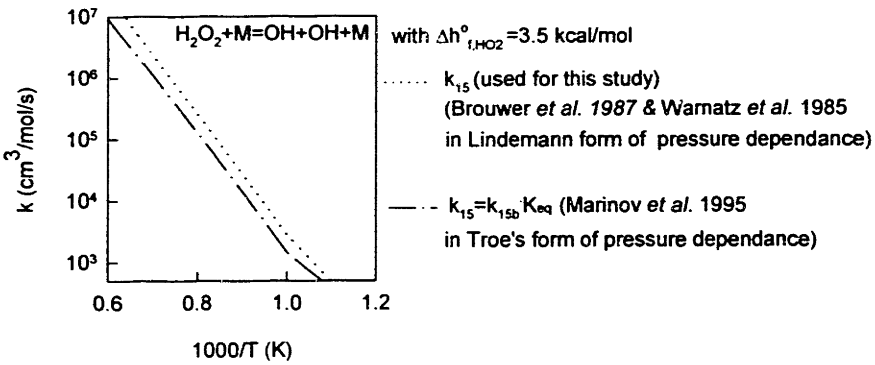

(b) Comparison between reaction rate constants for k_{15}. Refer to Table A.4.2 and A.4.3.

Figure 5.5.6 Comparison of induction time contours (τ_d=10 ms) between measurements in this study and calculation with reaction rates listed in Marinov *et al.* (1995).

Fig.5.4.6), and a larger value of the rate constant for R15 leads to a shorter induction time. It is shown in Fig.5.5.6 (b) that the rate constant k_{15} by Marinov *et al.* (1995) (which was fitted from previous measurements in a modified Arrhenius form) has a smaller value (about 50 %) and thus results in a longer induction time, as its sensitivity to induction time implies (see Fig.5.4.6). Note that reaction rates listed in Kim *et al.* (1994)*, which are used in this study, and rates listed in

* Tested ranges were at 0.1-1 MPa and 960-1200 K.

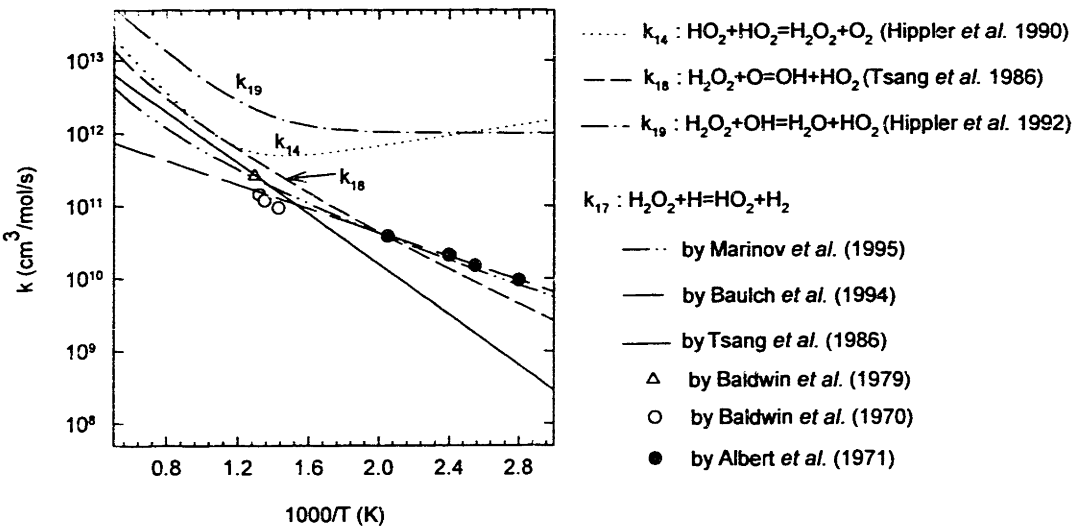

Figure 5.5.7 Comparison between reaction rate constants for k_{17}, k_{18}, and k_{19}.

in Marinov *et al.* (1995)* lead to similar predicted induction time, if the differences in reaction rates k_{15} and k_{17} are excluded. This also emphasizes the importance of accurate evaluation of these reaction rates at high pressure hydrogen oxidation.

Figure 5.5.7 shows the estimates for k_{17} at high temperatures, suggesting a higher activation energy than one at low temperature ranges (<~500 K). Although most binary elementary reactions exhibit classical Arrhenius behavior over a modest ranges of temperature, significant non-Arrhenius behavior can be exhibited over the temperature ranges encountered in combustion. Most often this variation is taken into account by finding an appropriate values of the exponent n (in T^n) such that the resulting expression accurately fits the available experimental data. Non-Arrhenius temperature dependence can generally be treated adequately through the T^n term (Westbrook 1984).

Several reactions analogous to R17 show non-Arrhenius behavior:

$$H_2O_2+H=HO_2+H_2 \qquad \text{(R17)}$$

* Tested ranges were at 0.1-0.2 MPa and 980-1176 K.

$H_2O_2+O=HO_2+OH$ (R18)

$H_2O_2+OH=HO_2+H_2O$ (R19)

In particular, R19 shows highly temperature dependent characteristics (Fig.5.5.7). Using this analogy, Marinov *et al.* (1995) fitted the reaction rate for R17 to a T^2 expression. The predicted induction time contour using their reaction rates shows different slope in pressure and temperature space than value predicted by reaction rates in a Arrhenius form (Fig. 5.5.6 (a)). Further study to evaluate this suggestion is apparently still necessary*. However, given available information, our reaction rate appears to fit all available data reasonably well.

* Although information and knowledge on reaction kinetics are not provided, additional suggestions for the reaction rate k_{17} are discussed in Appendix A.5.1 based on the best fit of measured data by this study and extrapolation of previous measured reaction rate for R17.

CHAPTER 6. CONCLUSIONS

This study developed a tool to study the high pressure autoignition of reacting mixtures, using measurements of pressure as a function of time. A special feature was created for this rapid compression machine to allow accurate characterization of mixture temperature in the reacting zone in chemical kinetic studies. The device can now be utilized to study autoignition characteristics of fuel-oxidizer mixtures. The results of this study are:

1. Previous rapid compression machine were plagued by the mixing of the reacting core gas with cold gases from boundary layer due to vigorous fluid motion during compression process. In order to prevent the core gas from being disturbed by the roll-up of the boundary layer, a new piston crevice head was designed to contain the thermal boundary layer and create well-defined core conditions. This allows more accurate predictions of the reacting temperatures to be made from the pressure-time records.
2. In order to verify that the performance of new designed piston crevice works as desired, a heat transfer model that maintains simplicity while including the effects of heat transfer and piston crevice volume was developed. This model was combined with a detailed chemical kinetic model to simulate the effect of heat transfer on the core temperatures during autoignition.
3. A model for the state of the gas mixture accurately predicted the observed pressures over a wide range of conditions with the specially designed piston. Model verification was also performed through autoignition measurements for hydrogen and oxygen mixtures in the

pressure range of 0.6 to 4 MPa and in the temperature range of 950 to 1050 K, which are above the second explosion limit.

4. Hydrogen oxidation analysis showed that, at high pressures, reactions that are *chain-branching* ($H_2O_2+H=HO_2+H_2$) and very *exothermic* ($HO_2+HO_2=H_2O_2+O_2$) can play an important role in determining the induction time. The rate constant for $H_2O_2+H=HO_2+H_2$ was identified as one of the most important reactions for hydrogen oxidation at pressures above the second explosion limit.

5. Modification to the reaction rate $H_2O_2+H=HO_2+H_2$ ($k_{17} = 2.3x10^{13}$ exp(-7950/RT)) is suggested based on measured pressure profiles and extensive sensitivity analysis, since there has been no accurate evaluation of this reaction rate constants at high temperatures. The model with the modified reaction rate agrees very well with the measured pressure profile in terms of the induction time and pressure rise due to energy release over the range tested by this study.

REFERENCE

Affleck, W.S. and Thomas, A., An Opposed Piston Rapid Compression Machine for Preflame Reaction Studies, *Proceedings of Instrumentation Mechanical Engineers*, **183** (19): 365 (1968).

Baldwin, R.R. and Walker, R.W., Rate Constants for Hydrogen+Oxygen Sytem,and for H Atoms and OH Radicals+Alkanes, *The Journal of Chemical Society, Faraday Trans. I*, **75**:140 (1979).

Balwin, R.R., Brattan, D., Tunnicliffe, B., Walker, R.W., and Webster, S.J., The Hydrogen-Sensitized Decomposition of Hydrogen Peroxide, *Combustion and Flame*, **15**:133-142 (1970).

Baldwin, R.R., Jackson, D., Walker, R.W. and Webster, S.J., Interpretation of Slow Reaction and Second Limits of Hydrogen Oxygen Mistureds by Computer Methods, *Trans. Faraday.Soc*, **63**: 1676-1686 (1967).

Baldwin, R.R., Jackson, D., Walker, R.W. and Webster, S.J., Interpretation of Induction Periods in the Hydrogen+Oxygen Reaction in Aged Boric-Acid-Coated Vessels, Trans. *Faraday.Soc*, **63**: 1665-1675 (1967).

Baldwin, R.R. and Brattan, D., Homogeneous Gas-Phase Decomposition of Hydrogen Peroxide, *Eighth (International) Symposium on Combustion*, The Combustion Institute, 110-119, 1960.

Baulch, D.L. et al., Summary Table of Evaluated Kinetic Data for Combustion Modeling: Supplement 1, *Combustion and Flame*, **98**:59-79 (1994).

Baulch, D.L. et al., Evaluated Kinetic Data for Combustion Modeling, *J.Phys.Chem.Ref.Data*, **21**(3):411 (1992).

Baulch, D.L., Griffiths, J.F., Pappin, A.J. and Sykes, A.F., Stationary-State and Oscillatory Combustion of Hydrogen in a Well-Stirred Flow Reactor, *Combustion and Flame*, **73**:163-185 (1988).

Bauch, D.L., Drysdale, D.D. and Horne, D.G., An Assessment of Rate Data for High-Temperature Systems, *Fourteenth (International) Symposium on Combustion*, The Combustion Institute, 107, 1973.

Benson, S.W., The Kinetics and Thermochemistry of Chemical Oxidation with Application to Combustion and Flames, *Prog. Energy Combust. Sci.*, 7:125-134 (1981).

Brouwer, L., Cobos, C.J., Troe, J., H. -R. Dubal and F. F. Crim, Specific Rate Constants k(E,J) and Product State Distributions in Simple Bond Fission Reactions. II. Application to HOOH→OH+OH, *The Journal of Chemical Physics*, **86**:6171 (1987).

Brussovansky, S., Heywood, J.B. and Keck, J.C., Predicting the effects of Air and Coolant Temperature, Deposits, Spark Timing and Speed on Knock in Spark Ignition Engines, *SAE paper* 922324 (1992).

Carlier, M., Corre, C., Minetti, R., Pauwels, J.-F., Ribaucour, M. and Sochet, L.-R., Autoignition of Butane: A Burner and a Rapid Compression Machine Study, *Twenty-Third Symposium (International) on Combustion*, The Combustion Institute, 1753-1758, 1990.

Carleton, K.L, Kessler, W.J. and Marinelli, W.J., $H+O_2+M$ (=N2, H_2O, Ar) Three-Body Rate Coefficients at 298-750 K, The Journal of Physical Chemistry, **97**:6412-6417 (1993).

Cheng, R.K. and Oppenheim, A.K., *Combust. Flame*, **58**:125-139 (1984).

Chung, T.J. et al., *Numerical Modeling in Combustion*, Taylor & Francis, 1993.

Cobos, C.J., Hippler, H. and Troe, J., High-Pressure Falloff Curves and Specific Rate Constants for the Reactions $H+O_2=HO_2=HO+O$, *The Physical Chemistry*, **89**:342-349 (1985).

Colella, K.J., Bailes, E.N., Ekchian, J.A., Cheng, W.K. and Heywood, J.B., A Rapid Compression Machine Study of the Influence of Charge Temperature on Diesel Combustion, *SAE paper* 870587 (1987).

Daneshyar, H., Fuller, D.E. and Deckker, B.E.L., Vortex Motion Induced by the Piston of an Internal Combustion Engine, *International Journal of Mechanical Society*, **15**: 381-390 (1973).

Dixon-Lewis, G., Greenberg, J.V. and Goldsworthy, F.A., Reactions in the Recombination Region of Hydrogen and Lean Hydrocarbon Flames, *Fifteenth (International) Symposium on Combustion*, The Combustion Institute, 717, 1975.

Dixon-Lewis, G., Flame Structure and Flame Reaction Kinetics. V. Investigation of Reaction Mechanism in a Rich Hydrogen-Nitrogen-Oxygen Flame by Solution of Conservation Equations, *Proc. Roy. Soc. Lond. A.* 317:235-263 (1970).

Dougherty, E.P. and Rabitz, H., Computational Kinetics and Sensitivity Analysis of Hydrogen-Oxygen Combustion, *The Journal of Chemical Physics*, **72**(12):6571 (1980).

Dryer, F.L. and Glassman, I., High-Temperature Oxidation of CO and CH_4, *Fourteenth (International) Symposium on Combustion*, The Combustion Institute, 987, 1973.

Elsworth, J.E., Haskell,W.W. and Read I.A., Non-uniform Ignition Processes in Rapid-compression Machines, *Combustion and Flame*, **13**:437 (1969).

Ely, J.F. and Huber, M.L., *NIST Thermophysical Properties of Hydrocarbon Database (SUPERTRAPP)*, Ver1.0, National Institute of Standards and Technology, 1992.

Frank, J., Griffiths, J.F. and Nimmo, W., The Control of Spontaneous Ignition Under Rapid Compression, *Twenty-first Symposium (International) on Combustion*, The Combustion Institute, 447-454, 1986.

Furutani, M., Ohta, Y. and Momatsu, K., Onset Behavior of Low Temperature Flames caused by Piston Compression, *SAE paper* 9303429 (1993).

Gas Kinetics and Energy Transfer, The Chemical Society, Vol.2, 1977.

Getzinger, R.W. and Schott, G.L., Kinetic Studies of Hydroxyl Radicals in Shock Waves. V. Recombination via the $H+O_2+M=HO_2+M$ Reaction in Lean Hydrogen-Oxygen Mixtures. *The Journal of Chemical Physics*, **43**(9):3237-3247 (1965).

Gray, P., Chemistry and Combustion, *Twenty-Third Symposium (International) on Combustion*, The Combustion Institute, 1-19, 1990.

Gray, P. and Sherrington, M.E., Explosive Oxidation of Hydrogen Sulfide : Self-heating, Chain-branching and Chain-thermal Contributions to Spontaneous Ignition, *J.C.S.Faraday I*, **70**:2336 (1974).

Gray, P. and Ip, J.K.K., Spontaneous Ignition Supported by Chlorine Dioxide. I. Chlorine Dioxide Alone and with Diluents, *Combustion and Flame*, **18**:361-371 (1972).

Gray, B.F. and Yang, C.H., The Present Theoretical Position in Explosion Theory, *Eleventh Symposium (International) on Combustion*, The Combustion Institute, 1057-1061,1967.

Gray, B.F. and Yang, C.H., On the Unification of the Thermal and Chain Theories of Explosion Limits, *The Journal of Physical Chemistry*, **69**(8): 2747 (1965).

Griffiths, J.F., Jiao, Q., Kordylewski, W., Schreiber, M., Meyer, J. and Knoche, K.F., Experimental and Numerical Studies of Ditertiary Butyl Peroxide Combustion at High Pressures in a Rapid Compression Machine, *Combustion and Flame*, **93**: 303-315 (1993).

Griffiths, J.F., Rose, D.J., Schreiber, M., Meyer, J. and Knoche, K.F., Novel Features of End-Gas Autoignition Revealed by Computational Fluid Dynamics, *Combustion and Flame*, **91**:209-212, (1992).

Griffiths, J.F., Jiao, Q., Schreiber, M., Meyer, J. and Knoche, K.F., Development of Thermokinetic Models for Autoignition in a CFD Code: Experimental Validation and Application of the Results to Rapid Compression Studies, *Twenty-Fourth Symposium (International) on Combustion*, The Combustion Institute, 1809-1815, 1992.

Griffiths, J.F. and Nimmo, W., Spontaneous Ignition and Engine Knock under Rapid Compression, *Combustion and Flame*, **60**:215-218 (1985).Griffiths, J.F. and Perche, A., The Spontaneous Decomposition, Oxidation and Ignition of Ethylene Oxide Under Rapid Compression, *Eighteenth Symposium (International) on Combustion*, The Combustion Institute, 893, 1981.

Gutman, D., Hardwidge, E.A., Dougherty, F.A. and Lutz, W., Shock-Tube Study of the Recombination Rate of Hydrogen Atoms with Oxygen Molecules, *The Journal of Chemical Physics*, **47**:11, 4400-4407 (1967).

Gyftopoulos, E.P. and Beretta, G.P., *Thermodynamics Foundations and applications*, Macmillan Publishing Company, 1991.

Halstead, M.P., Kirsch, L.J. and Quinn, C.P., The Autoignition of Hydrocarbon Fuels at High Temperature and Pressures - Fitting of a Mathematical Model, *Combustion and Flame*, **30**: 45-60 (1977).

Harding, L.B. and Wagner, A.F., Theoretical Study of the Reaction Rates of OH+OH=H_2O+O, *Twenty-Second Symposium (International) on Combustion*, The Combustion Institute, 983-989, 1988.

Haskell, W.W., Fuel Ignition in a Rapid Compression Machine : Sensitivity to Flame Ignition by Particles, *SAE paper* 700059 (1970).

Hayashi, T., Taki, M., Kojima, S. and Kondo, T., Photographic Observation of Knock with a Rapid Compression and Expansion Machine, *SAE paper* 841336 (1984).

Heywood, J.B., *Internal Combustion Engine Fundamentals*, McGraw Hill, 1988.

Hills, J.A. and Howard, C.J., Rate Coefficient Temperature dependence and branching ratio for the OH+CIO Reaction, *J.Chem.Phys.*, **81**(10), 4458, 1984.

Hippler, H. and Troe, J., Rate Constants of the Reaction HO+H_2O_2→HO_2+H_2O at T ≥1000 K, *Chemical Physics Letter*, **192**:333 (1992).

Hippler, H., Troe, J. and Willner, J., Shock wave study of the reaction HO2+HO2=H2O2+O2 : Confirmation of a rate constant minimum near 700 K, *The Journal of Chemical Physics*, **93**(3):1755 (1990).

Hochgreb, S., *An Experimental and Numerical Study of the Oxidation of Formaldehyde*, Ph.D. Thesis, Princeton University, 1991.

Homer, J.B. and Hurle, I.R., The dissociation of water vapor behind shock waves, *Proc. Roy. Soc. Lond. A.* 314, 585-598 (1970).

Hsu, K.J., Anderson, S.M., Durant, J.L. and Kaufman, F., Rate Constants for H+O_2+M from 298 to 639 K for M=H_2, N_2, and H_2O, *The Journal of Physical Chemistry*, **93**:1018-1021 (1989).

Irvin Glassman, *Combustion*, 2nd ed., Academic Press, 1987.

Keck, J.C., Thermal Boundary Layer in a Gas subject to a Time Dependent Pressure, *Letters in Heat and Mass Transfer*, **8**:313-319 (1981).

Kee, R.K, Rupley, F.M. and Miller, J.A., CHEMKIN II: A Fortran Chemical Kinetics Package for the Analysis of Gas-Phase Chemical Kinetics, *Sandia Report*: SAND89-8009, 1990.

Kee, R.K., Rupley, F.M. and Miller, J.A., The CHEMKIN thermodynamic database, *Sandia Report*: SAND80-8003, 1987.

Kim, T.J., Yetter, R.A. and Dryer, F.L., New Results on Moist CO Oxidation: High Pressure, High Temperature Experiments and Comprehensive kinetic modeling, *Twenty-fifth Symposium (international) on Combustion* , The Combustion Institute, 759-766, 1994.

Kordylewski, W. and Scott, S.K., The Influence of Self-Heating on the Second and Third Explosion Limits in the O_2+H_2 Reaction, *Combustion and Flame*, **57**:127-139 (1984).

Lai, M.-C., Zhou, B., Cheng, W.K., Wong, V.W. and Benedek, K.R., Parametric Studies of Coal-Water Slurry Combustion in a Rapid Compression Machine, *ASME*:87-ICE-9, Dallas, Texas, February (1987).

Lee, D., *Autoignition Measurement of Oxygenated Fuels in a Rapid Compression Machine*, M.S. Thesis, MIT, 1993.

Lee, D. and Hochgreb, S., Measurement and Modeling of Heat transfer Characteristics in a Rapid Compression Machine, *The Eighth International Symposium on Transport Phenomena in Combustion*, San Francisco (1995).

Lewis, B. and Elbe, G.V, Combustion, Flames and Explosions of Gases, Academic Press, 1987.

Lifshitz, A. and Michael, J.V., Rate Constants for the Reaction, $O+H_2O \rightarrow OH+OH$, Over the Temperature range, 1500-2400 K, By the Flash Photolysis-shock Tube Technique: A Further Consideration of the Back Reaction, *Twenty-Third Symposium (International) on Combustion*, The Combustion Institute, 59-67, 1990.

Lutz, A.E., Kee, R.J. and Miller, J.A., SENKIN: A Fortran Program for Predicting Homogeneous Gas Phase Kinetics with Sensitivity Analysis, *Sandia National Laboratories Report* No. SAND87-8248, 1990.

Marinov, N.M., Westbrook, C.K. and Pitz, W.J., Detailed and Global Chemical Kinetics Model for Hydrogen, *The Eighth International Symposium on Transport Phenomena in Combustion*, San Francisco (1995).

Maas, U. and Warnatz, J., Ignition Processes in Hydrogen-Oxygen Mixtures, *Combustion and Flame*, **74**:53-69 (1988).

Mass, U. and Warnatz, J., Ignition Processes in Carbon-Monoxide-Hydrogen-Oxygen Mixtures, *Twenty-Second Symposium (International) on Combustion*, The Combustion Institute, 1695-1704, 1988.

Meyer, J.M. and Oppenheim, A.K., On the Shock-induced Ignition of Explosive Gases, *Thirteenth Symposium (International) on Combustion*, The Combustion Institute, 1153, 1971.

Nikanjam, M. and Greif, R., Heat Transfer During Piston Compression, *The Journal of Heat Transfer*, **100**(3): 527 (1978).

Norton, T.S. and Dryer, F.L., Some New Observations on Methanol Oxidation Chemistry, *Combust. Flame*, **63**:107-129, 1989

Ohta, Y., Kadowaki, S., Terada, K. and Takahasi, H., Effect of Turbulent Fluid Motion on Low-Temperature Autoignition of Fuel-Air Mixture Under Piston Compression, *Progress in Astronautics and Aeronautics*, The American Institute of Aeronautics and Astronautics, 395 (1990).

Ohta, Y., Hayashi, K., Fujiwara, T. and Takahashi, H., n-Butane Ignition in a Wide Range of Temperatures, *Progress in Astronautics and Aeronautics, American Institute of Aeronautics and Astronautics*, **113**: 225-237 (1988).

Ohta, Y., Hayashi, K., Fujiwara, T. and Takahashi, H., *Progress in Astronautics and Aeronautics, American Institute of Aeronautics and Astronautics*, **105**: 93-103 (1986).

Oldenborg, R.C., Loge, G.W., Harradine, D.M. and Winn, K.R., Kinetic Study of the OH+H2 Reaction from 800 to 1550 K, *The Journal of Physical Chemistry*, **96:**8426-8430 (1992).

Ohta, Y. and Takahashi, H., Homogeneous and Propagation of Autoignited Cool and Blue Flames, *Progress in Astronautics and Aeronautics, American Institute of Aeronautics and Astronautics*, 236 (1984).

Oran, E.S. and Boris, J.P., Weak and Strong Ignition. II. Sensitivity of the Hydrogen-Oxygen System, *Combustion and Flame*, **48**:149-161 (1982).

Oran, E.S., Young, T.R, Boris, J.P. and Cohen, A., Weak and Strong Ignition. I. Numerical Simulation of Shock Tube Experiments, *Combustion and Flame*, **48**:135-148 (1982).

Park, P., *Rapid Compression Machine Measurements of Ignition Delays for Primary Reference Fuels*, Ph.D. Thesis, MIT, 1990.

Park, P. and Keck, J.C., Rapid Compression Machine Measurements of Ignition Delays for Primary Reference Fuels, *SAE Paper* 900027 (1990).

Patrick, R., Barker, J.R. and Golden, D.M., Computational Study of the HO_2+HO_2 and DO_2+DO_2 reactions, *The Journal of Physical Chemistry*, **88**:128 (1984).

Peters, N. *et al.*, *Reduced Kinetic Mechanisms for Applications in Combustion Systems*, Springer-Verlag, 1993.

Ritter, E.R. and Bozzelli, J.W., Dept. of Chemical Engineering, Chemistry, and Environmental Science, New Jersey Institute of Technology, March 16,, 1987.

Schreiber, M., Sadat Sakak, A., Poppe, C., Griffiths, J.F., Halford-Maw, P. and Rose, D.J., Spatial Structure in End-Gas Autoignition, *SAE paper* 932758 (1993).

Schott, G.L. and Kinsey, J.L., Kinetic Studies of Hydroxyl Radicals in Shock Waves. II. Induction Times in the Hydrogen-Oxygen Reaction, *The Journal of Chemical Physics*, **29**:1177 (1958).

Senkan, S.M., Detailed Chemical Kinetic Modeling: Chemical Reaction Engineering of the Future, *Advances in Chemical Engineering*, **18**:95-196 (1992).

Shum,G.S. and Benson,S.W., Review of the Heat of Formation of the Hydroperoxyl Radical, *J.Phys.Chem.*, **87**:3479-3482 (1983).

Skinner, G.B. and Ringrose, G.H., Ignition Delays of a Hydrogen-Oxygen-Argon Mixtures at Relatively Low Temperature, *The journal of Chemical Physics*, **42**(6):2190 (1965).

Slack, M.W., Rate Coefficient for $H+O_2+M=HO_2+M$ Evaluated from Shock Tube Measurements of Induction Times, *Combustion and Flame*, **28**:241-249 (1977).

Steinfeld, J.I., Francisco, J.S. and Hase, W.L, *Chemical Kinetics and Dynamics*, Prentice Hall, 1989.

Tabaczynski, R.J., Hoult, D.P. and Keck, J.C., High Reynolds Number Flow in a Moving Corner, *The Journal of Fluid Mechanics*, **42**: 249-255 (1970).

Taylor, C.F. et al., The Ignition of Fuels by Rapid Compression, *SAE Annual Meeting*, Detroit, Michigan, January (1950).

Tsang, W. and Hampson, R.F., Chemical Kinetic Data Base for Combustion Chemistry. Part I. Methane and Related Compounds, *The Journal of Physical Chemistry*, **15**:1087 (1986).

Wang, H. and Frenklach, M., Modification of Troe's fall-off broadening, *Chemical Physics Letter*, 205:271 (1993).

Westbrook, C.K. and Dryer, F.L., Chemical Kinetic Modeling of Hydrocarbon Combustion, *Prog. Energy Combust. Sci.*, **10**:1-57 (1984).

Yang, C.H. and Gray, B.F., The Determination of Explosion Limits from a Unified Thermal and Chain Theory, *Eleventh Symposium (International) on Combustion*, The Combustion Institute, 1099-1106, 1967.

Yetter, R.A., Rabitz, H. and Hedges, R.M., A Combined Stability-Sensitivity Analysis of Weak and Strong Reactions of Hydrogen/Oxygen Mixtures, International Journal of Chemical Kinetics, **23**:251- 278 (1991).

Yetter, R.A., Dryer, F.L. and Rabitz, H., Flow Reactor Studies of Carbon Monoxide/ Hydrogen/Oxygen Kinetics, *Combustion Science and Technology*, **79**:129-140 (1991).

Yetter, R.A., F. L. Dryer and Rabitz, H., A Comprehensive Reaction Mechanism for Carbon Monoxide/Hydrogen/Oxygen Kinetics, *Combustion Science and Technology*, **79**:97-128 (1991).

Yetter, R.A., Dryer, F.L. and H. Rabitz, Complication of One-Step Kinetics for Moist CO Oxidation, *Twenty-First Symposium (international) on Combustion*, The Combustion Institute, 749-760, 1986.

Yetter, R.A., Dryer, F.L. and Rabitz, H., Some Interpretive Aspects of Elementary Sensitivity Gradients in Combustion Kinetics Modeling, *Combustion and Flame*, **59**:107-133 (1985).

APPENDIX 1. PISTON O-RING CREVICE VOLUME

The piston O-ring pack (O-ring and back-up rings) moves along O-ring groove depending on the pressure difference at both sides. A hypothesis was made (Refer to section 2.5.3), by which the piston O-ring crevice volume was calculated using the geometry of a piston head. Experimental estimation of O-ring pack motion was available, hence the piston O-ring crevice volume was calculated from experimental data as well. Both results agreed well, thus validated the hypothesis of O-ring pack motion.

In order to use pressure records to calculate volumetric change, some preliminary analyses are necessary : (i) Leakage during operating of the RCM including *blow-by* along piston O-ring should be prevented. (ii) Volumetric resolution available from pressure record should be accurate enough. Discussions on these points follow.

A.1.1. Leakage (*blow-by*)

During operation of the RCM, efforts were made to avoid unacceptable leakage across the gas feeding valve and blow-by. Leakage across the gas feeding valve was monitored by MKS pressure gauge during operating of the machine and assured not to occur (Regular replacement of O-ring (2-011) around the gas feeding valve was necessary as will be discussed in section A.2.1).

Blow-by leakage was also regularly checked by monitoring the MKS pressure gauge after firing the machine. As shown in Fig.2.3.3 and Fig. A.1.1.1, gas feeding valve was opened

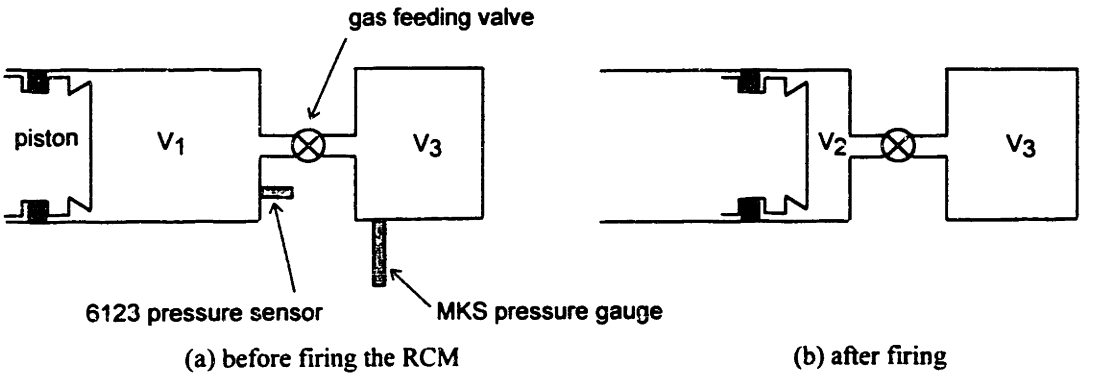

Figure A.1.1.1 Schematic diagram of volume change. (a) the valve was closed and RCM started compressing the gas. (b) after firing (t>10 s), the valve was opened and mixing was allowed. For both cases the total volume is closed (*if no blow-by exists*).

after the firing and pressure was recorded to investigate blow-by leakage, since the gap through piston O-ring is the only path available for leakage.

After firing the RCM, as shown in Fig.2.3.3 (b) the pressure drop shows that the cylinder gas cools to the wall temperature through gradient of $(\overline{T}_{t=10s} - \overline{T}_{t=30s}) / \overline{T}_{t=30s} \approx 0.007$, which corresponds to about 2 K at this temperature range. Thus, after about 10 seconds or more elapse, the cylinder gas is almost at the wall temperature. Note that the resolution of pressure sensor (Kistler 6123) is about 4.88 kPa corresponding to a resolution of 0.1 cm^3 of volume approximately. Also, minimum resolution of MKS pressure gauge (0.1 mmHg) can discern about 0.1 cm^3 of volumetric change within about 1000 cm^3 range.

From Fig. A.1.1.1, and the isothermal relation for ideal gas leads to

$$V_1 + V_3 = \frac{\pi R^2 L + \Delta V_{cr}}{1 - p_{t=0} / p_{t>10s}} \qquad \text{(A.1.1.1)}$$

where R is a radius of the combustion chamber and $\Delta V_{cr} = V_{cr,t=0} - V_{cr,t>10s}$.

Figure A.1.1.2 shows the calculated total volume from the measured pressure ratio of p(t=0)/p(t>10s). When autoignition was observed, that is, high and very rapid pressure occurred, blow-by leakage was observed. No appreciable leakage accompanied compression process, as also confirmed from measurement as in Fig.2.3.3.

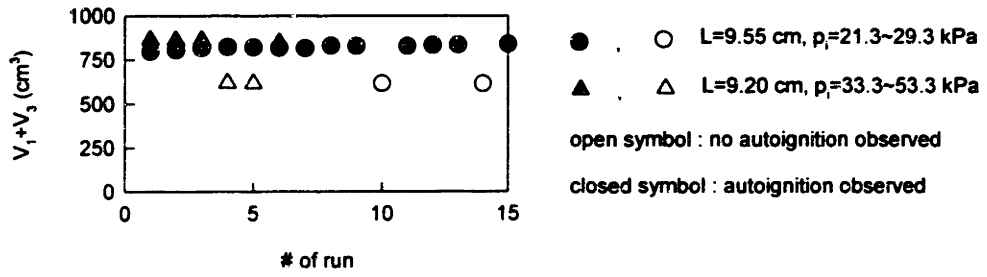

Figure A.1.1.2 Calculated total volume from measured pressure difference showing that when autoignition was observed, *i.e.* at high and very rapid pressure rise, blow-by leakage was observed. ΔV_{cr}=1.15 cm^3. 15 and 6 consecutive runs with different stokes were tested.

A.1.2. Piston O-ring crevice volume

Figure A.1.1.3 compares the measured profile with piston head #1 (in Fig.2.5.3 (a)) and #2 (in Fig.2.5.3 (b)), in which the piston crevice volume was increased (relative to head #1) to investigate the O-ring pack motion. The result shows that the pressure profile with piston head #2 differs from that with piston head #1 when the cylinder pressure drops down to values corresponding to temperature close to the wall temperature (t>~5 sec). It is noted that, during compression and at the peak, the pressure does not differ between the both cases shown in Fig.A.1.1.3 (a). Isothermal pressure difference results only from volumetric difference, which validates the hypothesis of O-ring motion as described in section 2.5.3. O-ring crevice volumes were calculated based on this results.

By comparing the measured initial (at t=0 s) and final pressures (at t=30 s) as in Fig.2.3.3, the change of crevice volume (including O-ring crevice) can be calculated from known stroke and clearance height data. Thus, $V_{cr(t=30s)} - V_{cr(t=0)} \approx 1.23$ cm^3, which is close to the calculated value of 1.37 cm^3 according to the geometry of Fig.2.5.6 (c).

From isothermal pressure difference (at t=4s in Fig.A.1.1.3 (b)) between two piston heads, the volumetric difference was calculated as

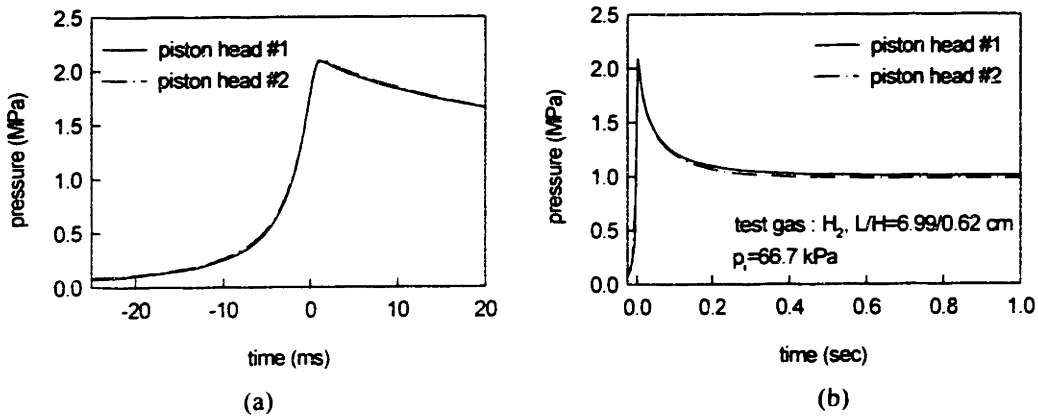

Figure A.1.1.3 A comparison of measured pressure profiles between different piston heads. Time span in (a) is to compare peak pressure and that in (b) is to compare isothermal pressure after relatively long time elapsed. Piston head #2 has larger cylinder volume than #1, which can explain why the O-rings move according to the hypothesis represented in Fig.2.5.6 (c).

$$\Delta V_{cr(\#1\sim\#2)} = 0.034 V_{\text{O-ring crevice}} + 0.46 \ (\text{cm}^3) \qquad \text{(A.1.1.2)}$$

The difference in O-ring groove volume between piston head #1 and #2, as shown in Fig.2.5.3, is 0.37 cm^3. Thus, from Eq.(A.1.1.2) ΔV is 0.50 cm^3, which is close to 0.37 cm^3, if considering that the volume being able to be discerned from the pressure difference is about 0.1 cm^3.

To calculate the volume of piston O-ring crevice as a function of time, the following empirical relation is used:

$$V_{\text{O-ring crevice}} = 1.37\left(1 - e^{-t^{0.6}/\tau}\right) \ \text{cm}^3 \qquad \text{(A.1.1.3)}$$

where τ is assumed to be about 15 ms and t (in ms) corresponds to time elapsed after the

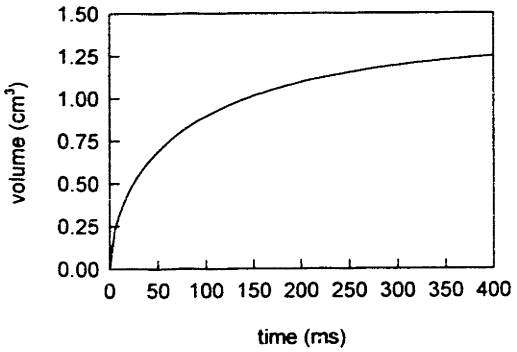

Figure A.1.1.4. Estimated piston O-ring crevice volume as a function of time elapsed after the compression process.

compression process. Experimental observations, shown in Figs. 2.2.4 and A.1.1.3, enable the determination of a time constant used to calculate O-ring crevice volume. Within the order of tens of milliseconds, O-ring packs start moving due to the higher pressure in the combustion chamber than in the hydraulic oil chamber (refer to Fig.A.1.1.1), and are squeezed to the other side (away from combustion chamber) of the O-ring groove. This all happens during about a few hundreds of milliseconds. Comparison between model and measurements (discussed in section 4.2) validates this hypothesis of piston O-ring motion. Figure A.1.1.4 shows a variation of the piston O-ring crevice volume after the compression process.

APPENDIX 2. TEST FAILURES AND DIAGNOSES

During operation of the rapid compression machine, failed test runs have been also observed. Some are related to solely human error or malfunctioning of the machine, whereas some result from the unknown reasons which have not yet been clarified. Whereas the current observations are particular to this machine, rapid compression machine measurements have been claimed to be difficult to be reproduced by well repeatable pressure records.

Mechanical failure including *O-ring failure* can be fixed relatively easily once the failed ring is identified. In some cases, reason for the abnormal* operation (possible ignition due to oil layer and/or piston corner vortex) have not been clearly identified. However, promising results have been observed since the piston head was replaced by the new design (Fig.2.5.3 (f)).

To understand the performance and limitations of the rapid compression machine, failed tests found in this study were classified and listed with the available diagnoses for them at the following. This results can be used to improve the rapid compression machine for future work.

A.2.1. Failed tests due to mechanical failure

Figure A.2.1.1 shows the installed locations of O-rings in the rapid compression machine. Several of them are installed for dynamic sealing. Their failures have been often observed based on corresponding pressure records, then a failed O-ring was identified and replaced.

The O-ring 2-011 acts to seal the combustion chamber during compression and induction O-ring is usually observed. Two methods of detection are available: (a) Before and after the

* Runs accompanied by pressure records showing that trends (not repeatable) are deviated from generally acceptable characteristics (repeatable) and resulted from unidentified sources.

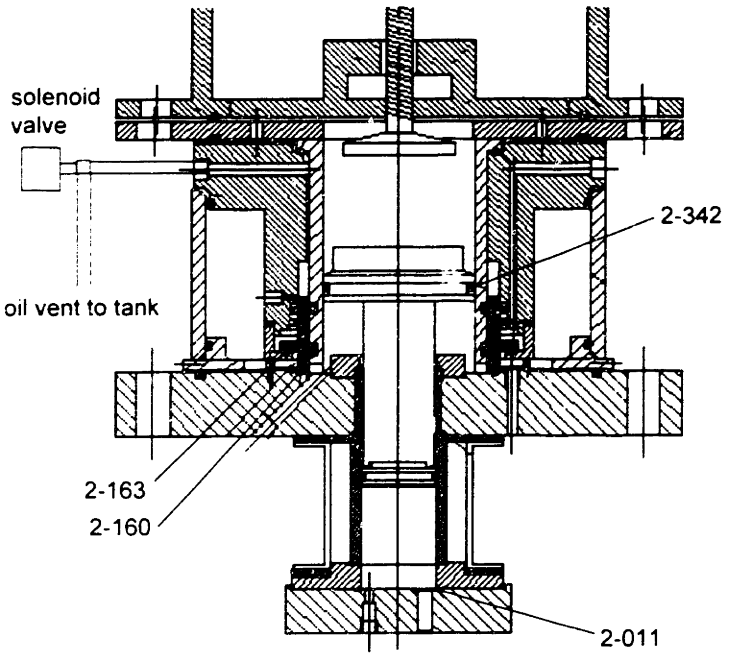

Figure A.2.1.1 Installed locations of O-ring in a rapid compression machine.

compression process any pressure difference read by MKS pressure sensor, located near the gas feeding valve as shown in Fig. 2.2.3, can monitor the failure of this O-ring. (b) During operation the machine the pressure record at times indicated the fatal failure of the O-ring 2-011 as shown in Fig. A.2.1.2 (a).

The O-ring 2-342 is located at the periphery of the driving piston head. Upon failure*, a pressure record as in Fig.A.2.1.2 (b) is obtained. Static diagnosis of proper functioning of this O-ring is possible by reading the pressure gauge for the driving air chamber and the hydraulic oil pressure to sustain the piston. Any pressure change of these two gauges for a relatively long time (~10 min) indicates that the O-ring 2-342 fails to seal between the driving air chamber and the driving side.

---

* Typically via abrasion : appearance shows a flat area on one side of O-ring cross section, where moving contact is made with the metal component, caused by too rough or too smooth metal surface.

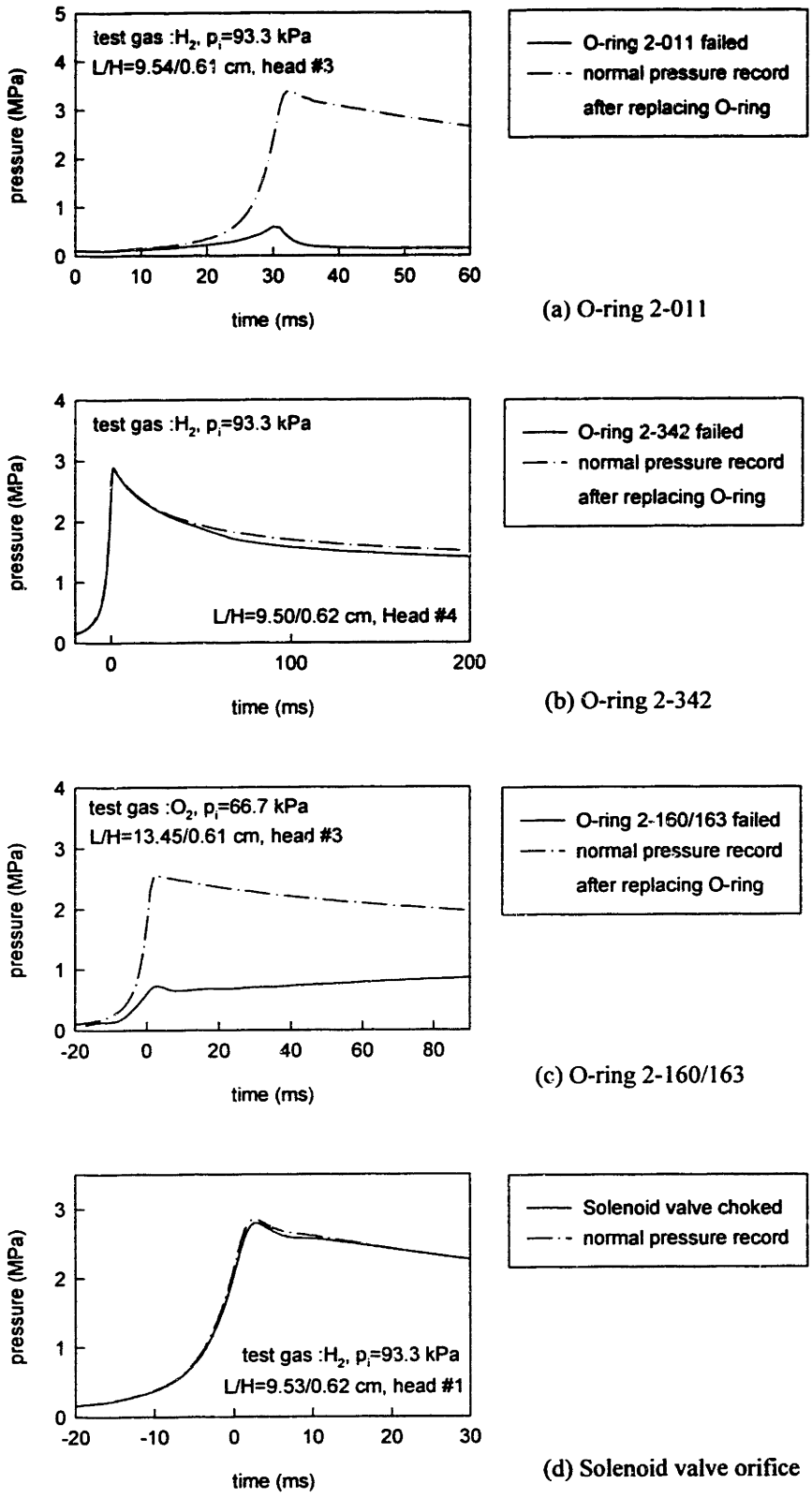

Figure A.2.1.2 Pressure records showing malfunctioning of the RCM compared to normal pressure records.

Proper functioning and good maintenance of O-rings 2-160 and 2-163 are very critical for the operation of the machine. The O-ring groove for O-ring 2-163 has been redesigned by a dove-tail groove, hence the pop-up of O-ring 2-163 has been prevented. However, failed pressure records due to the failure* of O-ring 2-160 at times have been observed as in Fig. A.2.1.2 (c). The durability of this O-ring was extended by lowering the operating hydraulic oil pressures to sustain the driving piston down to 1.25 MPa.

Finally, figure A.2.1.2 (d) shows a failed test when the orifice of the solenoid valve, through which hydraulic oil is released, was choked by small particles.

* Spiral failure : appearance exhibits a deep spiral cut (usually at about 45°) into the O-ring cross section. It is caused by the condition that the O-ring generally gets pinched or "hung-up" at one point of its periphery.

A.2.2. Abnormal ignition in pure oxygen tests

Abnormal ignition due to unidentified causes has been observed at times (neither repeatable, nor regular). A few of them obviously result from autoignition of alcoholic cleaner used to clean the combustion chamber in assembling combustion chamber parts. As shown in Fig. A2.2.1, an abnormal pressure record has observed resulting from the chemical reaction due to small amounts of alcoholic cleaner present in the chamber. It is noted that this type of pressure record was available only in cases that alcoholic cleaner (pure methyl alcohol) was used and not allowed to dry thoroughly before firing the machine. This is presented to compare to the following case, however, this is not of interest in this work.

An *oxygen dummy run* was suggested between each fuel + oxygen run to burn up any possible residuals from a previous run (Park 1990). In this study, oxygen dummy runs did not enhance the repeatability of measurements. Hydrogen oxidation (as discussed in Chapter 5.) was performed without oxygen dummy runs and showed good repeatability, presumably no intermediate products were absorbed on walls or lubricating oil. Oxygen dummy runs may apply to hydrocarbon oxidation measurements, where very small amount of residuals can alter the overall oxidation characteristics. As shown in Fig. A2.2.2, pure oxygen runs were accompanied

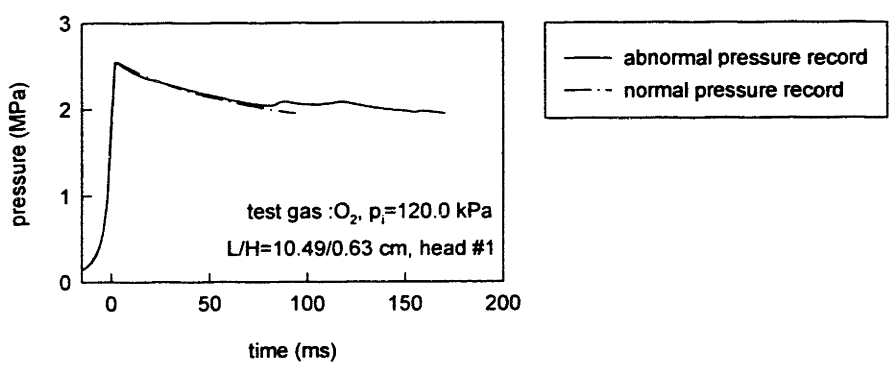

Figure A.2.2.1 Abnormal pressure records for oxygen runs. This obviously results from the alcohol residuals used to clean the chamber before this run.

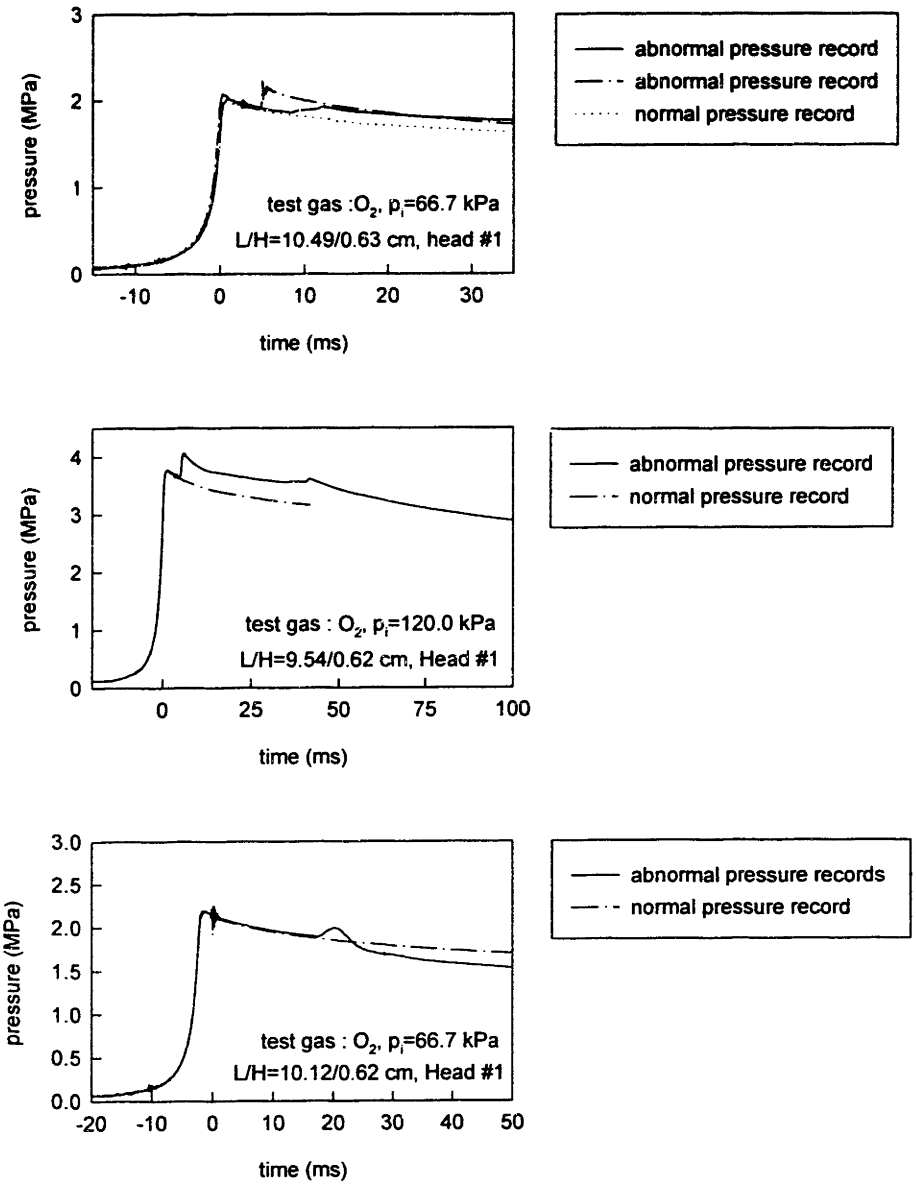

Figure A.2.2.2 Abnormal pressure records for oxygen runs. The oxygen dummy runs were used between hydrogen oxidation runs.

with abnormal pressure records, which clearly indicate that chemical reactions occur by unknown sources. The pressure records is characterized as : τ_d~5 to 20 ms, Δp~0.3 MPa and ΔT~30 K. In terms of ignition delay and pressure rise slope, they (possible ignition by oil vapor) differ from the previous case (possible ignition by alcoholic cleaner).

From the fact that those oxygen runs were performed between series of hydrogen oxidation runs and good repeatability has been attained without oxygen dummy runs in a case of piston head #6 (which was claimed to be able to minimize piston corner vortex and to achieve isothermal piston crevice volume as in Fig. 2.5.3 (f)), it can be drawn that the circumstances, in which oil layer (or vaporized hydraulic oil) can react at high temperature in abundant oxygen, is the only suspicious cause. The piston head #6 has the maximum surface to volume ratio compared to piston head #1 that has spacious piston crevice volume. Thus possible ignition of hydraulic oil vapor can be presumably minimized by the isothermal piston head, hence the repeatable measurements without abnormal autoignition were available.

APPENDIX 3. THERMODYNAMIC MODEL EQUATIONS

A.3.1. Derivation of thermodynamic model equations

Using thermodynamic model schematically shown in Fig. A.3.1.1, Model equations discussed in chapter 3 are derived as follows :

i) Core volume (where no temperature gradient is assumed to exist.)

Mass conservation :

$$dm_{\infty} = -d(m_{bl} + m_{cr}) \tag{3.3.1}$$

Volume conservation :

$$dV_{\infty} = dV - dV_{bl} \tag{3.3.2}$$

where the cylinder volume is

$$V = V_{\infty} + V_{bl}$$

Energy conservation :

$$dU_{\infty} = -pdV_{\infty} + h_{\infty}dm_{\infty} \tag{3.3.3}$$

where the internal energy for the core volume can be represented by :

$$dU_{\infty} = d(m_{\infty}u_{\infty}) \tag{3.3.4}$$

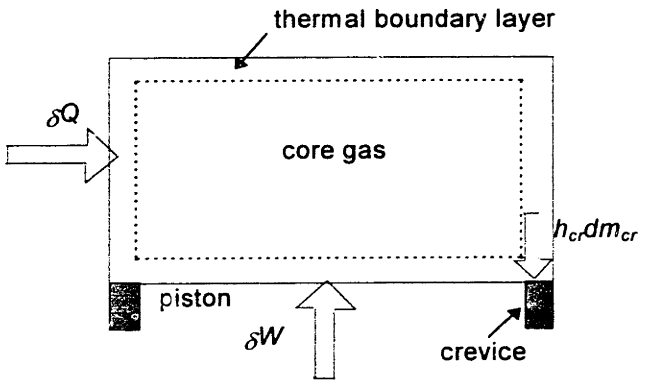

Figure A.3.1.1 Schematic diagram of thermodynamic. model.

and the specific internal energy can be calculated as

$$u_\infty = \sum_{i=1}^{K} h_i Y_i - \frac{p}{\rho_\infty} \tag{3.3.5}$$

where the specific enthalpy is calculated from

$$h_i = h_{f,i}^o + \int_{T_o}^{T_\infty} c_{p,i} dT \tag{3.3.6}$$

Species equation :

$$\frac{dY_i}{dt} = \frac{\dot{w}_i M_i}{\rho_\infty} \tag{3.3.7}$$

State equation :

$$p = \rho_\infty R_\infty T_\infty \tag{3.3.8}$$

ii) Boundary layer

Energy conservation :

$$dU_{bl} = \delta Q - p dV_{bl} - h_\infty dm_\infty - h_{cr} dm_{cr} \tag{3.3.9}$$

where conduction heat transfer through the cylinder wall is defined as (temperature gradient was discussed in Ch.3.)

$$\delta Q = -k_w A(y) \left.\frac{dT}{dy}\right|_{y=0} dt \tag{3.3.10}$$

Enthalpy associated with the mass going into/out of a piston crevice volume is defined as (energy-averaged temperature T'_{cr} can be calculated as in Ch.3.)

$$h_{cr} \equiv \begin{cases} c'_{p,cr} T'_{cr} & dm_{cr} > 0 \\ c_{p,cr} T_{cr} & dm_{cr} < 0 \end{cases} \tag{3.3.11}$$

and the mass can be calculated from

$$m_{cr} = \frac{p V_{cr}}{R_{cr} T_{cr}} \tag{3.3.12}$$

State equation :

$$p = \bar{\rho}_{bl} \bar{R}_{bl} \bar{T}_{bl} \tag{3.3.13}$$

where the mass average density is defined as

$$\bar{\rho}_{bl} = \frac{p}{\bar{R}_{bl} \bar{T}_{bl}} = \frac{1}{V_{bl}} \int_0^{\delta_t} \frac{pA(y)}{RT} dy \tag{3.3.14}$$

and the mass average temperature is defined as

$$\bar{T}_{bl} = \frac{V_{bl}}{\int_0^{\delta_t} \frac{A(y)}{T} dy} \tag{3.3.15}$$

From given t and V(t), dependent variables p, T_∞, δt and Y_i can be calculated by solving above equations simultaneously.

Finally Eqs.(3.3.1)-(3.3.15) were reduced to (3+K) equations to find (3+K) dependent variables :

(a) Mass conservation for the total volume including core, boundary layer and crevice volume.

(b) Energy conservation for the core volume.

(c) Species equations for the core volume.

(d) Energy conservation for the boundary layer.

Derivation for part (a) :

From Eq.(3.3.1)

$$d(\rho_\infty V_\infty) + d(\rho_{bl} V_{bl}) + d(\rho_{cr} V_{cr}) = 0 \tag{a-1}$$

$$V_\infty d\rho_\infty + V_{bl} d\rho_{bl} + V_{cr} d\rho_{cr} + \rho_\infty dV_\infty + \bar{\rho}_{bl} dV_{bl} + \rho_{cr} dV_{cr} = 0 \tag{a-2}$$

With Eq.(3.3.2) and divided by V and ρ_∞, Eq.(a-2) becomes

$$\frac{V_\infty}{V} \frac{d\rho_\infty}{\rho_\infty} + \frac{V_{bl}}{V} \frac{d\rho_{bl}}{\rho_\infty} + \frac{V_{cr}}{V} \frac{d\rho_{cr}}{\rho_\infty} + \left(\frac{\rho_{bl}}{\rho_\infty} - 1 \right) \frac{dV_{bl}}{V} + \frac{\rho_{cr}}{\rho_\infty} \frac{dV_{cr}}{V} = 0 \tag{a-3}$$

With the following relations that

$$\frac{1}{\rho_\infty}d\rho' = \frac{T_\infty}{T'}\frac{dp}{p} - \frac{T_\infty}{T'^2}dT' \tag{a-4}$$

Equation (a-3) becomes

$$\boxed{\left(\frac{V_\infty}{V} + \frac{V_{bl}}{V}\frac{T_\infty}{\bar{T}_{bl}} + \frac{T_\infty}{T_{cr}}\frac{V_{cr}}{V}\right)\frac{dp}{p} - \frac{V_\infty}{V}\frac{dT_\infty}{T_\infty} - \frac{V_{bl}}{V}\frac{T_\infty}{\bar{T}_{bl}}\frac{d\bar{T}_{bl}}{\bar{T}_{bl}} + \left(1 - \frac{T_\infty}{\bar{T}_{bl}}\right)\frac{dV_\infty}{V} + \frac{T_\infty}{T_{cr}}\frac{dV_{cr}}{V} = 0} \tag{a-5}$$

where $\bar{T}_{bl}$ was defined as in Eq.(3.3.15) and V_{cr} was discussed in section A1.2.

Derivation for part (b) :

From Eq. (3.3.3)-(3.3.4)

$$d(m_\infty u_\infty) = -pdV_\infty + h_\infty dm_\infty \tag{b-1}$$

With $d(pV) = pdV + Vdp$, Eq.(b-1) becomes

$$d(m_\infty u_\infty + pV_\infty) = V_\infty dp + h_\infty dm_\infty \tag{b-2}$$

From $h = u + pv$, Eq.(b-2) is reduced to

$$d(m_\infty h_\infty) = V_\infty dp + h_\infty dm_\infty \tag{b-3}$$

or

$$m_\infty dh_\infty + h_\infty dm_\infty = V_\infty dp + h_\infty dm_\infty \tag{b-4}$$

i.e.,
$$dh_\infty = \frac{V_\infty}{m_\infty}dp = \frac{dp}{\rho_\infty} \tag{b-5}$$

Using Eqs.(3.3.5)-(3.3.6), Eq.(b-5) can be represented as

$$\boxed{d\left[\left(\sum_{i=1}^{K} h_{f,i}^{o} + \int_{T^o}^{T_\infty} c_{p,i}dT\right)Y_i\right] = c_{p,\infty}dT_\infty + \sum_{i=1}^{K} h_i^o dY_i = \frac{dp}{\rho_\infty}} \tag{b-6}$$

Note that Eq.(b-6) can be reduced as follows in case that chemical reaction is not considered :

$$c_{p,\infty} dT_\infty = \frac{dp}{\rho_\infty} \tag{b-7}$$

or

$$\frac{dT_x}{T_x} = \frac{\gamma(T_x) - 1}{\gamma(T_x)} \frac{dp}{p} \tag{b-8}$$

which represents the isentropic relation between the core temperature and pressure when the chemical reaction is not involved.

Part (c) :

$$\frac{dY_i}{dt} = \frac{\dot{w}_i M_i}{\rho_\infty} \tag{3.3.7) (c-1}$$

Derivation for part (d) :

Following same procedures as in Eqs.(b-1)-(b-3), Eq.(3.3.9) becomes

$$d(m_{bl} h_{bl}) = \delta Q + V_{bl} dp - h_\infty dm_\infty - h_{cr} dm_{cr} \tag{d-1}$$

where

$$m_{bl} h_{bl} \equiv \int_0^{\delta_t} \rho c_p T A(y) dy$$

$$= \int_0^{\delta_t} \frac{\gamma}{\gamma - 1} pA(y) dy$$

$$= \left(\frac{\bar{\gamma}}{\bar{\gamma} - 1} \right)_{bl} pV_{bl} \tag{d-2}$$

Then Eq.(d-1) becomes

$$d(m_{bl} h_{bl}) = \left(\frac{\bar{\gamma}}{\bar{\gamma} - 1} \right)_{bl} (pdV_{bl} + V_{bl} dp)$$

$$= \delta Q + V_{bl} dp - h_\infty dm_\infty - h_{cr} dm_{cr} \tag{d-3}$$

Divided by pV, Eq.(d-3) becomes

$$\left(\frac{\bar{\gamma}}{\bar{\gamma}-1}\right)_{bl}\frac{dV_{bl}}{V}+\left(\frac{1}{\bar{\gamma}-1}\right)_{bl}\frac{V_{bl}}{V}\frac{dp}{p}=\frac{1}{pV}\delta Q-\frac{h_{\infty}dm_{\infty}}{pV}-\frac{h_{cr}dm_{cr}}{pV} \tag{d-4}$$

Using the following relations

$$\frac{1}{pV}dm'=\frac{1}{R'T'}\left(\frac{V'}{V}\frac{dp}{p}+\frac{d\bar{V}'}{V}-\frac{V'}{V}\frac{dT'}{T'}\right) \tag{d-5}$$

and $h_a \equiv c_p T_a$, Eq.(d-4) can be reduced to

$$\begin{aligned}&\left[\left(\frac{1}{\bar{\gamma}-1}\right)_{bl}\frac{V_{bl}}{V}+\left(\frac{\gamma}{\gamma-1}\right)_{\infty}\frac{V_{\infty}}{V}+\left(\frac{\gamma}{\gamma-1}\right)_{cr'}\frac{T'_{cr}}{T_{cr}}\frac{V_{cr}}{V}\right]\frac{dp}{p}+\left(\frac{\bar{\gamma}}{\bar{\gamma}-1}\right)_{bl}\frac{dV_{bl}}{V}+\\&\left(\frac{\gamma}{\gamma-1}\right)_{\infty}\frac{dV_{\infty}}{V}-\left(\frac{\gamma}{\gamma-1}\right)_{\infty}\frac{V_{\infty}}{V}\frac{dT_{\infty}}{T_{\infty}}+\left(\frac{\gamma}{\gamma-1}\right)_{cr'}\frac{T_{cr'}}{T_{cr}}\frac{dV_{cr}}{V}=-\frac{1}{pV}k_w A(y)\left.\frac{dT}{dy}\right|_{y=0}dt\end{aligned} \tag{d-6}$$

where properties T'_{cr} and $\gamma'_{cr'}$ are calculated at conditions denoted in Eq.(3.3.11).

A.3.2. Verification of assumptions for thermodynamic model

Based on the typically measured pressure and calculated temperature (non-reacting case by Eq.(2.2.1)) for hydrogen, oxygen and argon mixture, thermodynamic and transport properties of the mixture were calculated (using the code by Ely 1992) and shown in Fig.A.3.2.1. Verification of assumptions for the thermodynamic model are as follows :

(a) No chemical reaction takes place in the boundary layer :

Since the reaction rate varies approximately proportionally with the concentration of reactants and exponentially with temperature, the estimated ratio of reaction in the boundary layer to the core, the only place where the chemical reaction is assumed to occur, is approximately

$$\frac{\dot{\omega}_{bl}}{\dot{\omega}_{\infty}} \sim \frac{\rho_{bl}\exp(-E_a / RT_{bl})}{\rho_{\infty}\exp(-E_a / RT_{\infty})} \sim \frac{T_{\infty}\exp(-E_a / RT_{bl})}{T_{bl}\exp(-E_a / RT_{\infty})} \qquad \text{(A.3.2.1)}$$

The calculated ratio is shown in Fig.A.3.2.2 with typical conditions such as E_a=*70 kcal/mol*, T_{∞}=1000 K and T_i=300 K.

(b) Heat transfer is controlled by heat conduction from the core gases to the wall :

As shown in Fig. A.3.2.3, the conduction heat transfer is more significant than convection heat transfer at these flow conditions. Note that Reynolds number is much smaller than the critical value (~O(10^5)), for transition to turbulence (Convective transport towards the wall of course will still result from the density gradient through the boundary layer).

(c) Pressure is a function only of time :

The pressure throughout the cylinder is independent of the distance from the wall and a function only of time require that the transit time of a sound wave across the cylinder be small compared to the characteristic time for change in the pressure. Characteristic heating

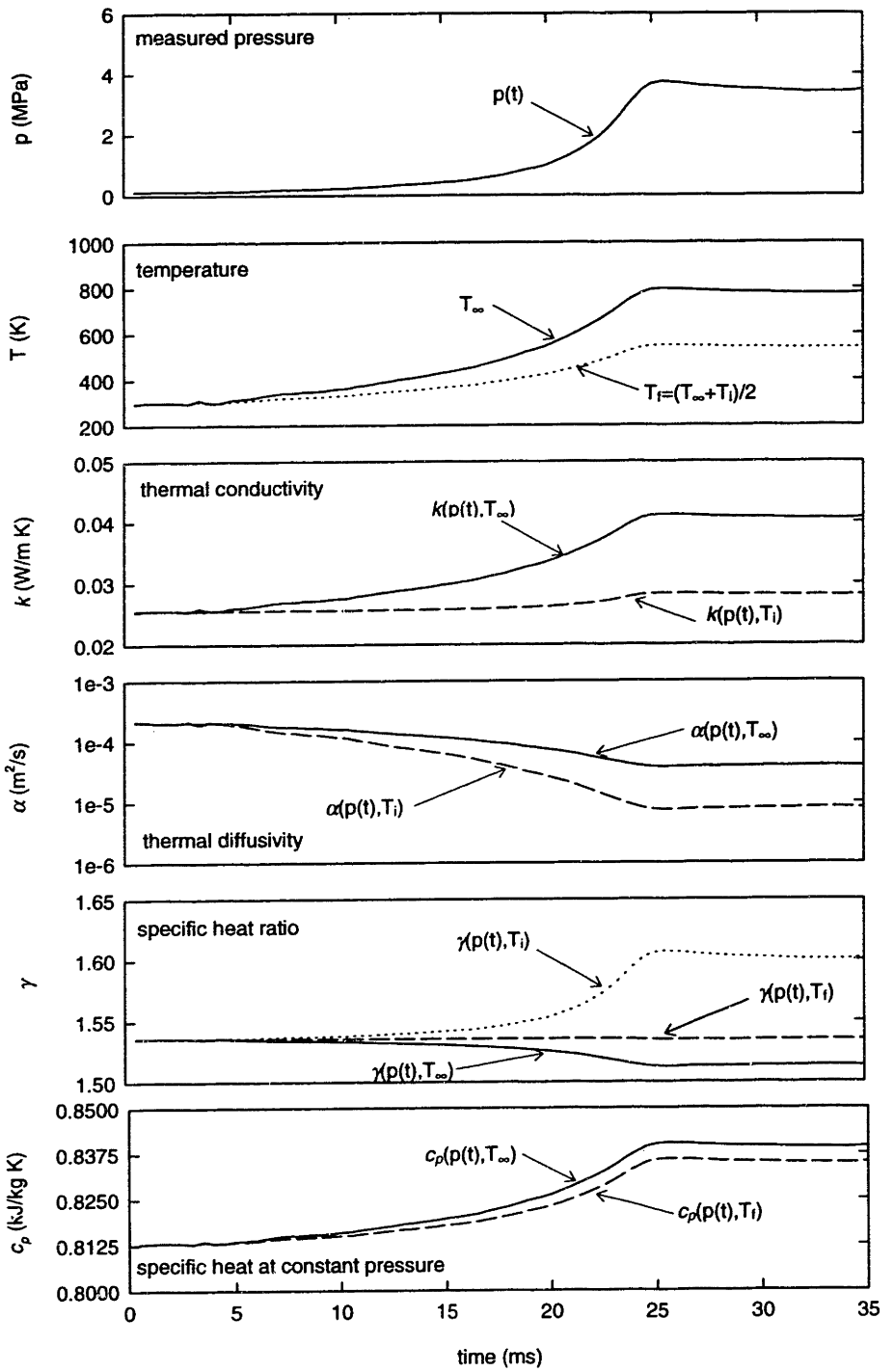

Figure A.3.2.1 Thermodynamic properties as functions of pressure and temperature. Measured pressure data is for $H_2/O_2/Ar=2/1/5$. $p_i=0.12$ MPa. $T_i=295$ K. L=7.446 cm and H=0.622 cm. Temperature was calculated under isentropic compression. Film temperature is defined as $T_f=(T_\infty+T_i)/2$.

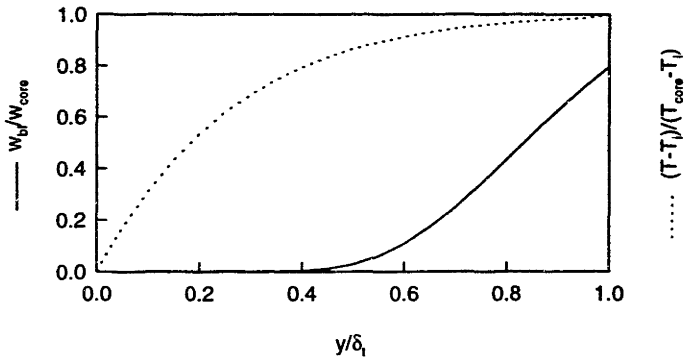

Figure A.3.2.2 Calculated the estimated ratio of chemical reaction in boundary layer to the core, where the chemical reaction is assumed to take place only. With E_a=*70 kcal/mol*, T_∞=1000 K and T_i=300 K.

rise time can be defined as the reciprocal of the logarithmic pressure rise rate at the end of the compression, and is given by the following relation (Park 1990) :

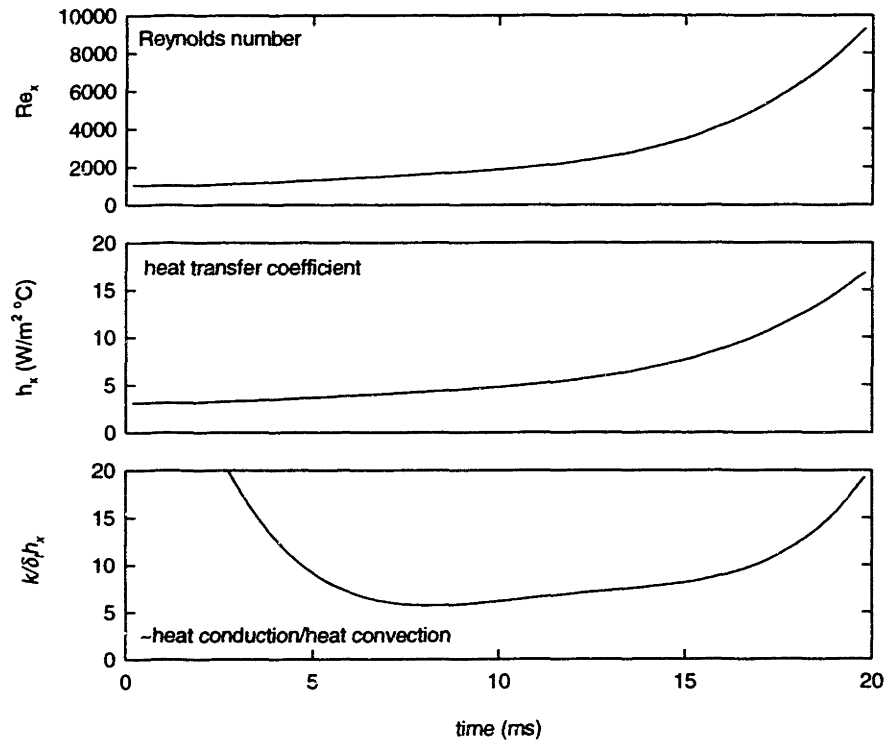

Figure A.3.2.3 Calculated Reynolds number, heat transfer coefficient and approximate ratio of heat conduction to heat convection. Pressure and temperature conditions are as same as in Fig. A.3.2.1. Film temperature was used to calculated corresponding thermodynamic properties.

time is

$$\frac{1}{\tau_{ch}} = \frac{d(\ln p)}{dt} = -\frac{\gamma}{V}\frac{dV}{dt} = \gamma\frac{U_p}{H}$$

i.e.,

$$\tau_{ch} = \frac{H}{\gamma U_p} \qquad \text{(A.3.2.2)}$$

Characteristic time for sound propagation (time for sound wave to cross the cylinder) can be defined as follows :

$$\tau_a = \frac{H}{a} = \frac{H}{\sqrt{\gamma RT}} \qquad \text{(A.3.2.3)}$$

Calculations from typical experimental conditions, τ_{ch}~O(1) ms and τ_a~O(10^{-3}) ms, show that the speed of sound is so fast that pressure variation throughout the cylinder can be neglected (except during the very fast pressure rise due to autoignition at the final induction period).

(g) Gas in the chamber obeys the ideal gas law : Compressibility factor is close to unity at these conditions (p=0.02~5 MPa, T=290~1200 K).

(h) Chamber walls remain at the initial temperature Ti :

Since heat is transferred mostly by conduction, the temperature rise at the wall can be calculated from heat transfer balance.

$q_{gas\ to\ wall} = q_{conducted\ into\ wall}$

$$\left(k\frac{\Delta T}{\delta}\right)_{wall} \sim \left(k\frac{\Delta T}{\delta}\right)_{gas} \qquad \text{(A.3.2.4)}$$

i.e.,

$$\frac{(\Delta T)_{wall}}{(\Delta T)_{gas}} \sim \frac{\left(\sqrt{k\rho c_p}\right)_{gas}}{\left(\sqrt{k\rho c_p}\right)_{wall}} \sim O(10^{-3})$$

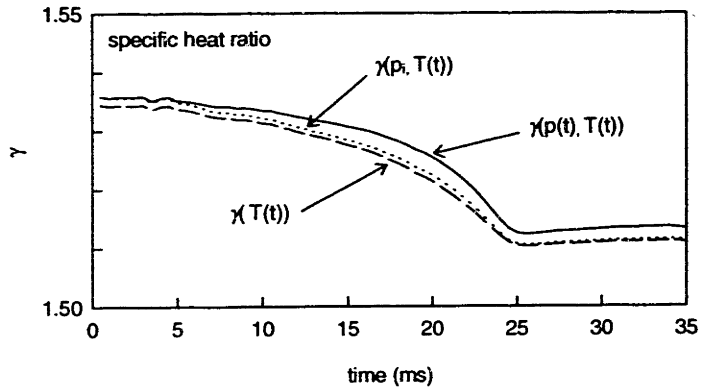

Figure A.3.2.4 Calculated specific heat ratio as function of pressure and temperature. p(t) and $T_\infty(t)$ are as same as in Fig. A.3.2.1.

Nikanjam & Greif (1978) measured the surface temperature of the wall in a rapid compression machine. During the compression, a thin platinum film resistance thermometer recorded the increase of about 3 K from the initial temperature.

(i) the ratio of specific heats (γ) is a function only of temperature : Refer to Fig. A.3.2.4.

(j) the gas constant R is uniform :

Composition of gas mixture is not significantly changed between each region. Thus,

$$R_\infty \approx R_{bl} \approx R_{cr} \approx \frac{R^o}{M} = \frac{R^o}{\sum_{i=1}^{K} Y_i M_i} \qquad \text{(A.3.2.5)}$$

A. 3.3 Derivation of compression time from measured data

For the model, compression time was assumed to be known as an input. Dynamic modeling of the RCM may determine the compression time from given geometry and operating conditions including an orifice angle of the speed control valve and its discharge coefficient as Park (1990) performed. For this study, however, compression time is derived from measured data. As shown in Fig.A.3.3.1, the correlation was made from measured data as a function of stroke (cm) and initial pressure (mmHg) as follows:

$$\tau_{cmp}(ms) = 0.11 \cdot \sqrt{p_i(mmHg)} \cdot L(cm) \qquad \text{(A.3.3.1)}$$

Note that measured compression time corresponds to $H_2/O_2/Ar$ mixtures in 2/1/5 ratio. All operating conditions were kept constant except stroke and initial pressure.

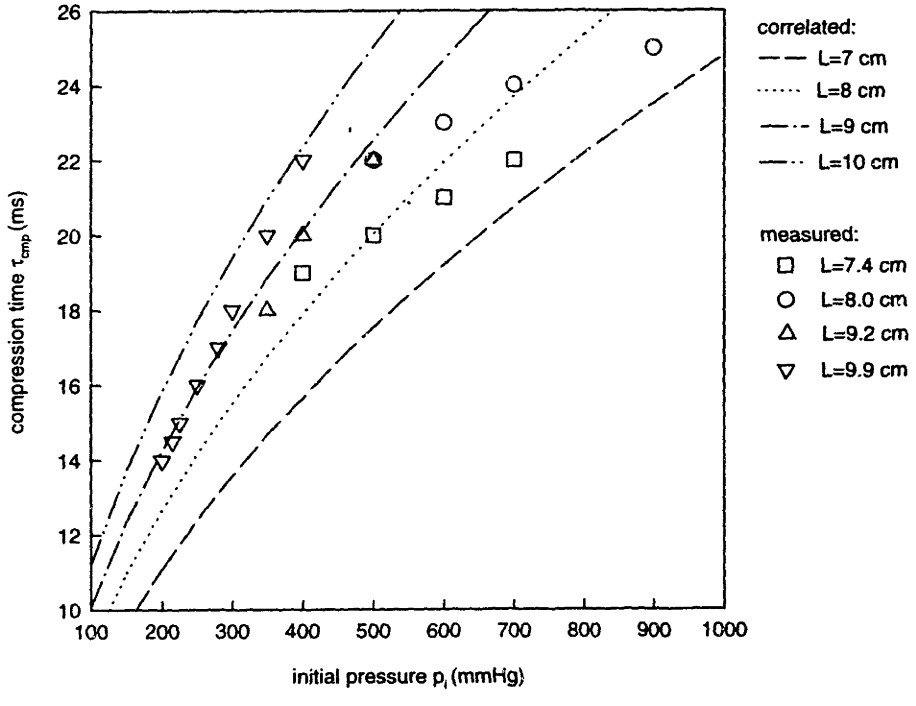

Figure A.3.3.1 Correlated compression time from measured data as a function of stroke and initial pressure in cm and mmHg respectively.

A.4.1 Thermodynamic properties and reaction rate data

Table A.4.1 Polynomial coefficients to calculate Thermodynamic properties (Kee 1987).

```
THERMO
  300.000  1000.000  5000.000
AR                120186AR 1                G 0300.00  5000.00  1000.00                1
 0.02500000E+02 0.00000000E+00 0.00000000E+00 0.00000000E+00 0.00000000E+00 2
-0.07453750E+04 0.04366000E+02 0.02500000E+02 0.00000000E+00 0.00000000E+00 3
 0.00000000E+00 0.00000000E+00-0.07453750E+04 0.04366000E+02                4
N2                KEE87N  2               G 0300.00  5000.00  1000.00                1
 0.02926640E+02 0.14879768E-02-0.05684760E-05 0.10097038E-09-0.06753351E-13 2
-0.09227977E+04 0.05980528E+02 0.03298677E+02 0.14082404E-02-0.03963222E-04 3
 0.05641515E-07-0.02444854E-10-0.10208999E+04 0.03950372E+02                4
H2O               KEE87H  2O  1           G 0300.00  5000.00  1000.00                1
 0.02672145E+02 0.03056293E-01-0.08730260E-05 0.12009964E-09-0.06391618E-13 2
-0.02989921E+06 0.06862817E+02 0.03386842E+02 0.03474982E-01-0.06354696E-04 3
 0.06968581E-07-0.02506588E-10-0.03020811E+06 0.02590232E+02                4
HO2               KEE87H  1O  2           G 0300.00  5000.00  1000.00                1
 4.07219124E+00 2.13129632E-03-5.30814532E-07 6.11226902E-11-2.84116471E-15 2
-1.57972702E+02 3.47602940E+00 2.97996306E+00 4.99669695E-03-3.79099697E-06 3
 2.35419240E-09-8.08902424E-13 1.76227387E+02 9.22272396E+00                4
H2O2              KEE87H  2O  2           G 0300.00  5000.00  1000.00                1
 0.04573167E+02 0.04336136E-01-0.14746888E-05 0.02348903E-08-0.14316536E-13 2
-0.01800696E+06 0.05011369E+01 0.03388753E+02 0.06569226E-01-0.14850125E-06 3
-0.04625805E-07 0.02471514E-10-0.01766314E+06 0.06785363E+02                4
H                 KEE87H  1           G 0300.00  5000.00  1000.00                1
 0.02500000E+02 0.00000000E+00 0.00000000E+00 0.00000000E+00 0.00000000E+00 2
 0.02547162E+06-0.04601176E+01 0.02500000E+02 0.00000000E+00 0.00000000E+00 3
 0.00000000E+00 0.00000000E+00 0.02547162E+06-0.04601176E+01                4
H2                KEE87H  2           G 0300.00  5000.00  1000.00                1
 0.02991423E+02 0.07000644E-02-0.05633828E-06-0.09231578E-10 0.15827519E-14 2
-0.08350340E+04-0.13551101E+01 0.03298124E+02 0.08249441E-02-0.08143015E-05 3
-0.09475434E-09 0.04134872E-11-0.10125209E+04-0.03294094E+02                4
O                 KEE87O  1           G 0300.00  5000.00  1000.00                1
 0.02542059E+02-0.02755061E-03-0.03102803E-07 0.04551067E-10-0.04368051E-14 2
 0.02923080E+06 0.04920308E+02 0.02946428E+02-0.16381665E-02 0.02421031E-04 3
-0.16028431E-08 0.03890696E-11 0.02914764E+06 0.02963995E+02                4
O2                KEE87O  2           G 0300.00  5000.00  1000.00                1
 0.03697578E+02 0.06135197E-02-0.12588420E-06 0.01775281E-09-0.11364354E-14 2
-0.12339301E+04 0.03189165E+02 0.03212936E+02 0.11274864E-02-0.05756150E-05 3
 0.13138773E-08-0.08768554E-11-0.10052490E+04 0.06034737E+02                4
OH                KEE87O  1H  1          G 0300.00  5000.00  1000.00                1
 0.02882730E+02 0.10139743E-02-0.02276877E-05 0.02174683E-09-0.05126305E-14 2
 0.03886888E+05 0.05595712E+02 0.03637266E+02 0.01850910E-02-0.16761646E-05 3
 0.02387202E-07-0.08431442E-11 0.03606781E+05 0.13588605E+01                4
END
```

where coefficients for HO_2 were compared with Sum *et al.* (1987)

```
HO2               BOZELLH  1O  2       G 0300.00  2000.00                1
 0.31903283E+01 0.37656915E-02-0.11613037E-05-0.15938400E-09 0.11601701E-12 2
 0.65320746E+03 0.82943891E+01 0.31903283E+01 0.37656915E-02-0.11613037E-05 3
-0.15938400E-09 0.11601701E-12 0.65320746E+03 0.82943891E+01                4
```

Table A.4.2 Reaction rate data for CHEMKIN driver by Kim *et al.* (1994).

```
! kim et al. (1994)
ELEMENTS
H O N AR
END
SPECIES
H2O   H2    O2    HO2   H2O2 OH   H    O AR N2
END
REACTIONS
H+O2=O+OH                       1.91E14         0.0             16440
O+H2=H+OH                       5.13E04         2.67            6290
OH+H2=H+H2O                     2.14E08         1.51            3430
O+H2O=OH+OH                     2.95E06         2.02            13400
H2+M=H+H+M                      4.571E19        -1.4            104380
    H2O/12/ H2/2.5/ O2/1/ HO2/1/ H2O2/1/ OH/1/ H/1/ O/1/ AR/0/
H2+AR=H+H+AR                    5.89E18         -1.1            104380
O+O+M=O2+M                      6.17E15         -.5             0
   H2O/12/ H2/2.5/ O2/1/ HO2/1/ H2O2/1/ OH/1/ H/1/ O/1/  AR/0/
O+O+AR=O2+AR                    1.91E13         0.0             -1790
O+H+M=OH+M                      4.68E18         -1.0            0
   H2O/12/ H2/2.5/ O2/1/ HO2/1/ H2O2/1/ OH/1/ H/1/ O/1/  AR/0.75/
H+OH+M=H2O+M                    2.24E22         -2.0            0
   H2O/12/ H2/2.5/ O2/1/ HO2/1/ H2O2/1/ OH/1/ H/1/ O/1/  AR/0/
H+OH+AR=H2O+AR                  8.32E21         -2.0            0
H+O2(+M)=HO2(+M)                4.47E13         0.0             0
   H2O/12/ H2/2.5/ O2/1/ HO2/1/ H2O2/1/ OH/1/ H/1/ O/1/  AR/0/
   LOW / 6.17E19  -1.42   0 /
H+O2(+AR)=HO2(+AR)              4.47E13         0.0             0
  LOW /1.51E15    0.0    -1000/
HO2+H=H2+O2                     6.61E13         0.0             2130
HO2+H=OH+OH                     1.70E14         0.0             870
HO2+O=OH+O2                     1.74E13         0.0             -400
HO2+OH=H2O+O2                   1.91E16         -1.0            0
HO2+HO2=H2O2+O2                 4.17E14         0.0             11980
  DUP
HO2+HO2=H2O2+O2                 1.29E11         0.0             -1629
  DUP
H2O2(+M)=OH+OH(+M)              2.95E14         0.0             48400
   H2O/12/ H2/2.5/ O2/1/ HO2/1/ H2O2/1/ OH/1/ H/1/ O/1/ AR/0/
   LOW /1.20E17    0.0       45500/
H2O2(+AR)=OH+OH(+AR)            2.95E14         0.0             48400
   LOW /1.91E16    0.0       43000/
H2O2+H=H2O+OH                   1.0E13          0.0             3590
H2O2+H=H2+HO2                   4.79E13         0.0             7950
H2O2+O=OH+HO2                   9.55E06         2.0             3970
H2O2+OH=H2O+HO2                 1.0E12          0.0             0
  DUP
H2O2+OH=H2O+HO2                 5.8E14          0.0             9560
  DUP
```

Table A.4.3 Reaction rate data for CHEMKIN driver by Marinov *et al.* (1995).

```
! Marivov et al. (1995)
ELEMENTS
H O N AR
END
SPECIES
H2O   H2    O2    HO2   H2O2 OH   H    O  AR N2
END
REACTIONS
O+OH=O2+H                   2.02E14         -.4             0
OH+H2=H+H2O                 2.14E08         1.52            3449
OH+OH=O+H2O                 3.57E04         2.40            -2112
O+H2=H+OH                   5.06E04         2.67            6290
H+H+M=H2+M                  1.E18           -1.0            0
  H2O/0/ H2/0/ O2/1/ HO2/1/ H2O2/1/ OH/1/ H/1/ O/1/ AR/1/
H+H+H2=H2+H2                9.27E16         -.6             0
H+H+H2O=H2+H2O              6.E19           -1.25           0
O+O+M=O2+M                  1.89E13         0               -1788
  H2O/12/ H2/2.5/ O2/1/ HO2/1/ H2O2/1/ OH/1/ H/1/ O/1/  AR/1/
O+H+M=OH+M                  4.71E18         -1.0            0
  H2O/12/ H2/2.5/ O2/1/ HO2/1/ H2O2/1/ OH/1/ H/1/ O/1/  AR/1/
H+OH+M=H2O+M                2.21E22         -1.25           0
  H2O/12/ H2/2.5/ O2/1/ HO2/1/ H2O2/1/ OH/1/ H/1/ O/1/  AR/1/
H+O2(+M)=HO2(+M)            4.517E13        0               0
  H2O/0/ H2/0/ O2/1/ HO2/1/ H2O2/1/ OH/1/ H/1/ O/1/  AR/1/
  LOW  /1.05E19  -1.257  0/
H+O2(+H2)=HO2(+H2)          4.517E13        0               0
  LOW  /1.52E19  -1.133  0/
H+O2(+N2)=HO2(+N2)          4.517E13        0               0
  LOW  /2.031E20  -1.590  0/
H+O2(+H2O)=HO2(+H2O)        4.517E13        0               0
  LOW  /2.1E23  -2.437  0/
HO2+H=H2+O2                 8.45E11         0.65            1241
HO2+H=OH+OH                 1.50E14         0               1000
HO2+H=O+H2O                 3.01E13         0               1721
HO2+O=OH+O2                 3.25E13         0               0
HO2+OH=H2O+O2               2.89E13         0               -497
HO2+HO2=H2O2+O2             4.20E14         0               11980
  DUP
HO2+HO2=H2O2+O2             1.30E11         0               -1629
  DUP
OH+OH(+M)=H2O2(+M)          1.24E14         -0.37           0
  H2O/12/ H2/2.5/ O2/1/ HO2/1/ H2O2/1/ OH/1/ H/1/ O/1/ AR/1/
  LOW /3.041E30  -4.63  2049/
  TROE /0.47  100 2000 1E15/
H2O2+H=H2O+OH               3.07E13         0               4217
H2O2+H=H2+HO2               1.98E6          2.0             2435
H2O2+O=OH+HO2               9.55E06         2.0             3970
H2O2+OH=H2O+HO2             2.4E0           4.042           -2162
```

A.4.2. Structure of programs

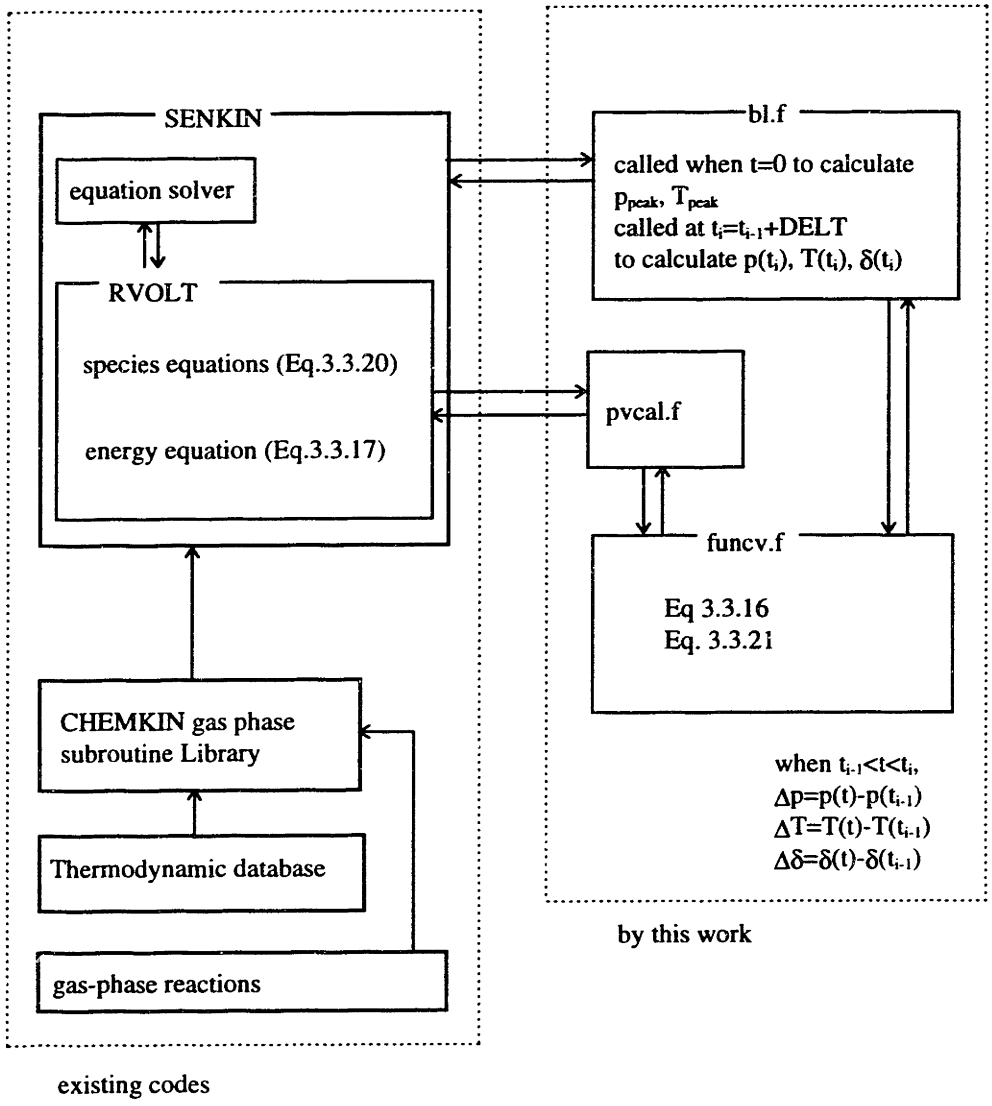

Figure 4.2.1 Structure of programs to calculate pressure history for autoignition in the rapid compression machine.

A.4.3. List of programs

```
c   List of variables
c
c   indx_bl  :index in bl2.f, =1 for 1st run, =2 for 2nd run
c   CH       :clearance height in cm
c   CH2      :half of clearance height in cm
c   H        :temporal variable for Lagrange interpolation
c   KK       :temporal variable for Lagrange interpolation
c   NDIM     :variable dimension for Lagrange interpolation
c   NORDER:number of order for Lagrange interpolation
c   NTABLE  :dimesion size for Lagrange interpolation =NDIM
c   PI       :=3.141592
c   PINP     :initial pressure for Lagrange interpolation
c   PPISEN   :isen. press. for Lagrange interpolation, (mmHg)
c   RES1-12 :common statement
c   T        :temporal variable for Lagrange interpolation
c   TIM      :time from the main, =0 when SENKIN routine starts.
c   TMP      :temperature for Lanrange interpolation
c   TT       :temporal variable
c   VZERO    :core volume calculated in pvcal.f
c   YAR      :mole fraction for argon
c   YM       :mole fraction for fuel
c   YN2      :mole fraction for nitrogen
c   YO2      :mole fraction for oxygen
c   ac_fct   :factor to form acceleration slope of verlocity profile
c   accel    :acceleration for piston velocity
c   acro     :normalized area of acrv
c   acrv     :area of isentropic crevice volume(cm**2) read from RCMPRMT
c   alph     :thermal diffusivity
c   aov      :normalized area/volume
c   blt      :boundary layer thickness (cm)
c   bore     :bore of a cylinder (cm) read from RCMPRMT file
c   broydn   :system of equation solver
c   btime    :time recorded when bl2.f is called, btime(ndt)=TIM
c   ch2      :=clht/2, temporary variable
c   clht     :clearance height (cm) read from RCMPRMT
c   d_guess  :guess of thermal boundary layer thickness
c   dc_fct   :factor to form deceleration slope of verlocity profile
c   decel1   :factor to form deceleration slope of verlocity profile
c   decel2   :factor to form deceleration slope of verlocity profile
c   delt     :thermal boundary layer thickness
c   delt_ht  :temporary b.l. thickness calculated in PVCAL.F
c   delta    :norm. var. for boundary layer thickness
c   deltao   :previous delta
c   dpdt     :time derivative of pressure
c   dqdt     :heat transfer rate
c   dt       :incremental time variable
c   dt0      :incremental time, =tc(sec)/ndt1
c   dt_ht    :incremental time to calculate heat transfer
c   dtim     :incremental time, dtim(ndt)
c   dvov     :dV/V
c   dx       :=x-xold
c   fvec(1)  :Eq.3.3.16
c   fvec(2)  :Eq.3.3.21
c   gambl    :specific heat ratio for boundary layer
c   gambl1   :1/(gambl-1)
c   gambl2   :gambl/(gambl-1)
c   gamc     :specific heat ratio for core gas
c   gamc2    :gamc/(gamc-1)
c   gamcr    :specific heat ratio for gas entering into crevice
c   gamcr2   :gamcr/(gamcr-1)
c   gamm     :FUNCTION calculating specific heat ratio
c   gamma    :temporary variable
c   gamwall  :specific heat ratio at wall temperature
c   i        :index for the loop in BL2.F
c   indx_bl  :index for BL2.F initial loop
c   indx_pv  :index for PVCAL.F initial loop
c   Irout    :output file index for 'rout'
c   n_accel  :#(w.r.t ndt) of loop for acceleration during compression
c   n_decel  :#(w.r.t ndt) of loop for decceleration during compression
c   n_indx   :index (funcv.f & bl.f) =0(compression), =2(after comp)
c   n_value  :index for BROYDN, # of index variable. (=2)
c   ndt      :loop index for dt, ndt1 for compression
c   ndt1     :(=500), read from RCMPRMT
c   ndt2     :=ndt1+4
c   ndt3     :=ndt1+10 or 11
c   ondt     :=ndt1
c   p_guess  :pressure guess in FUNCV.F
c   pconv    :pressure conversion factor from mmHg to dyne/cm**2
c   pini     :initial pressure in mmHg
c   pinp     :=pp(ndt)*pini (mmHg)
c   pp       :normalized pressure, pp(10000)
c   ppisen   :isentropic pressure for Lagrange interpolation
c   ppm      :pressure (MPa) at time=time
c   press    :pressure
c   pressi   :=pp(ndt)*pini (mmHg)/760*.101325, pressure in MPa
c   pressi_ht :pressure at time=TIM
c   rcmprmt  :common statement for parameters of RCM
c   rad      :bore/2
c   rado     :bore/2/strk
c   s        :temporary variable to calculate stroke x
```

```
c   strk       :stroke (cm) read from RCMPRMT
c   strkx      :=x*strk (cm), stroke at time t
c   t_guess    :temperature guess
c   t_oring    :time constant in calculating o-ring crevice volume(Eq.A.1.1.3)
c   taccel     :acceleration time
c   teat_cal   :FUNCTION calculating T'=(cp*V)cv/(cp*V/T)cv
c   tc         :compression time in sec
c   tcmp       :compression time (msec) read from /rcmprmt/ or Eq.A.3.3.1
c   tcore      :core temperature
c   tcore_ht   :core temperature at time=TIM
c   tcorr      :corrected time for time zero shifted at stpst pt.
c   tdecel     :decceleration time
c   temp       :core temperature at each time, temp(10000)
c   temp_bl    :FUNCTION calculating boundary layer temperature
c   temp_core  :temporary variable
c   tempp      :temporary variable for core temperature at time t
c   tgrad      :temperature gradient at wall
c   time       :in sec, calculated in BL2.F. =0 when piston starts
c   time_ht    :=TIM, time saved(PVCAL.F) to calculate dq/dt in FUNCV.F
c   timec      :time when compression is done
c   tini       :initial temperature read from RCMPRMT file
c   tmp        :temperature for Lagrange interpolation, tmp(4000)
c   tncore     :temporary variable in FUNCTION TEMP_BL
c   tsft       :shifted time due to time zero at the steepest pt. (RCMPRMT)
c   tx1        :coefficient for normalized temperature, power=0
c   tx2        :coefficient for normalized temperature, power=1
c   tx3        :coefficient for normalized temperature, power=2
c   tx4        :coefficient for normalized temperature, power=3
c   tx5        :coefficient for normalized temperature, power=4
c   tx6        :coefficient for normalized temperature, power=5
c   v_oring    :volume of o-ring crevice =1.369 cm**3
c   v1_fct     :factor to shape velocity profile
c   value(1)   :input variable to BROYDN for pressure
c   value(2)   :input variable to BROYDN for b.l. thickness
c   vcore      :volume of core gas
c   vcr_isn    :isentropic crevice volume in cm**3
c   vcr_isno   :normalized vcr_isn w.r.t initial volume
c   vcr_iso    :isothermal crevice volume in cm**3
c   vcr_isoo   :normalized vcr_iso w.r.t initial volume
c   vcrv       :crevice volume/cylinder volume
c   vcrvv      :=vcr_isoo/(x+vcr_isno), used in FUNCV.F
c   velo1      :velocity profile during compression
c   velo2      :velocity profile during compression
c   voli       :initial volume
c   x          :normalized stoke x=x(t)
c   xcho       :normalized clearance height
c   xi         :=strk/clht
c   xold       :previous x


      SUBROUTINE RVOLT (TIME, Z, ZP, DELTA, IRES, RPAR, IPAR)
ccccccccccccccccccccccccccccccccccccccccccccccccccccccccccccccccccccccc
c
c     modified energy equation to include pressure drop due to
c     heat transfer in a Rapid Compression Machine
c
ccccccccccccccccccccccccccccccccccccccccccccccccccccccccccccccccccccccc
C
C*****double precision
      IMPLICIT DOUBLE PRECISION (A-H, O-Z), INTEGER (I-N)
C*****END double precision
C*****single precision
C     IMPLICIT REAL (A-H, O-Z), INTEGER (I-N)
C*****END single precision
C
      DIMENSION Z(*), ZP(*), DELTA(*), RPAR(*), IPAR(*)
C
      EXTERNAL VOLT
      external pvcal
C
      COMMON /RES1/ P
      COMMON /RES2/ TOTMAS
      common /tempo1/ rhocore
C
C  Residual of differential equations for case where volume is
C  a user-specified function of time.
C
C  Variables:
C    Z(1)  = temperature (Kelvin)
C    Z(K+1) = species mass fractions
C    P     = pressure (dyne/cm2)
C    RHO   = density (gm/cm3)
C    TOTMAS = mass (gm) - constant for closed system
C    TIME  = time (sec)
C
C  User supplys a subroutine for the volume:
C    SUBROUTINE VOLT (TIME, VOL, DVDT)
C    VOL   = volume of system
C    DVDT  = time derivative of system volume
C    VOLSP = specific volume
```

```
C   VDOT   = time derivative of specific volume
C  Note: Consistent units for volume are (cm3), but the volume can
C       be considered to be normalized and therefore unitless.
C       The problem is solved using intensive variables, so the
C       solution is independent of extensive variables such as
C       the volume and total mass.  Subroutine VOLT is called at
C       time zero and a total mass is computed, but the solution
C       only depends on the density, so the total mass and total
C       volume are not important.
C
      KK    = IPAR(1)
      IPRCK  = IPAR(2)
      IPRA   = IPAR(3)
      IPRB   = IPAR(4)
      IPRE   = IPAR(5)
      IPWT   = IPAR(6)
      IPWDOT = IPAR(7)
      IPU    = IPAR(8)
      IPICK  = IPAR(9)
      LOUT   = IPAR(10)
      II     = IPAR(11)
C
C       MODIFY CHEMKIN WORK ARRAY FOR PRE-EXPONENTIAL
C
      CALL CKA (II, RPAR(IPRCK), RPAR(IPRA))
C
C       GET VOLUME AS FCN OF TIME
C
      tcore=Z(1)

      call pvcal (TIME, tcore, P, dpdt, VOL)
      call ckrhoy(P,tcore,Z(2),IPAR(IPICK),RPAR(IPRCK),rhocore)
      volsp=1./rhocore
      IF (VOLSP .EQ. 0.0) THEN
        WRITE (LOUT, '(/1X,A)') 'Stop, zero volume in RVOLT.'
        STOP
      ENDIF
      RHO = 1./ VOLSP

C
C       CALL CHEMKIN SUBROUTINES
C
      call ckcpbs (Z(1), Z(2), IPAR(IPICK), RPAR(IPRCK), CPB)
      CALL CKWYR  (RHO, Z(1), Z(2), IPAR(IPICK), RPAR(IPRCK),
     1            RPAR(IPWDOT))
      CALL CKUMS  (Z(1), IPAR(IPICK), RPAR(IPRCK), RPAR(IPU))
C
C       ENERGY EQUATION (Eq.3.3.17)
C
      SUM = 0.
      DO 100 K = 1, KK
        K1 = K-1
        SUM = SUM + RPAR(IPU+K1) * RPAR(IPWDOT+K1) * RPAR(IPWT+K1)
100   CONTINUE

      DELTA(1) = ZP(1) + (- dpdt + SUM) /CPB *VOLSP
C
C       SPECIES EQUATIONS (Eq.3.3.20)
C
      DO 200 K = 1, KK
        K1 = K-1
        DELTA(K+1) = ZP(K+1) - RPAR(IPWDOT+K1) *RPAR(IPWT+K1) *VOLSP
200   CONTINUE
C
      RETURN
      END


      SUBROUTINE bl2(lrout, TIM)
ccccccccccccccccccccccccccccccccccccccccccccccccccccccccccccccc
c
c     calculating 1. peak pressure and peak core temperature
c     2. after compression process, pressure p(i) and
c     thermal boundary layer thickess blt(i)
c
ccccccccccccccccccccccccccccccccccccccccccccccccccccccccccccccc
      implicit double precision (a-h, o-z), integer (i-n)

      dimension pp(10000),blt(10000),btime(10000)
      dimension tmp(4000),ppisen(4000),temp(10000)
      dimension value(2),ymol(10)

      common /res5/ pp,btime
      common /res6/ ndt, blt
      common /res7/ pconv, temp,tcore_pk,press_pk
      common /res8/ i, dt0, xo, aov, n_indx, deltao
      common /res9/ dvov, ax0, popo, vcrvv
      common /res12/ xtim, yblt, ypres, ytemp
      common /rcmprmt/ tcmp,vcrv,rad,clht,strk,pmax,pini,tini,
     *           errp,ndt1,tsft,acrv,strkx
```

```
      common /intf/ tmp, ppisen
      common /vtim/ tcore_ht, time_ht, factc
      COMMON /MOLE_FRACTION/YM,YO2,YN2,YAR !mole fractions
      common /seninp/ ymol
      common /funcv1/ vcr3,vcr3old,tblold,d_old,tavgbl,teat
      common /funcv2/ strko, vol,tcold,tcore
      common /bl21/ v_oring, t_oring
      common /tempo1/ rhocore
      data ntable /4000/
      data norder /2/
      data n_value /2/

      parameter (PI=3.141592)
      ytotal=ymol(2)+ymol(3)+ymol(10)+ymol(9)
      ym=ymol(2)/ytotal  ! in onder appearing at mech (reaction rate file)
      yo2=ymol(3)/ytotal
      yn2=ymol(10)/ytotal
      yar=ymol(9)/ytotal

      indx_bl = indx_bl + 1
c
c     compresssion process & initializing
c
      IF (indx_bl.eq.1) THEN

c
c       compression time from Eq.A.3.3.1
c
        tcmp=0.112D0*sqrt(pini)*strk
        cpp=cp(tini)
        gam1=gamma(tini)
        palpha=1.*pini/760.*.101325
        alphai=alpha(palpha,tini)
c
c     assign variables for Lagrange interpolation
c
        H=(2000.-tini)/4000.
        DO KK=1,4000
            T=tini+H*FLOAT(KK-1)
            GA=gamma(T)
            TMP(KK)=GA/(GA-1.)/T
        ENDDO
        NDIM=4000
        CALL QSF(H,TMP,PPISEN,NDIM)
        DO KK=1,4000
            PPISEN(KK)=EXP(PPISEN(KK))*pini
        ENDDO
c
c       TEMPERATURE ASSIGNMENT
c
        H=(2000.-tini)/4000.
        DO KK=1,4000
            TMP(KK)=tini+H*FLOAT(KK-1)
        ENDDO

        pconv=1.01325E6*(pini/760.)
        t_core=tini
        v_oring=1.369
        t_oring=15.

        vcr1=0.
        vcr2=vcrv
        tc=tcmp/1000.
        tsft=tsft/1000.
        dt0=tc/float(ndt1)

        rado=rad/strk
        vcr1o=vcr1/(PI*(rad**2)*strk)
        vcr2o=vcr2/(PI*(rad**2)*strk)
        acro=acrv/(PI*(rad**2))
        xcho=(strk+clht)/strk

        pp(1) = 1.0
        time = 0.
        blt(1)=0.
        deltao=1.D-3
        tblold=tini
        d_old=0.
        strko=strk+clht
        vcr3=0.
        vcr3old=0.
        tcold=tini
c
c       for velocity profile during compression process
c
        ac_fct=0.1
        dc_fct=0.1
        v1_fct=0.8
        xold=xcho-1./float(ndt1)
        taccel=tc*ac_fct
```

```
      tdecel=tc*dc_fct
      n_accel=int(taccel/dt0)
      taccel=float(n_accel)*dt0
      n_decel=int(tdecel/dt0)
      tdecel=float(n_decel)*dt0
      v1_fct=(2.-ac_fct-dc_fct)/2.
      velo1=strk/tc/v1_fct
      velo2=strk/tc*(2.*v1_fct-1.+dc_fct)/(1.-ac_fct)/v1_fct
      accel=velo1/taccel
      decel1=(velo1-velo2)/(tc-taccel-tdecel)
      decel2=velo2/tdecel
c
c     compression process (n_indx=0)
c
      n_indx=0
      do i = 2, ndt1
c
c     calculate normalized stoke x with acceleration and decceleration
c
          time = dt0*float(i)
          if (i.le.n_accel) then
              s=accel*time**2/2.
              x=1.- s/strk + clht/strk
              s1=s
          else if ((i.lt.(ndt1-n_decel)).and.(i.gt.n_accel)) then
              s=s1+velo1*(time-taccel)
              s=s-.5D0*decel1*(time-taccel)**2
              x=1.-s/strk+clht/strk
              s2 = s
          else if (i.ge.(ndt1-n_decel)) then
              s=s2+velo2*(time-tc+tdecel)
              s=s-decel2*(time-tc+tdecel)**2/2.
              x=1.-s/strk+clht/strk
          endif
          dx=x-xold
          strkx=x*strk
          xold=x
          aov=(2.+2.*x/rado)/(x+vcr1o)
          dvov=dx/(x+vcr1o)
          vcrvv=vcr2o/(x+vcr1o)
          vol=pi*rad**2*strkx
          value(1)=pp(i-1)*1.05
          value(2)=deltao*1.01
          n_value=2
c
c     calculate boundary layer thickness and pressure
c     from the mass conservation using relations in funcv.f routine
c     BROYDN : system of nonlinear equation solver
c
              call broydn(value, n_value, check)
              pp(i)=value(1)
              delta=value(2)
              deltao=delta
              blt(i)=delta*strk
              pinp=pp(i)*pini
              call lagint1(ppisen,tmp,ntable,norder,pinp,tt)
              tempp=tt
              tblold=tavgbl
              d_old=delta*strk
              strko=strkx
              tcold=tempp
              tcorr=time-tc+tsft
              ppm=pp(i)*pconv/1.D7          ! in MPa
              write(lrout,1000)  tcorr, ppm, tempp, blt(i)
1000          format (1p,4E13.3)
          end do
          timec=time
          tcore_pk=tempp
          press_pk=ppm
          tcold=tempp
          n_indx=2
      ELSE
c
c     after the compression (n_indx=2)
c
          xi=clht/strk
          aov=(2.+2.*xi/rado)/(xi+vcr1o)
          vcrvv=vcr2o/(xi+vcr1o)
          strkx=clht
          n_indx=2
          ttim=TIM*1000.
c
c         calculating o-ring crevice volume (Eq.A.1.1.3)
c
          vcr3=v_oring*(1.-exp(-ttim**0.6/t_oring))

          time_ht=TIM
          value(1)=pp(ndt-1)*0.98
          value(2)=deltao*1.01
c
```

```
c    calculate boundary layer thickness and pressure
c    from the mass conservation using relations in fconv.f routine
c    BROYDN : system of nonlinear equation solver
c
       call broydn(value, n_value, check)
       pp(ndt)=value(1)
       delta=value(2)
       deltao=delta
       tblold=tavgbl
       d_old=delta*strk
       strko=strkx
       vcr3old=vcr3
       tcold=tcore
c
c    physical dimension of thermal boundary layer thickness in cm
c
       blt(ndt)=delta*strk
        ch2=clht/2.
       if (blt(ndt).ge.ch2) then
c           pause 'blt larger than CH/2'
           STOP
       endif
       btime(ndt)=TIM
       tcorr=timec-tc+TIM+tsft
       ppm=pp(ndt)*pconv/1.E7      ! in MPa
       tempp=tcore_ht
       write(lrout,1100)  tcorr, ppm, tempp, blt(ndt)
1100     format (1p,4E13.3)

     ENDIF

     RETURN
     end

     subroutine funcv(n,x,fvec)
ccccccccccccccccccccccccccccccccccccccccccccccccccccccccccccccccccccccc
c
c    subroutine to calculate pressure and thermal boundary layer
c    thickness
c    input : n, x(1) for pressure, x(2) for b.l. thickness
c    output : fvec(1) from Eq.3.3.16, fvec(2) from Eq.3.3.21
c
ccccccccccccccccccccccccccccccccccccccccccccccccccccccccccccccccccccccc
     implicit real*8 (a-h, o-z), integer (i-n)
     DIMENSION TMP(4000),PPISEN(4000),fvec(2),x(2)
     dimension temp(10000)

     common /res5/ p(10000),btime(10000)
     common /res6/ ndt,blt(10000)
     common /res7/ pconv, temp,tcore_pk,press_pk
     common /res8/ i, dt0, xo, aov, n_indx, deltao
     common /rcmprmt/ tcmp,vcr2,rad,ch,stroke,pmax,pini,tempi,
    *          errp,ndt1,tsft,acrv,strkx
     common /intf/ tmp, ppisen
     common /vtim/ tcore_ht, time_ht, factc
     common /funcv1/ vcr3,vcr3old,tblold,d_old,tavgbl,teat
     common /funcv2/ strko,vol,tcold,tcore
     parameter (PI=3.141592D0)

     DATA NTABLE/4000/
     DATA NORDER/2/  !use 2nd order Lagrange polynomial
c
c    n_indx=0 : during compression process, w/o reaction
c    n_indx=2 : after compression process, w/ reaction
c
     IF (n_indx.eq.0) THEN
        pinp=x(1)*pini
        CALL LAGINT1(PPISEN,TMP,NTABLE,NORDER,PINP,TT)
        tcore=TT
        dtqht=dt0
        dpovp=(x(1)-p(i-1))/x(1)
     ELSE IF (n_indx.eq.2) THEN
        tcore=tcore_ht
        dtqht=time_ht-btime(ndt-1)
        factc=(x(1)-p(ndt-1))/dtqht
        dpovp=(x(1)-p(ndt-1))/x(1)
     ENDIF

     dtcovtc=1.-tcold/tcore
     p_guess=x(1)*pconv/1.D7              ! in MPa
     delta=x(2)
     d_guess=x(2)*stroke
     gamc=gamma(tcore)
     gamc2=gamc/(gamc-1.)
     gamwall=gamma(tempi)
     tavgbl=tavg_bl(tcore,d_guess)
     gambl=gamma(tavgbl)
     gambl2=gambl/(gambl-1.)
     gambl1=1./(gambl-1.)
c
```

```
c    x(1)*pressi is cancelled out with terms for fact2
c    rkwall=x(1)*pressi/tempi*gam_wall/(gam_wall-1.)*alpha_wall
c
     rkwall=1./tempi*gamwall/(gamwall-1.)*alpha(p_guess, tempi)

     if (n_indx.eq.0) then
c
c    teat = energy-averaged temperature for mass going into
c          isothermal crevice
c
        teat=teat_cal(tcore,d_guess)
             teatovtcr=teat/tempi
     else
        teat=tempi
        teatovtcr=-1.
     endif
     gamcr=gamma(teat)
     gamcr2=gamcr/(gamcr-1.)
     vol=PI*rad**2*strkx
     vblovv=vbl(d_guess,strkx)/vol

     tcovtbl=tcore/tavgbl
     vcrovv=(vcr2+vcr3)/vol

     tcovtcr=tcore/tempi
     dtblovtbl=(tavgbl-tblold)/tavgbl

     dvblovv=(vbl(d_guess,strkx)-vbl(d_old,strko))/vol
     vcovv=vcore(d_guess,strkx)/vol
     dvcovv=(vcore(d_guess,strkx)-vcore(d_old,strko))/vol
     if (n_indx.eq.0) then
        dvcrovv=0.
     else
        dvcrovv=(vcr3-vcr3old)/vol
     endif
c
c    fvec(1) from Eq.(3.3.16)
c
     term11=vcovv+vblovv*tcovtbl
     term11=term11+tcovtcr*vcrovv
     term11=term11*dpovp
     term12=-vcovv*dtcovtc
     term13=vblovv*tcovtbl*dtblovtbl
     term14=tcovtbl*dvblovv+dvcovv
     term15=tcovtcr*dvcrovv

     fvec(1)=term11+term12-term13+term14+term15
c
c    fvec(2) from Eq.(3.3.21)
c
     dqht=-aov/stroke*rkwall*dtqht*tgrad(tcore,d_guess)

     term21=gambl1*vblovv
     term21=term21+gamc2*vcovv
     term21=term21+gamcr2*teatovtcr*vcrovv
     term21=term21*dpovp
     term22=gambl2*dvblovv
     term23=gamc2*dvcovv
     term24=gamc2*vcovv*dtcovtc
     term25=dqht
     term26=gamcr2*dvcrovv

     fvec(2)=term21+term22+term23-term24-term25+term26

     return
     END


     function vcore(delt,strk)
c
c    calculating volume of core
c
     implicit double precision (a-h, o-z), integer (i-n)
     common /rcmprmt/ tcmp,vcr2,rad,ch,stroke,pmax,pini,tempi,
    *          errp,ndt1,tsft,acrv,strkx
     parameter (pi=3.141592)

     ch2=ch/2.D0
     if ((delt.gt.0).and.(delt.lt.ch2)) then
        vcore=pi*(rad-delt)**2*(strk-2.*delt)
     else
        vcore=pi*rad**2*strk
     endif

     return
     END


     function func_aot(x,tcore,delt)
c
```

```
c    fuction defining integral of 1/temperature over volume
c    of thermal boundary layer
c
     implicit double precision (a-h, o-z), integer (i-n)
     common /rcmprmt/ tcmp,vcr2,rad,ch,stroke,pmax,pini,tempi,
    *           errp,ndt1,tsft,acrv,strkx

     parameter (PI=3.141592)

     area=2.*pi*(rad-x)**2+2.*pi*(rad-x)*(strkx-2.*x)
     if (delt.gt.0) then
        xodelt=x/delt
        temp=temp_bl(xodelt,tcore,tempi)
     else
        temp=tempi
     endif

     aot=area/temp
     func_aot=aot

     return
     end


     function tgrad(tcore,delt)
c
c    calculating temperature gradient at the wall
c    dt/dy|y=0 = (tcore-tini)/delt*tx2
c
     implicit double precision (a-h, o-z), integer (i-n)
     common /rcmprmt/ tcmp,vcr2,rad,ch,stroke,pmax,pini,tempi,
    *           errp,ndt1,tsft,acrv,strkx

     parameter (PI=3.141592)
     data tx2 / 3.61502 /

     tgrad=(tcore-tempi)/delt*tx2

     return
     end

     function teat_cal(tcore,delt)
c
c    function defining teat: energy-averaged temperature
c    for mass going into isothermal crevice
c
     implicit double precision (a-h, o-z), integer (i-n)
     common /rcmprmt/ tcmp,vcr2,rad,ch,stroke,pmax,pini,tempi,
    *           errp,ndt1,tsft,acrv,strkx

c    gap between wall and piston in cm
     data gap /.046D0/

     sum1=0.
     sum2=0.
     gap_step=gap/20.D0
     ch2=ch/2.
     if ((delt.gt.0).and.(delt.lt.ch2)) then
        do x=0,gap,gap_step
           xodelt=x/delt
           if (xodelt.lt.1) then
              temp=temp_bl(xodelt,tcore,tempi)
           else
              temp=tcore
           endif
           sum1=sum1+cp(temp)*gap_step
           sum2=sum2+cp(temp)*gap_step/temp
        enddo
        cpd=sum1
        cpdot=sum2
        teat_cal=cpd/cpdot
     else
        teat_cal=tcore
     endif

     return
     end

     function vbl(delt,strk)
c
c    function defining volume of thermal boundary layer
c
     implicit double precision (a-h, o-z), integer (i-n)
     common /rcmprmt/ tcmp,vcr2,rad,ch,stroke,pmax,pini,tempi,
    *           errp,ndt1,tsft,acrv,strkx

     parameter (PI=3.141592)

     vol=pi*rad**2*strk
     vbl=vol-vcore(delt,strk)
```

```
      return
      end


      function tavg_bl(tcore,delt)
c
c     calculating defining average temperature of thermal boundary layer
c
      implicit double precision (a-h, o-z), integer (i-n)
      common /rcmprmt/ tcmp,vcr2,rad,ch,stroke,pmax,pini,tempi,
     *           errp,ndt1,tsft,acrv,strkx

      external func_aot
      parameter (PI=3.141592)

      x1=0.
      x2=delt
      ch2=ch/2.D0
      if ((delt.gt.0).and.(delt.lt.ch2)) then
         call qromb (func_aot,x1,x2,vot,tcore,delt)
         tavg_bl=vbl(delt,strkx)/vot
      else
         tavg_bl=tempi
      endif

      return
      end

      function alpha(pres, temp)
c
c     calculate alpha(thermal diffusivity) with H2/O2/Ar=2/1/5 ratio
c     input press in MPa(=10**6N/m**2)
c     output alpha in cm**2/sec
c
      implicit real*8 (a-h, o-z), integer(i-n)
      COMMON /MOLE_FRACTION/YM,YO2,YN2,YAR !mole fractions

      data wm_h2, wm_o2, wm_ar, wm_n2
     *     /2.02D0, 32, 39.948D0, 28.013D0/  !g/mol or kg/kmol
      data UR /8.31434D0/                    !J/mol or kJ/kmol

      press=pres*1.D6
      rho_h2=press/temp/(UR/wm_h2*1000.)
      rho_o2=press/temp/(UR/wm_o2*1000.)
      rho_ar=press/temp/(UR/wm_ar*1000.)
      rho_n2=press/temp/(UR/wm_n2*1000.)
      rho=rho_h2*YM+rho_o2*YO2+rho_ar*YAR+rho_n2*YN2
      alph=rkovcp(temp)/rho
      alpha=alph*1.D4                    ! in cm^2/sec

      return
      end

      function rkovcp(T)
c
c     function defining thermal conductivity over heat capacity cp
c     k/Cp (W/m K / J/kg) for H2/O2/Ar=2/1/5 ratio
c
      implicit real*8 (a-h, o-z), integer (i-n)

      data c1,c2,c3,c4
     *           /3.67792D-3,1.09245D-4,-6.23007D-8,2.19844D-11/

      rkovcp=c1+c2*T+c3*T*T+c4*T*T*T
      rkovcp=rkovcp/1000.

      return
      end

      function temp_bl(x,tcore,tempi)
c
c     calculating temperature of thermal boundary layer
c     from thickness x and core temperature
c
      implicit real*8 (a-h, o-z), integer (i-n)
c
c     coefficients for normalized temperture profile
c
      data tx1, tx2, tx3, tx4, tx5, tx6
     *     / 3.67241e-3, 3.61502, -5.73534, 4.88238,
     *      -2.16448, 3.89161e-1 /

      xodelt=x
      tncore=tx1+tx2*xodelt+tx3*xodelt**2
      tncore=tncore+tx4*xodelt**3+tx5*xodelt**4
      tncore=tncore+tx6*xodelt**5

      temp_bl=(tcore-tempi)*tncore+tempi
```

```
      return
      end


      SUBROUTINE pvcal(TIM,tcore,press, dpdt, VZERO)
ccccccccccccccccccccccccccccccccccccccccccccccccccccccccccccccccccccccccccc
c
c     subroutine to calculate pressure, dpdt and core volume
c     input : TIM, tcore
c     output : press, dpdt, VZERO
c
ccccccccccccccccccccccccccccccccccccccccccccccccccccccccccccccccccccccccccc
      implicit double precision (a-h,o-z), integer (i-n)

      dimension pp(10000), dtim(10000), blt(10000)
      dimension temp(10000),value(2), btime(10000)
      parameter (pi=3.141592654)

      common /RES1/ P
      common /RES3/ T
      common /res5/ pp, dtim,btime
      common /res6/ ndt, blt
      common /res7/ pconv, temp,tcore_pk,press_pk
      common /res8/ i, dt0, xo, aov, n_indx, deltao
      common /res12/ xtim, yblt, ypres, ytemp
      common /rcmprmt/ tcmp,vcrv,rad,clht,strk,pmax,pini,tini,
     *          errp,ndt1,tsft,acrv,strkx
      common /res13/ pmaxo2
      common /vtim/ tcore_ht, time_ht, factc
      common /funcv1/ vcr3,vcr3old,tblold,d_old,tavgbl,teat
      common /bl21/ v_oring, t_oring

      time_ht=TIM
      tcore_ht=tcore
c
c     n_indx=0: during compression process
c     n_indx=1: after compression, but not BL2.F called yet, which means
c           pressure is not calculated(converged) yet.
c     n_indx=2: after compression, when BL2.F called
c
      n_indx=2
      indx_pv=indx_pv+1
c
c     initializing
c
      if (indx_pv.eq.1) then
          temp(ndt1)=T
          temp(ndt1+1)=T
          ondt=ndt1
          blt(ndt1-1)=blt(ndt1)
          tempo=tini
      endif
c
c     for attenuation of initial searching, which is for 3*DELT period
c
      ndt3=ndt1+1

      if (ndt.ge.ndt3) then
          ttim=TIM*1000.
          vcr3=v_oring*(1.-exp(-ttim**0.6/t_oring))  !Eq.A.1.1.3
          value(1)=pp(ndt-1)*.99D0                  !guess of pressure
          value(2)=deltao*1.01D0                    !guess of b.l.t.
          n_value=2
          call broydn(value,n_value,check)
          pp(ndt)=value(1)
          p_guess=value(1)
          delt_ht=value(2)*strk
      else
          p_guess=pp(ndt1)
      endif

      press=p_guess*pconv
      ndt2=ndt1+2
c
c     factc from FUNCV.F
c     VZERO=density at the peak/density of core at time t
c         =(ppeak/Tpeak)*(Tcore/pcore)
c     in RVOLT of rcmsk2.f
c     VOLSP=VZERO/TOTMAS, which is a reciprocal of density
c     TOTMAS=RHO*ZERO
c     where VZERO=1 as initial condition and RHO=density(Tpeak,ppeak)
c
      dpdt=factc*pconv
      VZERO=pp(ndt1) /tcore_pk *tcore/p_guess

      return
      end
```

A.4.4. List of measured data for hydrogen autoignition

Table A.4.4 List of measured data for hydrogen autoignition.

no.	p_i(mmHg)	T_i(K)	p_{peak} (MPa)	T_{peak} (K)	L (cm)	H (cm)	τ_d (ms)
1	900.4	299.5	3.731	971.2	7.45	0.62	11.5
2	700.2	299.5	2.953	976.9	7.45	0.62	17.3
3	600.2	299.5	2.497	972.5	7.45	0.62	39.2
4	700	293.5	3.038	967.3	7.8	0.62	25.5
5	700	293.5	3.057	969.3	7.8	0.62	21.2
6	600.2	293.5	2.619	969.1	7.8	0.62	45
7	600.2	293.5	2.621	969.2	7.8	0.62	44.4
8	900.1	294	3.871	966	7.8	0.62	14
9	899.9	294	3.844	963.8	7.8	0.62	14.6
10	700.2	294	3.165	982.3	8	0.62	10.6
11	600	294	2.723	983.4	8	0.62	12.8
12	500.2	294	2.239	978.9	8	0.62	23.1
13	500.3	293.5	2.316	988.5	8.28	0.62	13.1
14	400.2	293.5	1.803	979.4	8.28	0.62	33.5
15	400	293.5	1.938	1003.6	8.70	0.62	8.3
16	350	293.5	1.667	998	8.70	0.62	12.1
17	300.4	293.5	1.398	990.3	8.70	0.62	26.5
18	290.2	293.5	1.361	992.7	8.70	0.62	28.3
19	300.4	293.5	1.485	1010.2	9.13	0.62	6.8
20	250.7	293.5	1.233	1008.6	9.13	0.62	10.3
21	225.1	294	1.091	1005.6	9.13	0.62	16.7
22	300.2	294	1.499	1015.4	9.13	0.62	5.8
23	215	294	1.039	1004.3	9.13	0.62	24.2
24	200.7	293.5	0.999	1012.7	9.55	0.62	13.6
25	175.5	293.5	0.868	1010.9	9.55	0.62	11.1
26	200.1	295	1.011	1022.9	9.55	0.62	5.7
27	200.1	295.3	0.985	1014.8	9.55	0.62	6
28	174.8	295.3	0.874	1020.1	9.55	0.62	5.6
29	174.9	295.3	0.88	1022.2	9.55	0.62	6
30	160.1	295.3	0.799	1019.6	9.55	0.62	7
31	160	295.2	0.791	1016.3	9.55	0.62	13.3
32	155.1	295.3	0.767	1016.5	9.55	0.62	16.7
33	155.1	295.3	0.75	1008.9	9.55	0.62	10.1
34	150.2	295.5	0.732	1012.2	9.55	0.62	21.2
35	210.1	295.5	1.105	1038.3	9.55	0.62	3.9
36	200.1	295.5	1.007	1023.2	9.55	0.62	5.1
37	199.9	295.3	1.042	1034.2	9.76	0.62	3.5
38	180	295.3	0.904	1022	9.76	0.62	4.6
39	160	295.3	0.803	1021.6	9.76	0.62	6.9
40	200.1	293.8	1.045	1030.3	9.76	0.62	5.7
41	200.2	294.1	1.046	1031.2	9.76	0.62	6
42	180.1	294.5	0.931	1028.9	9.76	0.62	9
43	180.1	294.7	0.936	1031.6	9.76	0.62	7.5
44	180.1	294.9	0.937	1032.4	9.76	0.62	7.8

(continued)

Table 4.4.1 *(continued).*

no.	p_i(mmHg)	T_i(K)	p_{peak} (MPa)	T_{peak} (K)	L (cm)	H (cm)	τ_d (ms)
45	160.5	296.5	0.824	1033.3	9.76	0.62	8.1
46	160	296.6	0.803	1025.9	9.76	0.62	7.8
47	155.2	297	0.803	1037.3	9.76	0.62	7.2
48	150.2	297	0.797	1046.3	9.9	0.62	4.4
49	130	296.6	0.678	1039	9.9	0.62	6.9
50	130.1	297	0.677	1039.8	9.9	0.62	6.4
51	120.1	297	0.615	1034.5	9.9	0.62	9
52	120.1	297.2	0.618	1036.6	9.9	0.62	6.4
53	109.9	296.9	0.569	1037.4	9.9	0.62	2.7
54	120.1	297	0.614	1033.4	9.9	0.62	7.2

$H_2/O_2/Ar$=2/1/5. Piston head #6 was used.

APPENDIX 5. ADDITIONAL SUGGESTION OF REACTION RATE CONSTANT K_{17}

The reaction rate constant for k_{17} has been suggested in section 5.5 based on the Arrhenius form, $k=A \exp(-E_a/RT)$. However, there seems to be the possibility that the rate constant k_{17} may be strongly dependent on temperature, as are rate constants k_{18} and k_{19} (see in Fig.5.5.7) because of their analogies to H atom abstraction reaction. Marinov *et al.* (1995) suggested the rate constant in a modified Arrhenius form, *i.e.*, $k_{17}=1.98E6\ T^2 \exp(-2435/RT)$, which was fitted from previous measurements to match their results (Fig. A.5.1.1). Accurate evaluation of this reaction rate constant is desirable for further study of high pressure hydrogen oxidation, which will consist of a sub-oxidation mechanism for more complex fuels. Particularly its rate at high temperature range (>1000 K) needs to be investigated thoroughly.

First, additional suggestion of the reaction rate is shown in Fig.A.5.1.1 and Eq.A.5.1.1, which is in a modified Arrhenius form. A correlation was performed with the reaction rate,

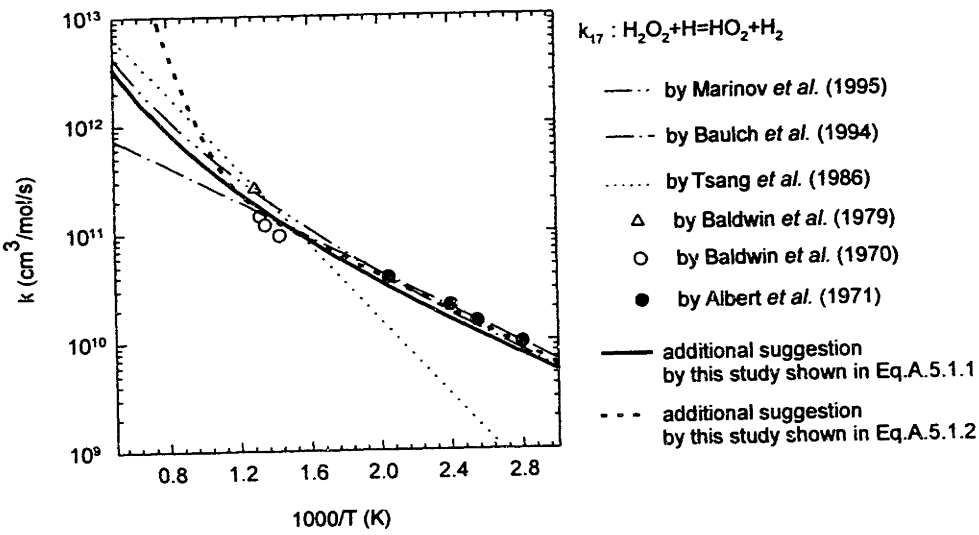

Figure A. 5.1.1 Comparison between reaction rate constants for k_{17}.

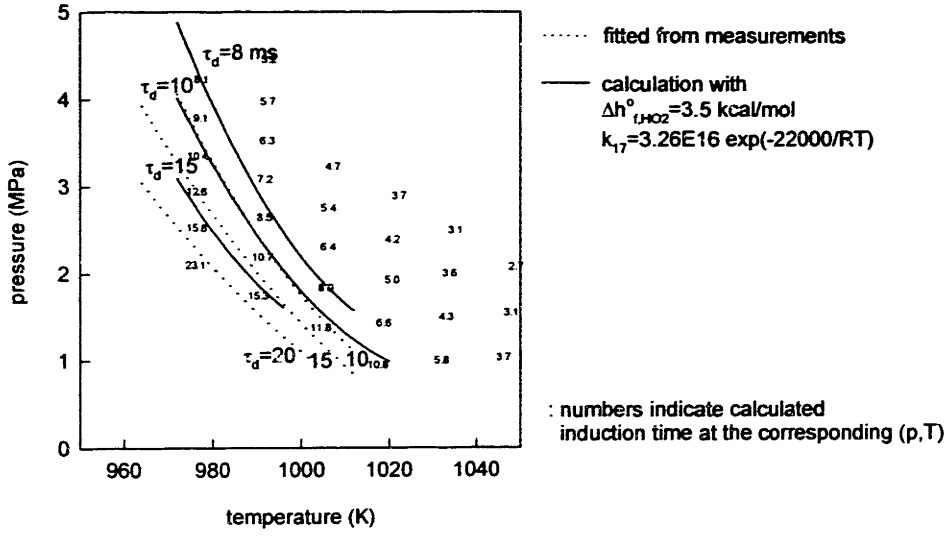

Figure A.5.1.2 Comparison between measured and calculated induction time contour. k_{17}=3.26E16 exp(-22000/RT) is used for calculation. Induction time contour was fitted from measured/calculated induction times at pressure and temperature space.

2.3E13 exp(-7950/RT), suggested in section 5.5 and the previous measured reaction rates at low temperatures shown in Fig.A.5.1.1. The result in a modified Arrhenius form is as follows:

$$k_{17}=3E5\ T^{2.2}\ \exp(-2000/RT) \qquad (A.5.1.1)$$

Second, additional suggestion is also made for k_{17}. Within the temperature ranges covered by the measurements, the best fit of k_{17} leads to k_{17}=3.26E16 exp(-22000/RT) as shown in Fig. A.5.1.2. Although this rate constant seems to show unrealistic rate constant in terms of a pre-exponential factor and an activation energy, the correlation between this rate constant and measured reaction rates can result in a rate constant as follows:

$$k_{17}=3E16\ \exp(-22000/RT) + 1.8E12\ \exp(-3750/RT) \qquad (A.5.1.2)$$

Comparison is shown in Fig. A.5.1.1. Further study to evaluate this rate constant is apparently necessary.

THESIS PROCESSING SLIP

FIXED FIELD: ill. _____ name _____

index _____ biblio _____

▶ COPIES: (Archives) Aero Dewey (Eng) Hum

Lindgren Music Rotch Science

TITLE VARIES: ▶☐ _____

NAME VARIES: ▶☐ _____

IMPRINT: (COPYRIGHT) _____

▶ COLLATION: 168 l.

▶ ADD. DEGREE: _____ ▶ DEPT.: _____

SUPERVISORS: _____

NOTES:

cat'r: date:

page: F.52

▶ DEPT: M. E.

▶ YEAR: 1997 ▶ DEGREE: Ph. D

▶ NAME: LEE, Daeyup